NUMERICAL SIMULATION OF THE ONE METER DROP TEST ON A BAR FOR THE CASTOR CASK

Advanced and final analyses

Nikola Jakšić, Karl-Fredrik Nilsson

DG JRC

Institute for Energy

2007

EUROPEAN COMMISSION
DIRECTORATE-GENERAL
Joint Research Centre

EUR 22470 EN / 2

Institute for Energy

Mission of the Institute for Energy
The Institute for Energy provides scientific and technical support for the conception, development, implementation and monitoring of community policies related to energy. Special emphasis is given to the security of energy supply and to sustainable and safe energy production.

European Commission
Directorate-General Joint Research Centre (DG JRC)
http://www.jrc.ec.europa.eu/

Institute for Energy, Petten (the Netherlands)
http://ie.jrc.ec.europa.eu/

Contact details:
Nikola Jakšić
+31 (0)224 565498
nikola.jaksic@jrc.nl

Karl-Fredrik Nilsson
+31 (0)224 565420
karl-fredrik.nilsson@jrc.nl

Legal Notice

Neither the European Commission nor any person acting on behalf of the Commission is responsible for the use which might be made of this publication.

The use of trademarks in this publication does not constitute an endorsement by the European Commission.

The views expressed in this publication are the sole responsibility of the author(s) and do not necessarily reflect the views of the European Commission.

A great deal of additional information on the European Union is available on the Internet. It can be accessed through the Europa server http://europa.eu/

EUR 22470 EN / 2
ISSN 1018-5593
Luxembourg: Office for Official Publications of the European Communities

© European Communities, 2007
Reproduction is authorised provided the source is acknowledged.
Printed in the Netherlands

Contents

Abstract

The report presents the numerical analysis of two one meter drop tests of a single ductile cast iron cask on a steel bar. This analysis is a follow-up to the analysis [1]. The cask comes from the CASTOR family with machined cooling fins in a region where impact occurs. In the first test, the impact is on the cask's cooling fins whereas in the second test the impact is in an area where the fins have been locally machined away. The numerical analysis is based on an explicit dynamic analysis using the commercial finite element code ABAQUS extended with Python scripts to allow a parametric description of the problem. The report describes two sets of analyses. First a comparison to the model used in [1] was carried out together with advanced parameter variation simulations (advanced sensitivity analyses) and then the responses of the basic model are compared with the experimental results provided by GNS. The overall behavior of the model is qualitatively very similar to what was observed during the experiments. The quantitative differences between experimental and numerical responses are generally within 10% and up to 20% with some exceptions. A longer impact duration, (between 3 ms to 5 ms) when the cask is dropped on the fins in comparison to the flat target, is observed in both the analysis and the test. The advanced sensitivity analysis was performed to study the influence of parameters either identified in [1] as influential or not yet tested there. Based on results the final set of parameters values are given and the final analysis is carried out. The overall behavior of the model is qualitatively very similar to what was observed during the experiments.

Chapter 1

Introduction

1.1 Scope

The integrity of waste packages is crucial for the safe disposal, storage and transport of spent nuclear fuel and radioactive waste. To certify waste packages the manufactures are required to demonstrate that the waste packages can withstand loads that could occur under operation and accident conditions. These tests are defined by IAEA [2] and used for transport regulations. The manufacturer needs to prove the integrity by full-scale testing or simulation. Simulations will never completely replace full-scale tests, but the trend is to do as much as possible by numerical analysis. Simulation has of course the advantage that the cost for a "numerical test" is significantly lower than for an actual drop test, but the numerical simulation gives also a better understanding of the underlying physics and allows the user to check the influence of specific parameters. The analysis of a drop test is a highly nonlinear and dynamic event and it is difficult to prove the accuracy and completeness of the results. Systematic assessment of the influence of the model parameters were studied in [1].

This report is result of the cooperation between JRC-IE (Joint Research Center - Institute for Energy) and GNS (Gesellschaft für Nuklear-Service mbH) and presents the modelling of the 1m drop test on a steel bar of a Castor AVR cask for the nuclear waste transport and storage.

This particular test was proposed by GNS to evaluate different modelling aspects. The problem has a direct practical implication since the effect of the cask's cooling fins on the impact behaviour is not completely understood. The finite element analysis is based on the explicit version of the commercial finite element code ABAQUS which has been extended with our own routines. The report describes two sets of analyses. First a comparison to a model used in [1] was carried out together with advanced parameter variation simulations (advanced sensitivity analyses) and then the responses of the basic model are compared to the experimental results provided by GNS. The recommendations are given for optimizing the final analysis with respect to accuracy as well as computational efficiency.

1.2 Introduction

CASTOR (**CA**sk for **S**torage and **T**ransport **O**f **R**adioactive material) and CONSTOR are casks for transport and storage of spent fuel and radioactive waste. The casks are used in the EU, Russia and the USA. The CASTOR is the family of the transport and storage cask for spent fuel and radioactive waste. Around 900 casks of the CASTOR family have been produced by GNS since 1979.

The IAEA drop test system is made up of a series of well defined structural and destructive dynamic tests [2]. It includes a 9 meter drop test on an unyielding surface as well as a 1 meter drop test on a bar. The tests are designed to simulate worst case scenarios during the cask transportation and handling. The manufacturer of casks need to verify that the casks' integrity and functioning are maintained after drop tests. This can either be done by experimental drop tests or by computer simulations which are difficult to perform. The drop tests are extremely expensive to perform. The drop test is very complex to analyse and computationally extremely costly since it involves large deformations, dynamics and and material failure. The tools for impact analysis have developed significantly and numerical simulations are now performed in parallel with experiments. The numerical simulations are also very useful in design since they allow the influence of modifications and different parameters to be assessed. A further aspect is that the understanding of the physical phenomena often require a combination of dedicated tests and associated analyses.

1.2.1 Transport regulations

According to IAEA §726, the 1 m drop onto a steel bar and the 9 meter drop test should be followed by a thermal test. The sequence and boundary conditions (drop orientations) of the two mechanical tests should be selected in such a way that they cause the maximum damage. For example, the functionability of a penetration protection is to be maintained after the 9 m drop. The boundary conditions for the test with the 1 m drop onto a steel bar are defined in §727(b). According to IAEA §637 and §664, a temperature range of -40°C to 70°C is to be considered.

1.2.2 Experiment

Based on the requirements of transport regulations a drop of the transport/storage cask from a height of 1 m onto a steel bar must be assessed. High strains occur in the cask body due to the locally induced load force from the bar. The location of the impact may affect the global deformation. Transport casks usually have cooling fins on parts of its outer surface. A question is then to what extent the overall response to an impact is affected by whether the impact occurred at a location with or without fins. It is difficult to model this due to the very complex geometries involved. Therefore two 1 meter drop tests were performed to quantify the influence of the circumferential fins on energy absorption and cask integrity. The experiments were performed on an old CASTOR AVR cask, Fig. 1.1, that scales almost perfectly to the targeted member of the CASTOR family (CASTOR V/19) by a geometrical ratio of 1:2.

The fins were machined away at two distinct locations, Fig. 1.2. The cask was dropped on the bar twice from 1 m height, Fig. 1.1. In the first test the impact point was at the finned part (*finned target*) and in the second test the impact point was in the area where the fins had been removed (*flat target*). The force under

the bar was measured in the vertical direction only. The cask accelerations were measured in two directions at two different positions. Strains were measured at the inside surface of the cask, directly above the impact area at 9 different locations by means of multi-axial strain gages.

Figure 1.1: *The CASTOR AVR cask and the set-up of the experiment (courtesy of GNS).*

(a) *(b)*

Figure 1.2: *The flat (a) and finned (b) target on the cask (courtesy of GNS).*

The main conclusions of the experiment were:

- impact duration is approximately 5 ms (25%) longer for the finned target drop,
- force in the force transducer below the bar is approximately 6% smaller for the finned target drop,
- both drops produce only elastic strains at the measurement points, with 21% lower strain amplitude for the finned target compared to the flat target.

1.2.3 Simulation tools

The commercial code ABAQUS is the main tool used for the FEM analysis in the SAFEWASTE action. It is currently running on a Linux Cluster. We have both the implicit and explicit versions installed and licensed, together with ABAQUS/CAE and VIEWER for pre- and post- processing the analyses.

The drop test is modelled with the parameter driven Python code inside the Abaqus/CAE software. ABAQUS/CAE is used as a pre-processor as well as a post-processor. ABAQUS/Explicit is used as solver for a given problem.

ABAQUS [3] is a suite of powerful engineering simulation programs, based on the finite element method, that can solve problems ranging from relatively simple linear analyses to the most challenging nonlinear simulations. ABAQUS contains an extensive library of elements that can model virtually any geometry. It has an equally extensive list of material models that can simulate the behavior of most typical engineering materials including metals, rubber, polymers, composites, reinforced concrete, crushable and resilient foams, and geotechnical materials such as soils and rock. Designed as a general-purpose simulation tool, ABAQUS can be used to study more than just structural (stress/displacement) problems. It can simulate problems in such diverse areas as heat transfer, mass diffusion, thermal management of electrical components (coupled thermal-electrical analyses), acoustics, soil mechanics (coupled pore fluid-stress analyses), and piezoelectric analysis.

ABAQUS/CAE [4] is a complete ABAQUS environment that provides a simple, consistent interface for creating, submitting, monitoring, and evaluating results from ABAQUS/Standard and ABAQUS/Explicit simulations. Python used by Abaqus/CAE is not the “standard Python” supported by the www.ptyhon.org, though the differences are small. ABAQUS Python adds more than 500 new data types to the “standard Python”.

Python, see www.ptyhon.org, is an easy to learn, powerful programming language. It has efficient high-level data structure and a simple but effective approach to object-oriented programming. Python’s elegant syntax and dynamic typing, together with its interpreted nature, makes it an ideal language for scripting and rapid application development in many areas on most platforms.

There are two major reasons for using ABAQUS Python scripts:

- to utilize the automatic meshing capabilities of ABAQUS/CAE and
- to use parametric approach for the geometry and mesh formation.

ABAQUS/Explicit is a solver for explicit dynamic problems and thus suited for the drop test simulation, see also [1].

1.2.4 Summary of the first report [1]

The report presents the initial and sensitivity numerical analysis of two one meter drop tests of a single ductile cast iron cask on a steel bar. In the first test, the impact is on the cask's cooling fins whereas in the second test the impact is in an area where the ribs have been locally machined away. The numerical analysis is based on explicit dynamic analysis using the commercial finite element code ABAQUS extended with Python scripts to allow a parametric description of the problem.

The analysis consists of two parts:

- a sensitivity analysis and
- a "blind-analysis" with assumed model parameters.

The "**blind-analysis**" (model without any knowledge of test results) was performed for the two drop tests. The overall behaviour predicted by the model is qualitatively very similar to what was observed during the experiments. The longer impact duration, approximately between 3 ms to 5 ms, when the cask is dropped on the fins compared to the flat target drop, is observed in both analysis and test. The reaction force at the bar's bottom surface from the computational model is qualitatively similar to the test. The peak force is overestimated by about 35%. On the contrary the measured strains inside the cask above the impact area are underestimated by the similar amount. The underestimation is partly attributed to the fact that the lid wasn't modeled and the total mass was therefore underestimated. The maximum strain is about 20% higher for the flat impact area in both simulation and experiment. The following list of possible improvements was compiled.

- Lid must be added to the model to ensure better inertia representation. This influences values of all variables under consideration.
- The mesh of the finned target should be refined.
- The mesh of the bar is also too coarse due to the same reasons as fins.
- The mesh pattern of the bar is not really optimal for the shape of the other body in contact in the case of the finned target area.
- The boundary conditions at the bar's bottom surface assume no friction in the contact between bar and the force transducer. It was shown that the simulated shape of the bar at its bottom surface is qualitatively different to the one observed during the experiment. The upper transducer's surface will have to be modelled and thus introducing another contact pair of surfaces.
- The artificial energy exceeds 10% of the total initial energy for the finned target drop. The influence of the different hourglass procedures should be examined.
- Only the tensile test material data are considered. The compression test data, lacking at the present, should also be incorporated in the material model.

The **sensitivity analysis** was performed to study the influence of parameters which either cannot be or were not defined directly from the experimental data, such as the friction coefficient, or which are linked to the FE numerical procedures, like the bulk viscosity. The analyses are set to determine the influence of the following parameters' variations on the model response:

- mesh element size;
- bulk viscosity;
- dry friction coefficient in contact formulation;
- element type;
- contact formulation;
- hourglass control; and
- boundary conditions at the bar's bottom surface.

Based on results, recommendations are given as:

- Tetrahedral elements should be avoided if possible.
- The experimental behaviour of the bar's bottom part lies in between the two bounding cases: free to slide with zero friction and encastered. A contact friction should be considered.
- The model with the finer mesh yields better results than the model with the coarser one, but needs more time to calculate the response.
- The friction coefficient value has a significant influence, in particular on the vertical reaction force. No value for coefficient of friction is available, but it could potentially be computed with an inverse numerical procedure based on the experimental data of the vertical reaction force or it could be measured by dedicated test.
- The default values of the bulk parameters in ABAQUS/Explicit should be decreased in order to decrease the artificial energy.
- The enhanced hourglass control seems to work relatively well for this analysis. The Kelvin - pure stiffness hourglass formulation should be avoided. The integral viscoelastic hourglass formulation gives the lowest artificial energy in the case of the finned target drop. The Kelvin - pure viscous hourglass formulation gives the lowest artificial energy in the case of the flat target drop. Due to relatively big discrepancies in displacement responses among models, verification with the experimental data must be done prior the final verdict. The analysis did not clearly indicate the optional hourglass control. However, the enhanced hourglass control is formulation of the choice at the moment.
- Mass scaling should be added to speed up lengthy analysis. The amount of mass scaling should be investigated first in order to avoid influencing the model's response too much. A compromise between speed and reliability of the results should be found (if there is any at all).

The report also gives the description of the model and material formulation as well as scripts and theoretical background about the explicit dynamics in ABAQUS.

Chapter 2

Model description

2.1 Introduction

The numerical modelling presented in this report is an extension of the work presented in [1]. The model is upgraded in line with the conclusions reported in [1], which implies:

- the lid is added as a new part,
- the force transducer upper surface is modelled as a rigid surface and thus forming frictional contact between the bar bottom and the force transducer top surface,
- the material data are slightly revised,
- the cask part 5 is partitioned in a way that the use of the tetrahedral elements in minimized (Fig. 2.1),
- the cask part 6 is divided into four parts in order to enable finer meshing and using of the hexagonal elements at the impact area (Fig. 2.2),
- best values for parameters identified in the report [1] are used.

In addition to model upgrade the influences of

- the value of the coefficient of friction at the contacts,
- the element size,
- the mass scaling and
- the shear failure mechanism

were studied.

Parametric model support allows the user to define geometry parameters, material parameters as well as analysis parameters such as mesh density in a way which can be easily modified for sensitivity studies.

The model consists of the cask's body, the lid and the bar supported at its bottom face by the ground (rigid surface). One symmetry plane is considered. The geometry description of the parts is given accompanied with the meshing description. The parts of the model are subsequently assembled and positioned. The analysis is then defined by initial and boundary conditions, loads and contact definition. The description of the model parameters, material data and structure of the script files can be found in the Appendices.

2.2 Model parts

The test system consist of 4 parts: the lid, the cask, the bar and the force transducer. The model consists of 12 parts. Nine parts make up the cask and the remaining three: the lid, the bar, and the top surface of the force transducer. Multiple parts are needed for the cask in order to mesh volumes more in accordance with their physical behaviour. Hence, different volumes are meshed differently; volumes near the impact point are meshed with finer mesh than volumes farther away.

2.2.1 Cask

Cask parts 5 and 6 are changed compared to [1] and presented here. All other cask parts are the same as in the report [1]. Cask part 5 is additionally partitioned which enabled use of the hexagonal elements over most of its volume (Fig. 2.1).

Cask part 6 (Fig. 2.2) is divided into four parts: 6a, 6b, 6c, 6d in order to to enable finer meshing and using the hexagonal elements at the point of impact and its vicinity. The tetragonal elements are used for meshing the 6d cask part for the flat target only. The element size can be controlled for each part separately.

2.2.2 Bar

The bar remains the same as in [1].

2.2.3 Lid

The lid has been added to the model. It is shown in Fig. 2.3.

2.2.4 Ground

The part named ground has been added to the model to simulate the top surface of the force transducer. The frictional contact between the bar and the transducer is formed in this way. The ground is modelled as a rigid immovable surface (Fig. 2.4).

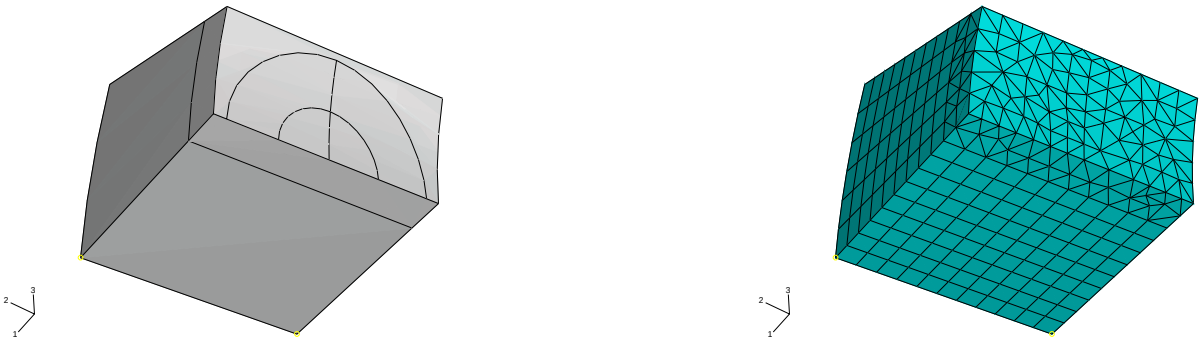

Figure 2.1: *The geometrical representation and the mesh of the part 5 of the cask.*

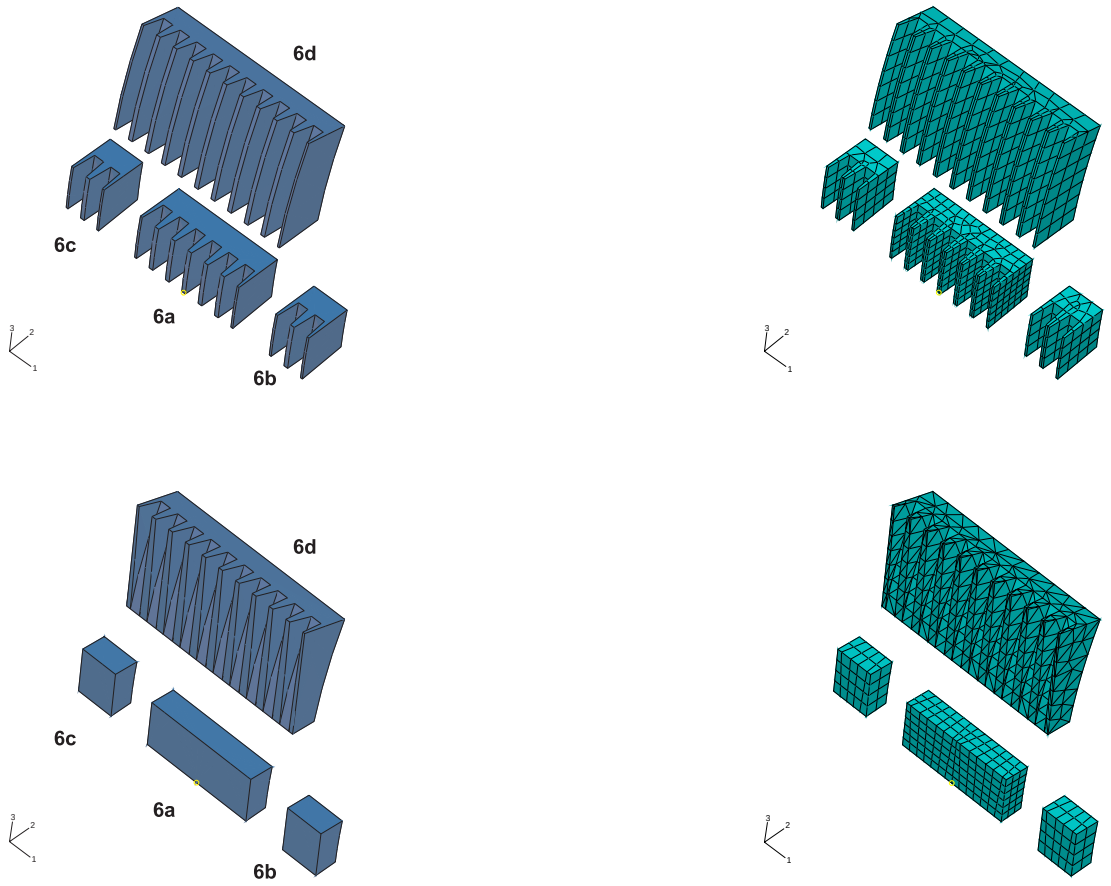

Figure 2.2: *The geometrical representation and the mesh of the parts 6a, 6b, 6c and 6d of the cask. Finned target area at the top and flat one at the bottom.*

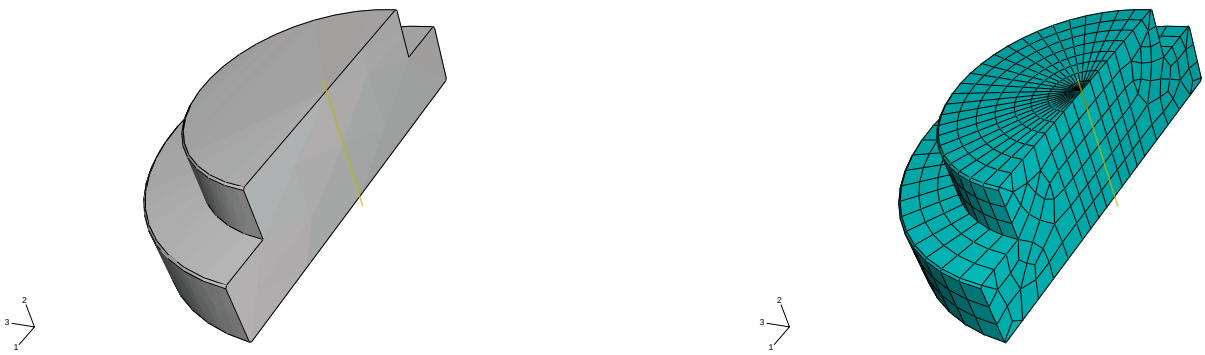

Figure 2.3: *The geometrical representation and the mesh of the lid part.*

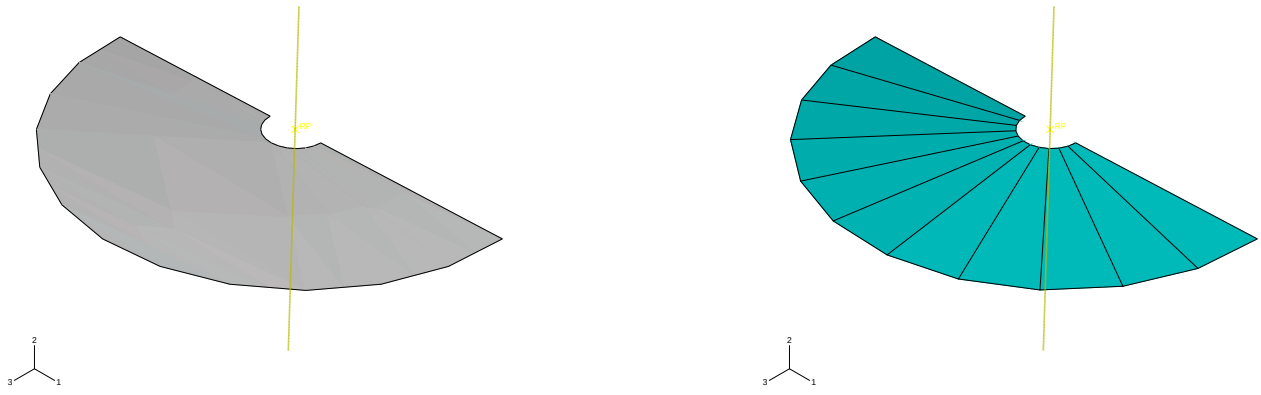

Figure 2.4: *The geometrical representation and the mesh of the ground part.*

2.3 Model assembly

The model assembly is shown in Fig. 2.5. Parts of the cask are connected by the tie command, tying adjacent surfaces of the parts. Tie constraints tie two separate surfaces together so that there is no relative motion between them. The nodes on the slave surface are constrained to have the same value of displacement, temperature, pore pressure, or electrical potential as the point on the master surface to which they are tied. The surface with the finer mesh is selected to be the slave surface.

2.3.1 Initial conditions

The initial conditions are the same as in [1].

2.3.2 Boundary conditions

Two different kinds of boundary conditions are used:

- for defining model's symmetry plane and
- for defining model's support.

The symmetry boundary conditions are the same as in [1] but the support boundary conditions are significantly changed.

Support boundary conditions
The bar is screwed into the force transducer in the experimental set-up. The force transducer is considered as rigid and the contact between the transducer and bar is modelled by three different boundary conditions:

- fixing all degrees of freedom on the bar's bottom surface where the bolt is, and fixing only the vertical displacement (axis 2) over the remaining part of the bar's bottom surface (Fig. 2.6),
- fixing all degrees of freedom on the entire bar's bottom surface, i.e. $u_1 = u_2 = u_3 = 0$, or
- introducing the rigid surface and frictional contact at the bars's bottom surface. The degrees of freedom at the bar's bottom surface, where the bolt is located, are still fixed (encastre). The ground is completely rigid and fixed. The contact takes place on the portion of the bar's bottom surface where $u_2 = 0$ is pointing to (see Fig. 2.6).

2.3.3 Loads

The only load defined in the model is volume force (acceleration) due to gravity, as in [1].

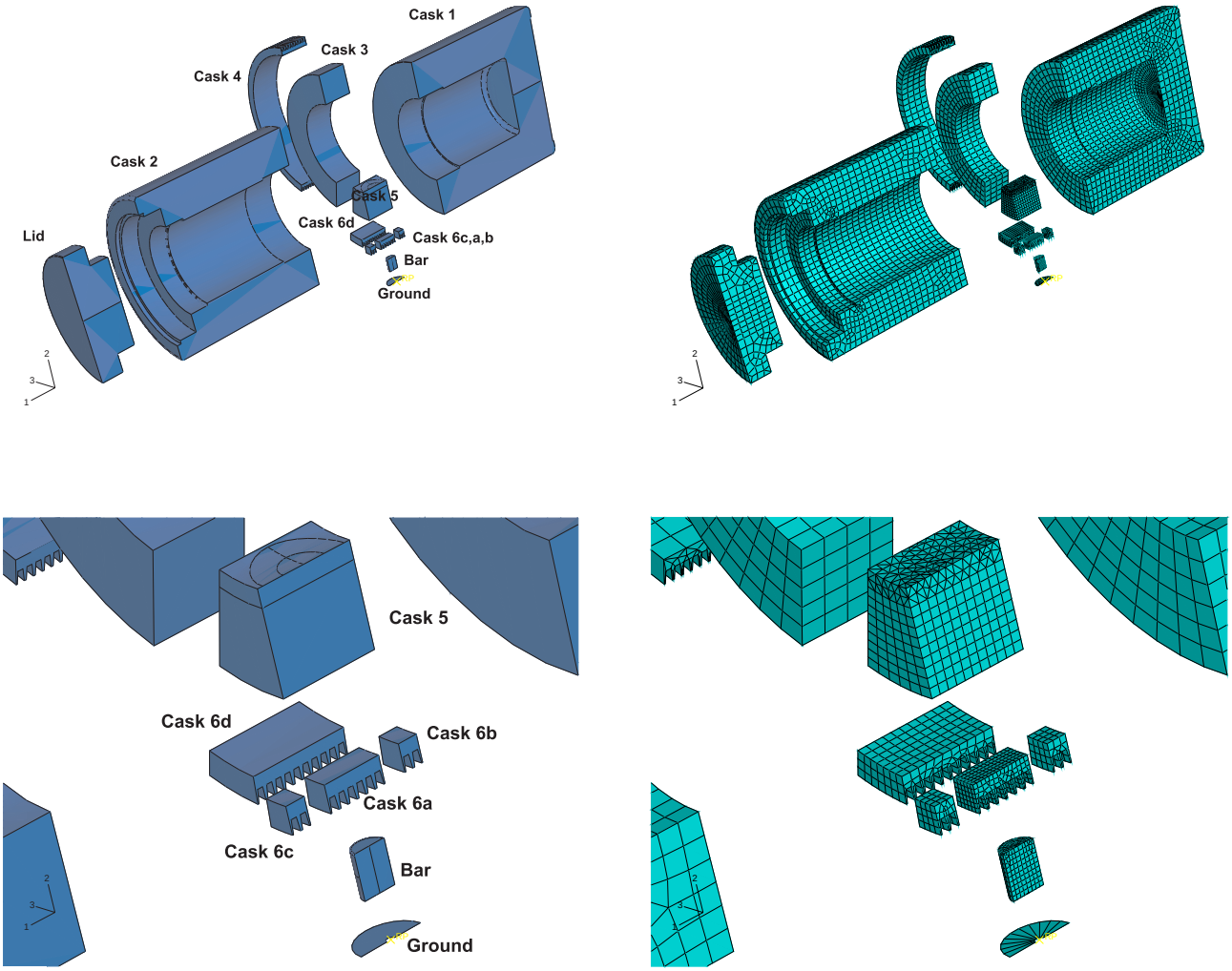

Figure 2.5: *The expanded geometrical representation and the mesh of the assembly of the model (detail at the bottom).*

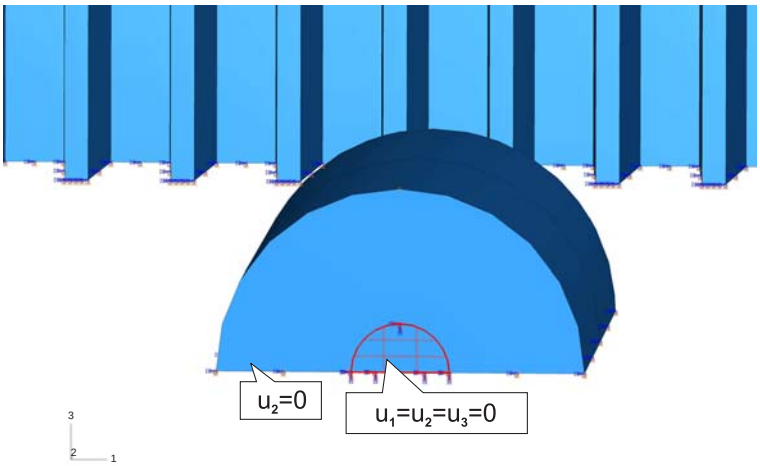

Figure 2.6: *Support boundary conditions on the bar's bottom surface; fixed degree of freedom in all directions (encastre) on the hatched surface and fixed ones only in the vertical (axis 2) direction on the rest of the surface.*

2.3.4 Contact definition

The general contact algorithm, which is very powerful and highly automated, is used for contact formulation during the impact between the cask and the bar (see also [1]). When the ground part is modelled, the additional surface to surface contact is formulated on the basis of the penalty method. This contact pair is excluded from the general contact algorithm, thus allowing a user to specify different coefficient of friction for different contact areas, e.g. between the cask and the bar and between the ground and the bar.

Chapter 3

Simulation results

3.1 Introduction

A Base Model presented here is defined based on conclusions of the report [1]. An additional parametric sensitivity study of the model is also presented in this chapter. First, the comparison of Base Model to Model **a** from [1] is presented. The sensitivity of the model on variations of the following parameters is studied afterwards. The analyses encompass:

- variation of the support boundary conditions;
- variation of the coefficient of friction between the bar and the force transducer;
- variation of the material model;
- variation of the mass scaling factor; and
- variation of the element size.

Some of these parameters have strong physical background like defining the boundary conditions and material model. Others are tied to the numerical method within the FEM by defining the element size and mass scaling factor.

The different model responses were obtained at different locations named as follows:

- CSK1 - point on the cask at the opposite side of the contact point, Fig. A.1;
- CSK3 - contact point on the cask, Fig. A.1;
- D1 - point inside the cask above the contact point, Fig. A.4;
- PIN4 - point at the edge of the bar's bottom surface, Fig. A.6.

3.2 Comparative analysis of Base Model and Model a

The results for the Base Model are given in this section together with Model **a** from [1]. The values of the parameters are presented in Tab. 3.1

Table 3.1: *Parameter values of Base Model and Model **a** [1].*

Parameter	Unit	Base Model	Model **a**
dropDuration	ms	35	35
dropHeight	m	1.006-eps	1.006-eps
dropFreq	/	10	10
dropDataFreq	/	1	1
anaMassScaling	/	0 (none)	0 (none)
anaTimeStep	s	10^{-7}	10^{-7}
anaLinBulkVis	/	0.03	0.06
anaQuadBulkVis	/	0.6	1.2
anaFricCoef	/	0.2	0.3
anaFricCoefGround	/	0.2	/
anaElementType	/	0 (hex)	0 (hex)
anaContactMethod	/	0 (penalty)	0 (penalty)
anaHourglassControl	/	0 (enhanced)	0 (enhanced)
anaSupportBC	/	2 (contact formulation)	0 (encastre @ screw)
_cskElementSize_1	mm	50	50
_cskElementSize_2	mm	50	50
_cskElementSize_3	mm	50	50
_cskElementSize_4	mm	50	50
_cskElementSize_5	mm	20	20
_cskElementSize_6	mm	/	15
_cskElementSize_6a	mm	10	/
_cskElementSize_6b	mm	15	/
_cskElementSize_6c	mm	15	/
_cskElementSize_6d	mm	20	/
_pinElementSize	mm	10	10

Four different energies of the complete model are considered and compared for the models: artificial, total, kinetic and strain, see Fig. 3.1. A comparison of the reaction forces in the vertical directions is shown in Fig. 3.2, together with the maximal principal strains at the D1 measurement point. Vertical displacements at the points CSK1 and CSK3 are compared in Fig. 3.3. Vertical velocities at the points CSK1 and CSK3 are compared in Fig. 3.4. Horizontal displacements at the point PIN4 are compared in Fig. 3.5.

The artificial energy of Base Model is smaller then for Model **a**. Preservation of the total energy of Base Model is much better than for Model **a**. The total energy of Base Model is larger than for Model **a**, due to the lid mass. The same is true for the kinetic as well as for strain energy, but the difference is much smaller. The values of the vertical reaction forces are surprisingly smaller for Base Model than for Model **a** in spite of its

larger model mass. However, the contrary the maximal principal strains at the measuring point D1 are larger for Base Model than for Model **a**. The vertical displacements of Base Model are larger compared to Model **a**. There is a big difference between the models when comparing horizontal displacements at the bottom surface of the bar. This is due to the different supporting boundary conditions of the models. There is no significant difference when comparing vertical velocities at CSK1. But the vertical velocity at the CSK3 (contact between the cask and the bar) oscillates more for Base Model compared to Model **a** due to its smaller value of the coefficient of friction.

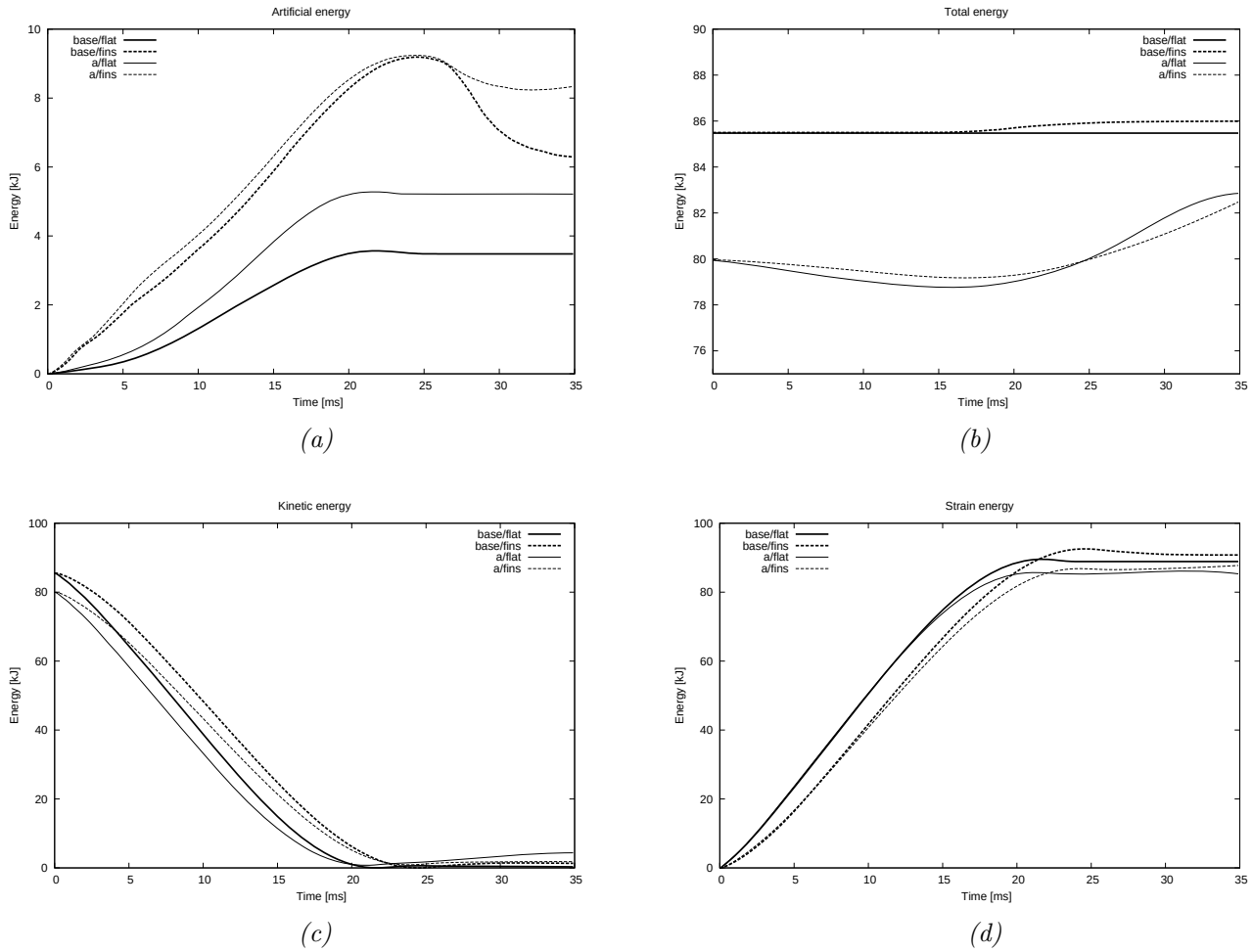

Figure 3.1: *Base Model and Model* ***a****: comparison of the artificial (a), total (b), kinetic (c) and strain energy (d).*

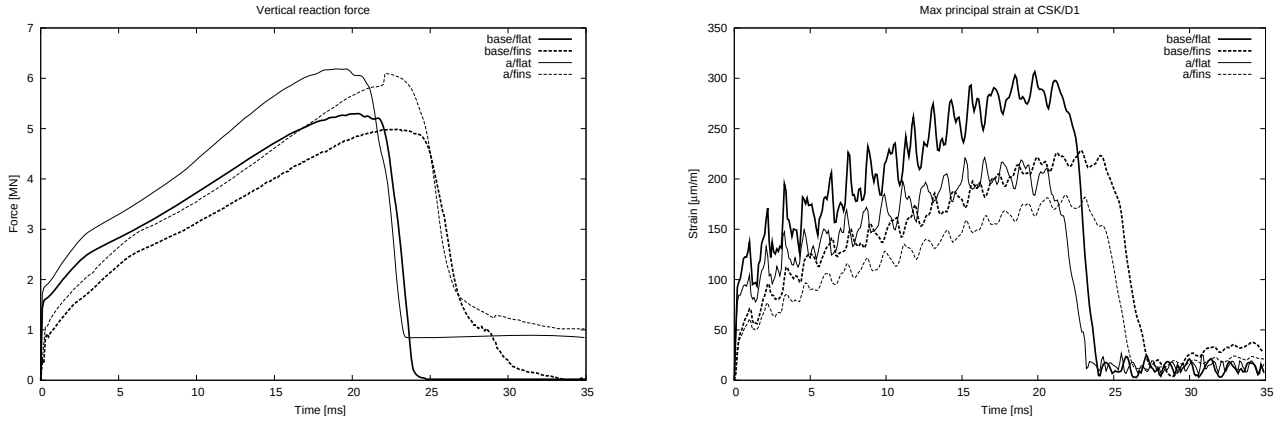

(a) *(b)*

Figure 3.2: *Base Model and Model* ***a****: comparison of the vertical reaction forces (a) and maximal principal strains at the D1 (b).*

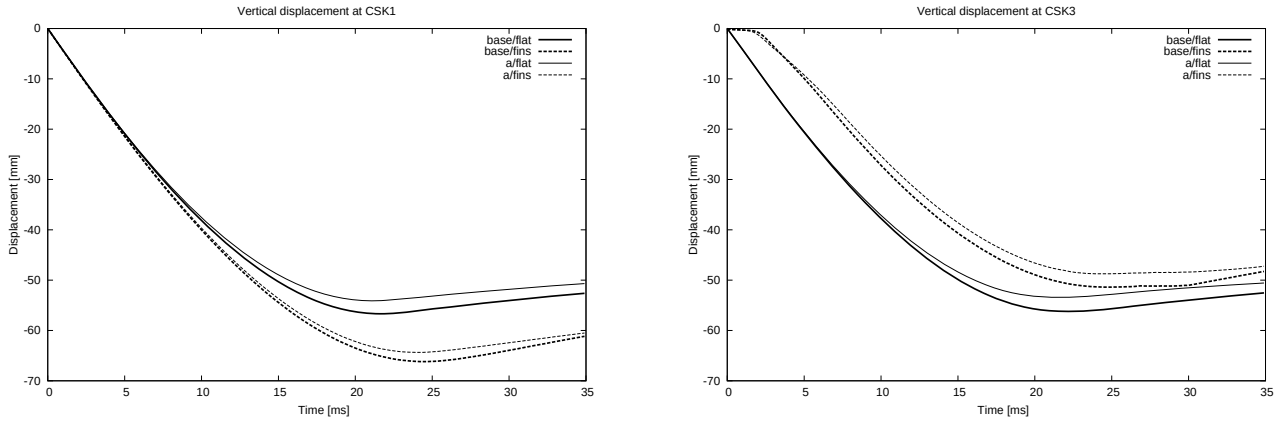

(a) *(b)*

Figure 3.3: *Base Model and Model* ***a****: comparison of the vertical displacements at the CSK1 (a) and at the CSK3 (b).*

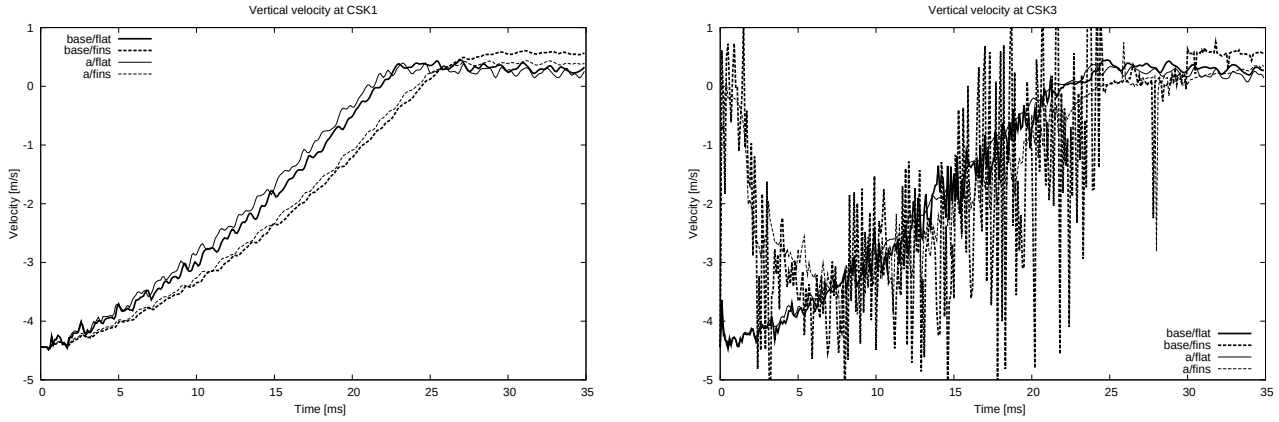

(a) *(b)*

Figure 3.4: *Base Model and Model* ***a****: comparison of the vertical velocities at the CSK1 (a) and at the CSK3 (b).*

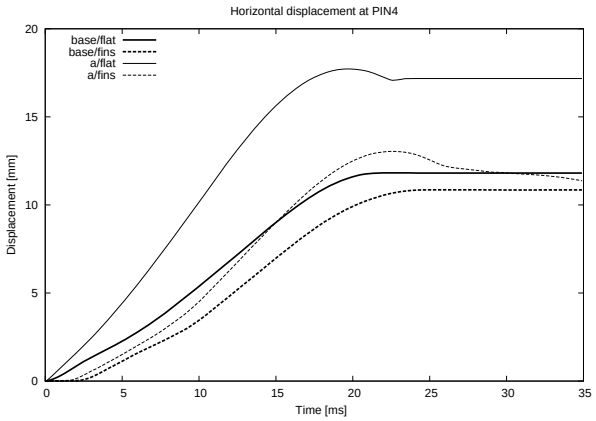

Figure 3.5: *Base Model and Model* ***a****: comparison of the horizontal displacements at the PIN4.*

3.3 Influence of the different types of the boundary conditions between the bar and the force transducer

The supporting boundary condition (BC) of the model has been upgraded in this report by the contact between bottom bar surface and top force transducer's surface. The results of the revised boundary condition is compared to two boundary conditions in [1], which presents bounding cases of the contact between the bar and the force transducer. Two additional BCs are applied to Base Model. Model *bc-1* applies the supporting boundary condition by fixing all degrees of freedom on the bar's bottom surface, where the bolt is, and fixing only the vertical displacement (axis 2) over the remaining part of the bar's bottom surface (as Model **a** in [1]). Model *bc-2* applies the supporting boundary condition as Model **j** in [1] by fixing all degrees of freedom on the bar's bottom surface. See also Fig. 2.6. All three supporting boundary conditions presume absolute rigidity of the force transducer.

Four different energies of the complete model are considered and compared for the models, see Fig. 3.6: artificial, total, kinetic and strain. A comparison of the reaction forces in the vertical directions is shown in Fig. 3.7, together by the maximal principal strains at the D1 measurement point. Vertical displacements at the points CSK1 and CSK3 are compared in Fig. 3.8. Vertical velocities at the points CSK1 and CSK3 are compared in Fig. 3.9. Horizontal displacements at the point PIN4 are compared in Fig. 3.10.

Artificial energy for Base Model lies between models *bc-1* (the upper bound) and *bc-2* (the lower bound). There are no significant differences in the total, kinetic and strain energies. Base Model exhibits the biggest values of the vertical reaction forces. The differences are up to 10%. There are rather small differences when comparing the maximal principal strains at the measuring point D1.

Vertical displacements of Base Model at CSK1 and CSK3 are in-between the model *bc-1* (the upper bound) and the model *bc-2* (the lower bound). The differences are in range of few millimeters. The same is true for the vertical velocities at CSK1 where the differences are in range of few dm/s. The time histories of the vertical velocities at CSK3 are heavily influenced by the frictional contact. The influence is visible in the oscillations of

the time histories. The horizontal displacement at PIN4 of the base model is almost identical to the one of the *bc-2*.

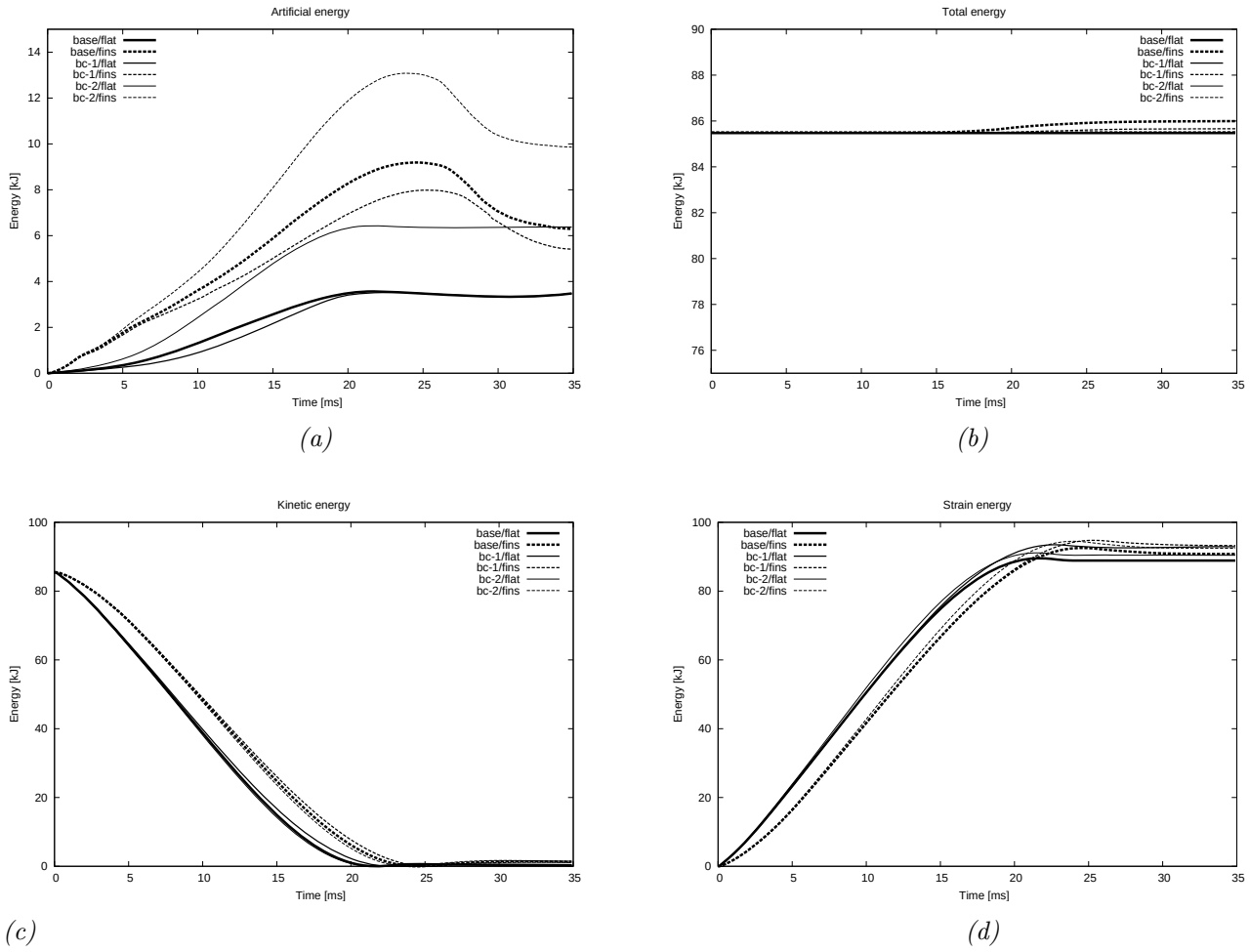

Figure 3.6: *Base Model and models bc-1 and bc-2: comparison of the artificial (a), total (b), kinetic (c) and strain energy (d).*

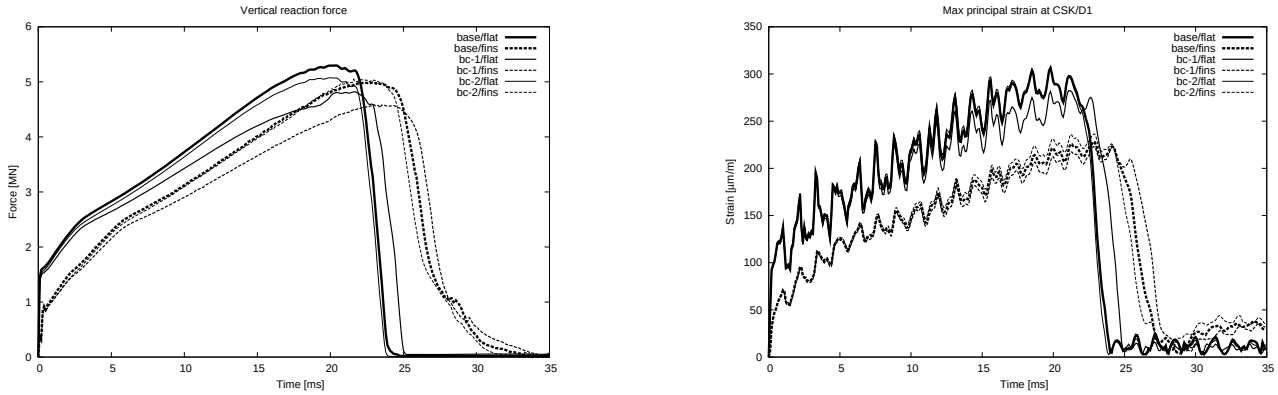

(a) *(b)*

Figure 3.7: *Base Model and models bc-1 and bc-2: comparison of the vertical reaction forces (a) and maximal principal strains at the D1 (b).*

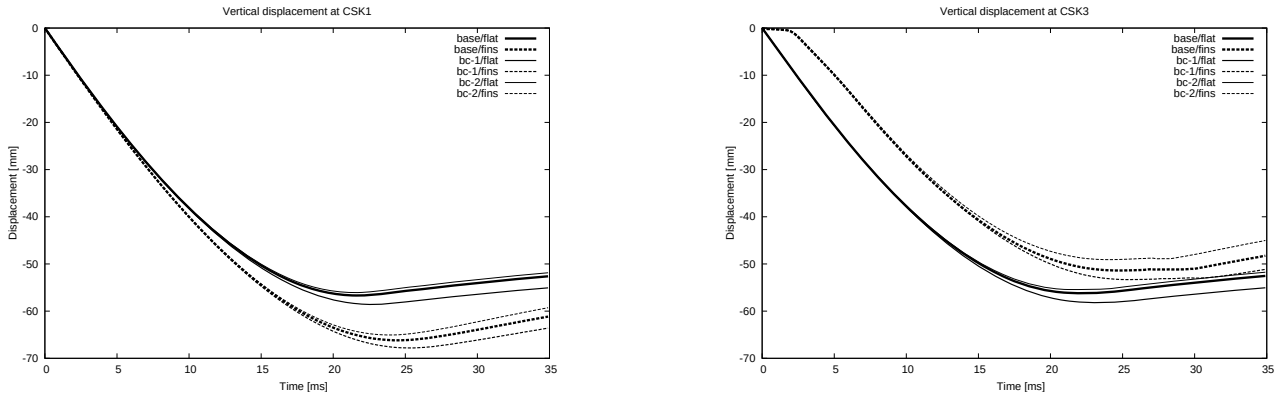

(a) *(b)*

Figure 3.8: *Base Model and models bc-1 and bc-2: comparison of the vertical displacements at the CSK1 (a) and at the CSK3 (b).*

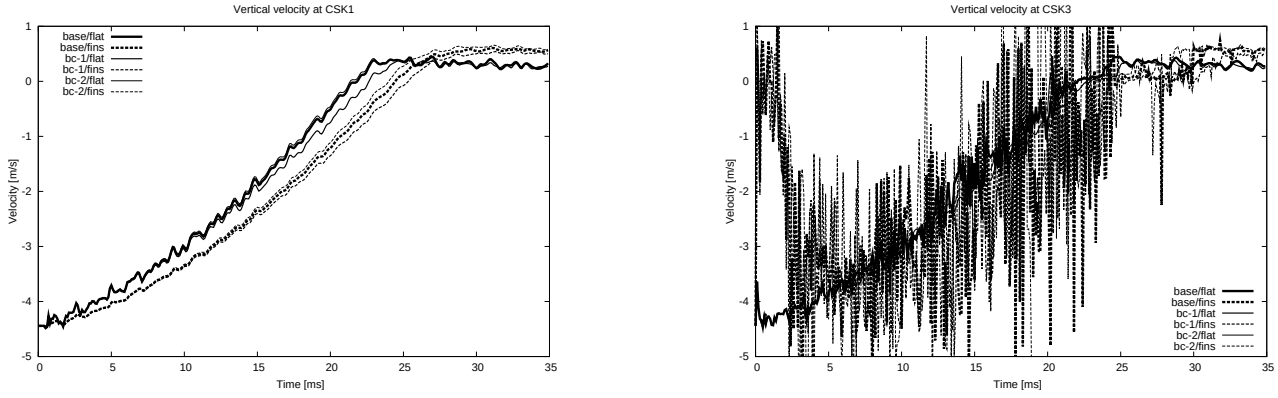

(a) *(b)*

Figure 3.9: *Base Model and models bc-1 and bc-2: comparison of the vertical velocities at the CSK1 (a) and at the CSK3 (b).*

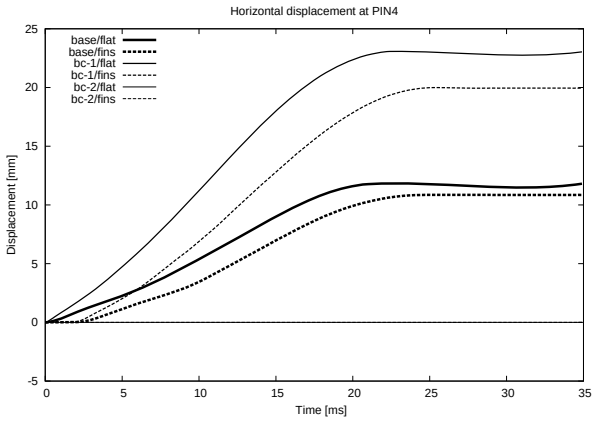

Figure 3.10: *Base Model and models bc-1 and bc-2: comparison of the horizontal displacements at the PIN4.*

3.3.1 Comparison of different models of bar-force transducer set-up

The comparison of the models *bc-1* and *bc-2* with the Base Model and the models *cf-0* and *cf-1* which are equivalent to the Base model with the values of the coefficient of friction between the bar and the ground $\mu = 0$ and $\mu = 1$ respectively. Models *bc-1* and *cf-0* model the same physical set-up in two different ways. The same is true for models *bc-2* and *cf-1*.

A comparison of the reaction forces in the vertical direction is shown in Fig. 3.11. The maximal principal strains at the D1 measurement point are shown in Fig. 3.12. Horizontal displacements at the point PIN4 are compared in Fig. 3.13.

The differences between models *bc-1* and *cf-0* and as well for models *bc-2* and *cf-1* are most pronounced for the vertical reaction force and much less pronounced for the maximal principal strains at the D1 and the horizontal displacements at the PIN4 when analyzing the finned drop case. On the contrary, there are almost no differences for the flat drop case when comparing the maximal principal strains at the D1 and the horizontal displacements at the PIN4. The differences between models *bc-1* and *cf-0* and as well for models *bc-2* and *cf-1* are due to different bar-force transducer set-up modelling. The models *cf* corresponds better to what we expect to be proper physical behavior.

The qualitative comparison between simulation and experiment shows that the final shape of the bar is best simulated with the frictional contact formulation of the Base model, Fig. 3.14.

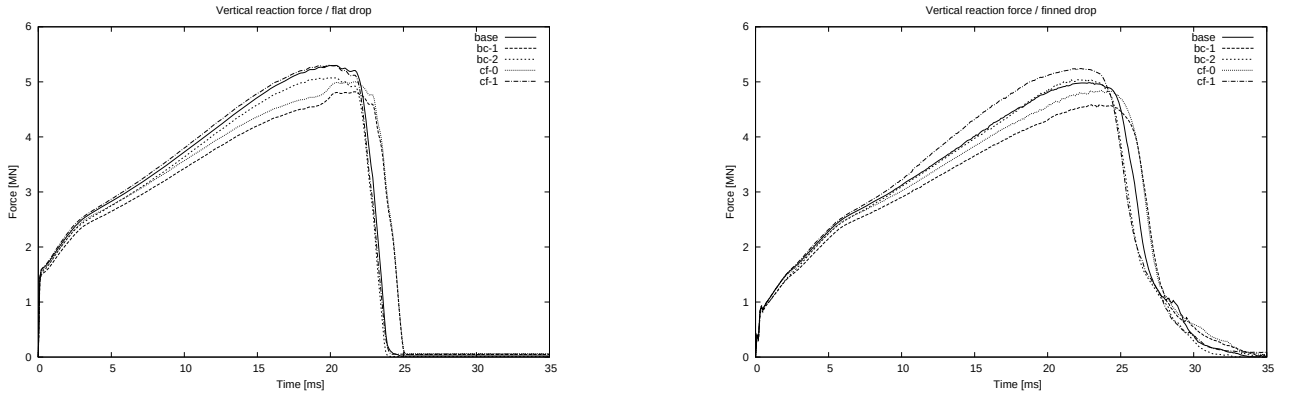

(a) *(b)*

Figure 3.11: *Base Model and models bc-1, bc-2, cf-0 and cf-1: comparison of the vertical reaction forces; flat (a) and finned target (b).*

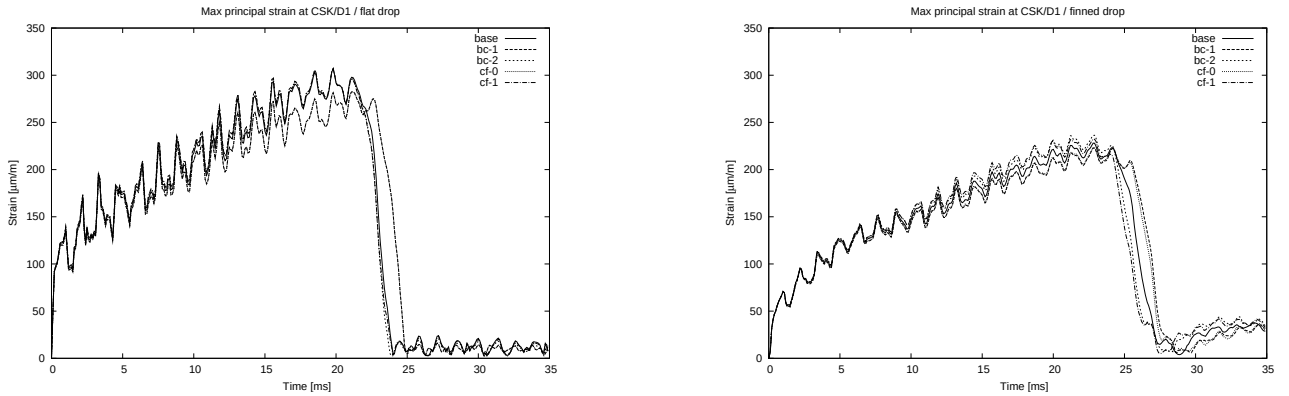

(a) *(b)*

Figure 3.12: *Base Model and models bc-1, bc-2, cf-0 and cf-1: comparison of the maximal principal strains at the D1; flat (a) and finned target (b).*

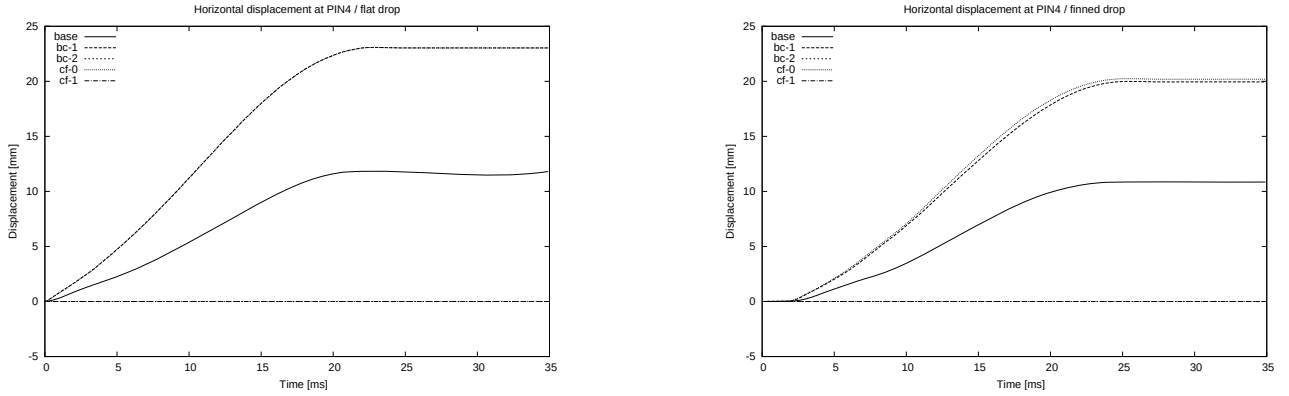

(a) *(b)*

Figure 3.13: *Base Model and models bc-1, bc-2, cf-0 and cf-1: comparison of the horizontal displacements at the PIN4; flat (a) and finned target (b).*

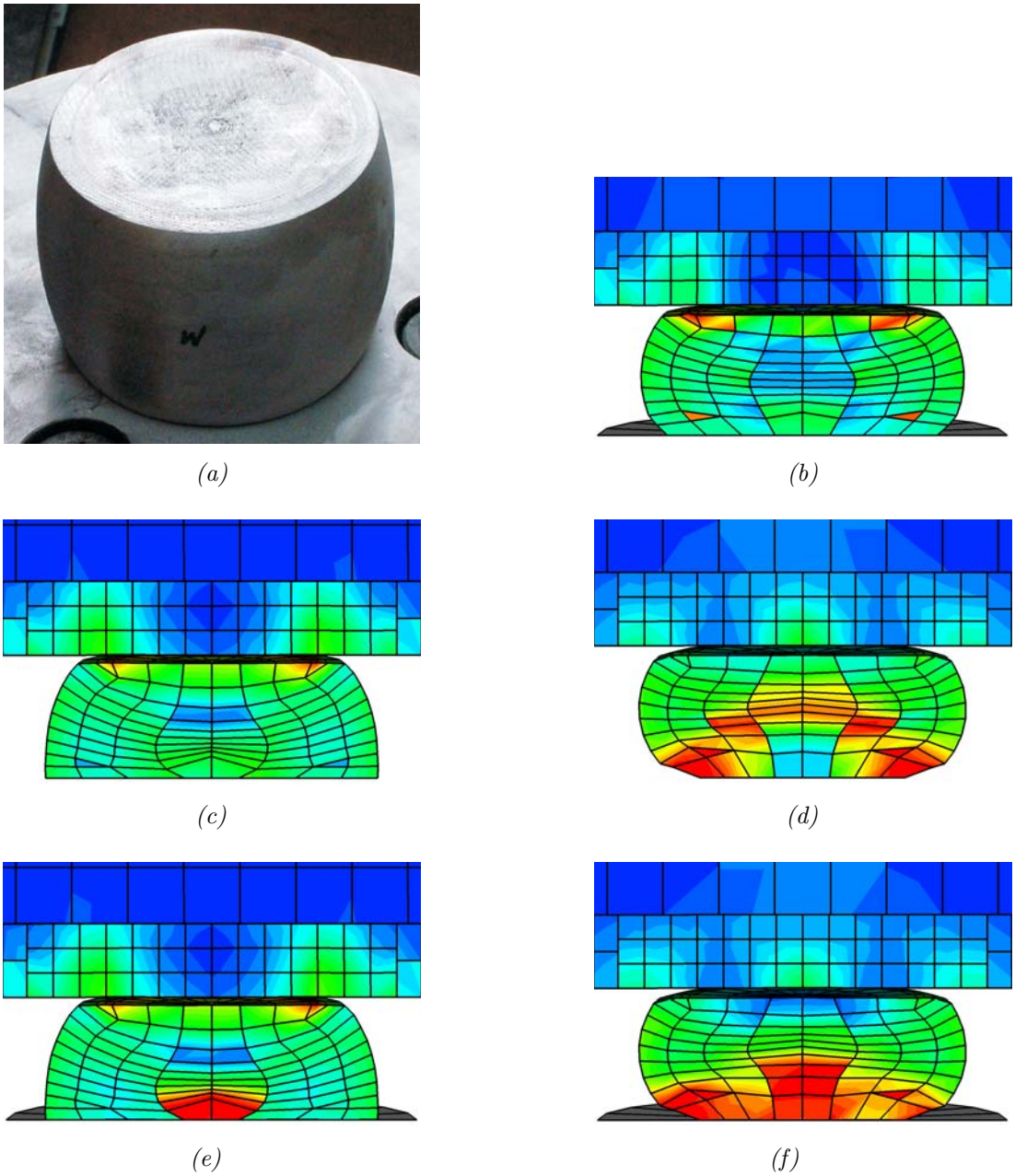

(a) *(b)* *(c)* *(d)* *(e)* *(f)*

Figure 3.14: *Final bar shape: Experiment (a), Base model (b), Model bc-1 (c), Model bc-2 (d), Model cf-0 (e) and Model cf-1(f).*

3.4 Influence of the different values of the coefficient of friction in the contact areas

The coefficient of friction is varied between values of 0.05 and 0.3 (see Tab. 3.2). The coefficient of friction is varied in both contact regions; between the cask and the bar and between the bar and the ground.

Table 3.2: *Models and associated coefficient of friction.*

Model name	Value of the coefficient of friction
bf-05	0.05
bf-10	0.10
bf-15	0.15
base	0.20
bf-25	0.25
bf-30	0.30

The artificial, total, kinetic and strain are presented in Fig. 3.15, 3.16, 3.17 and 3.18 respectively. A comparison of the reaction forces in the vertical directions is shown in Fig. 3.19 and the maximal principal strains at the D1 measurement point in Fig. 3.20. Vertical displacements at the points CSK1 and CSK3 are compared in Fig. 3.21 and 3.22 respectively. Vertical velocities at the points CSK1 and CSK3 are compared in Fig. 3.23 and 3.24. Horizontal displacements at the point PIN4 are compared in Fig. 3.25.

Less friction in the contact means less artificial energy. There are no significant differences in the total, kinetic and strain energy. The vertical reaction force vary moderately with the coefficient of friction; the larger the coefficient of friction the larger the maximal value of the reaction force. The differences are in range of 5% to 10%. There are rather small differences between the maximal principal strains at the measuring point D1.

Vertical displacements at CSK1 and CSK3 are in between Model *bc-1* (the upper bound) and Model *bc-2* (the lower bound). The differences are in range of few millimeters (±5% of Base Model values). The same is true for the vertical velocities at CSK1 where the differences are in range of few dm/s. The time histories of the vertical velocities at CSK3 are heavily influenced by the frictional contact. The influence is visible in the oscillations of the time histories. The horizontal displacement at PIN4 of the base model is placed in between others as dictated by the coefficient of friction. It is clear that coefficient of friction influences the horizontal displacement of the PIN4 point. The difference between models *bf-05* and *bf-30* is more than a factor 2.

Linear approximation by means of the least mean squares of the bar's horizontal displacement of the point PIN4 as function of the coefficient of friction is presented in Fig. 3.26 for the flat drop case and in Fig. 3.27 for the finned drop case. The approximation data are compiled in Tab. 3.3, where r^2 stands for the correlation coefficient and χ^2 for the value of the merit function. The linear model is presented by the equation $y = a_0 + a_1\, x$, where a_0 and a_1 are model parameters, y [m] denotes bar's horizontal displacement of the point PIN4 and x denoted the coefficient of friction. It is clear that the horizontal displacement of the bar's point PIN4 scales linearly with the coefficient of friction in both drop targets. Hence, only two different simulations for each drop target are enough for fine tuning the coefficient of friction for the mesh used.

Consistent value of the coefficient of friction is approximately 0.08.

Table 3.3: *Line ($y = a_0 + a_1\, x$) fitting results to displacement-coefficient of friction data for both drop types.*

Drop type	a_0 [m]	a_1 [m]	r^2	χ^2
flat	0.019405	-0.037974	0.9965	$1.776 \cdot 10^{-7}$
finned	0.019929	-0.044408	0.9977	$1.566 \cdot 10^{-7}$

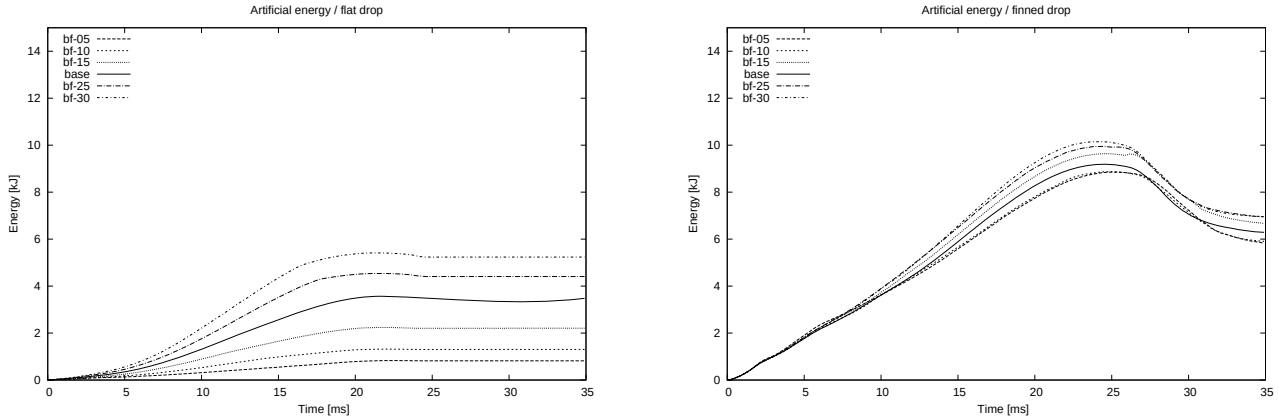

(a) *(b)*

Figure 3.15: *Computed artificial energy for different coefficients of friction: flat (a) and finned target (b).*

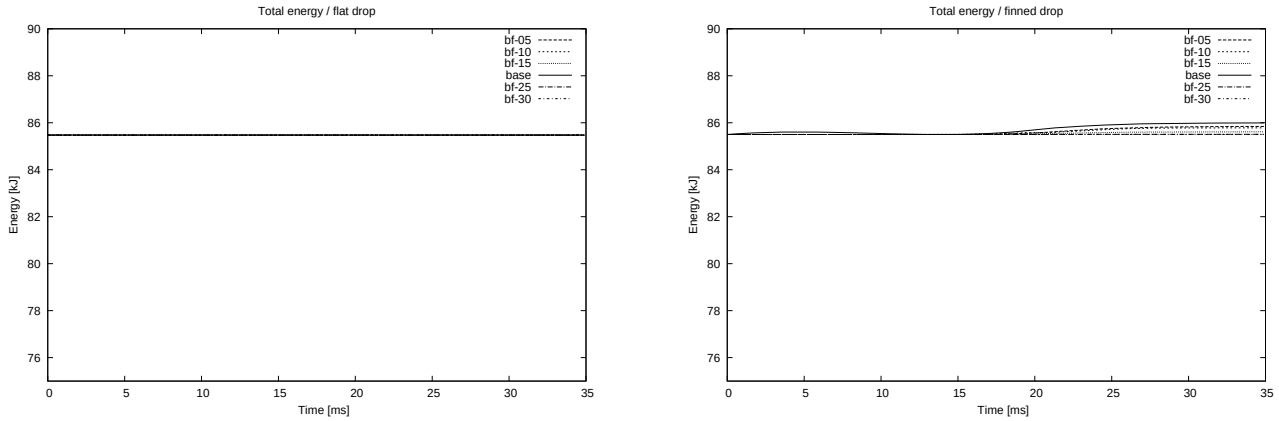

(a) *(b)*

Figure 3.16: *Computed total energy for different coefficients of friction: flat (a) and finned target (b).*

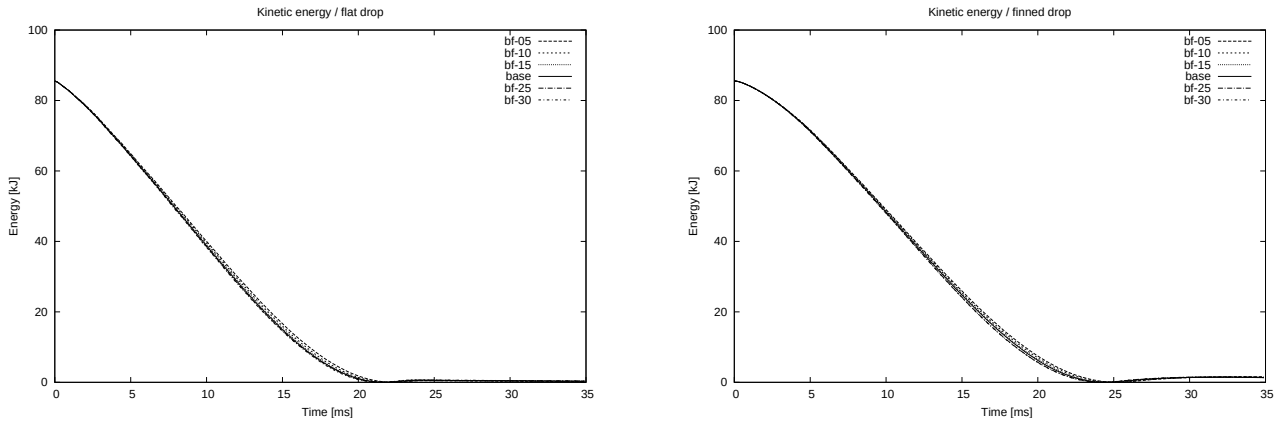

(a) *(b)*

Figure 3.17: *Computed kinetic energy for different coefficients of friction: flat (a) and finned target (b).*

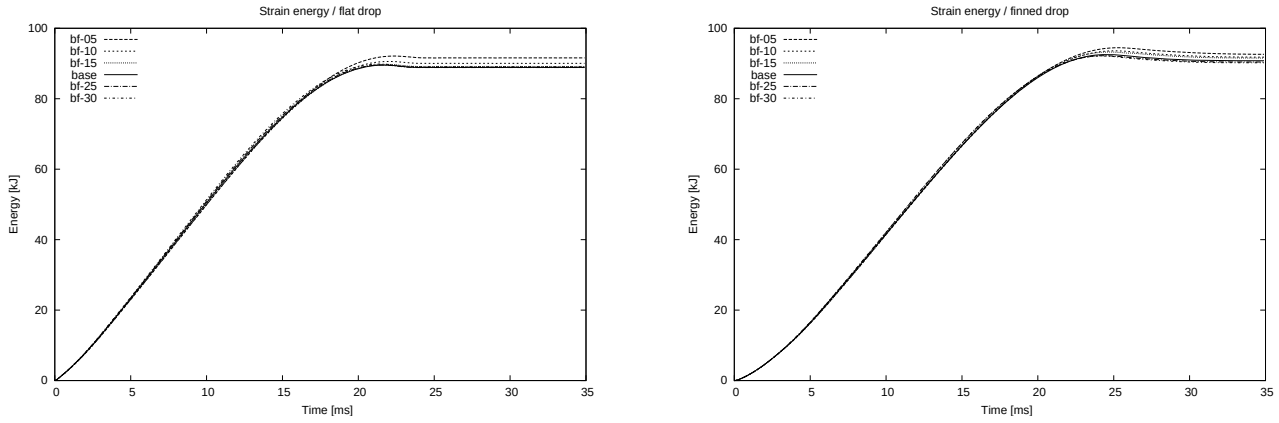

(a) *(b)*

Figure 3.18: *Computed strain energy for different coefficients of friction: flat (a) and finned target (b).*

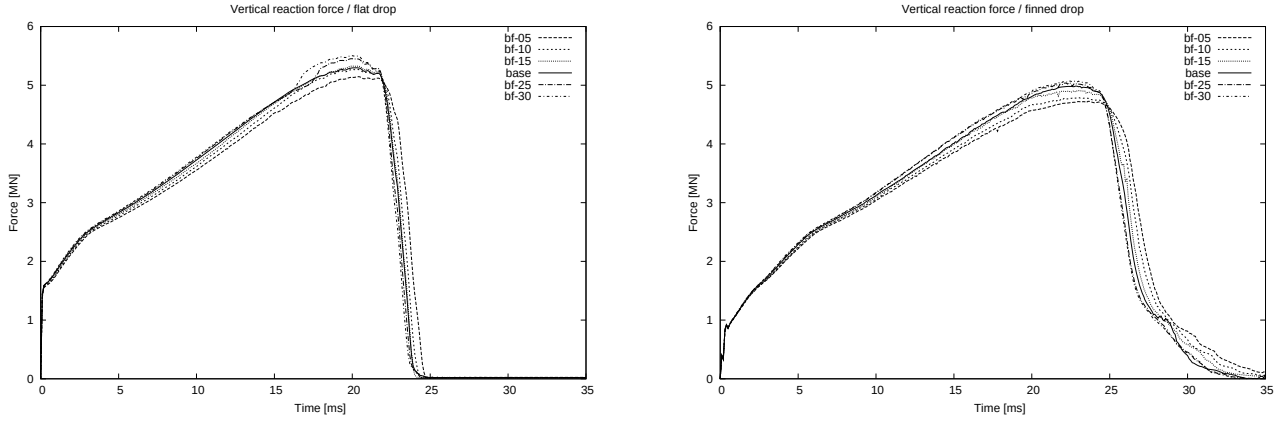

(a) *(b)*

Figure 3.19: *Computed vertical reaction forces for different coefficients of friction: flat (a) and finned target (b).*

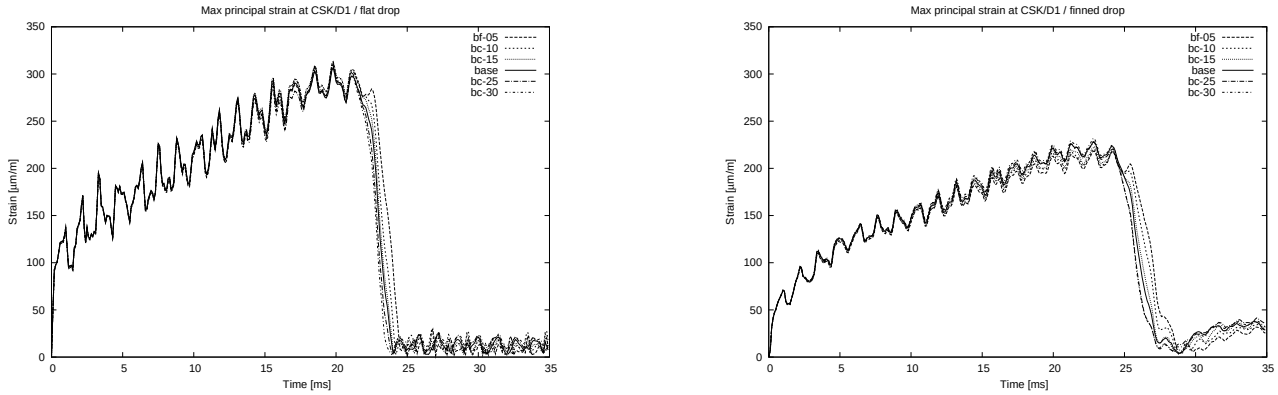

(a) *(b)*

Figure 3.20: *Computed maximal principal strains at the D1 for different coefficients of friction: flat (a) and finned target (b).*

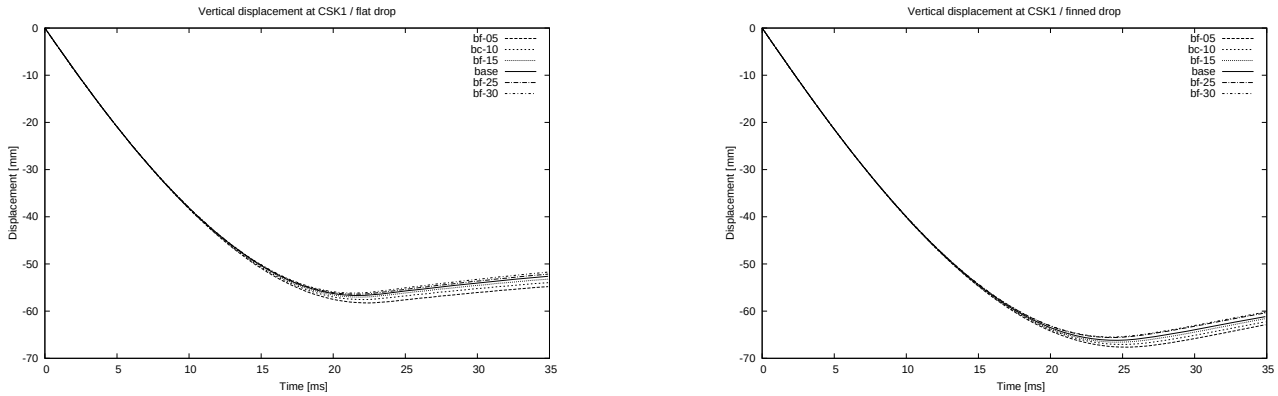

(a) *(b)*

Figure 3.21: *Computed vertical displacements at the CSK1 for different coefficients of friction: flat (a) and finned target (b).*

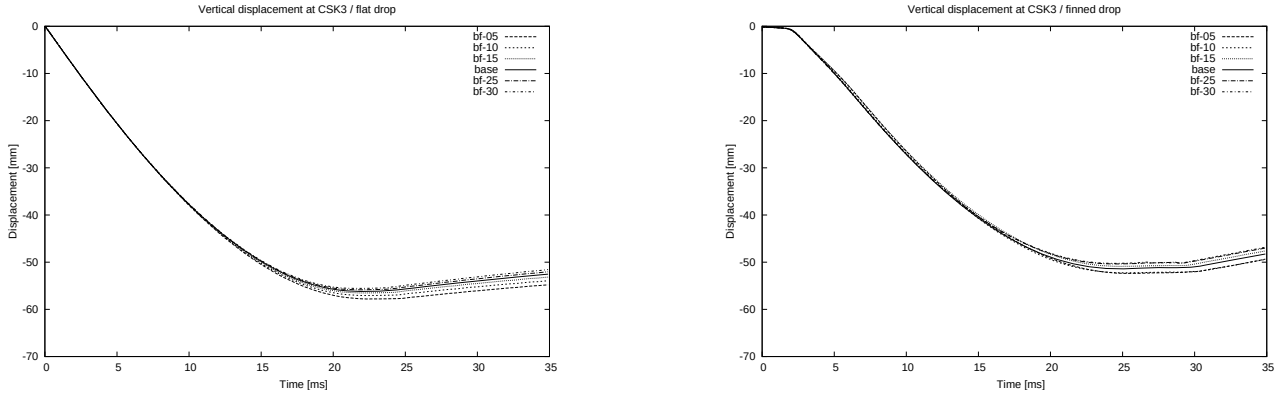

(a) *(b)*

Figure 3.22: *Computed vertical displacements at the CSK3 for different coefficients of friction: flat (a) and finned target (b).*

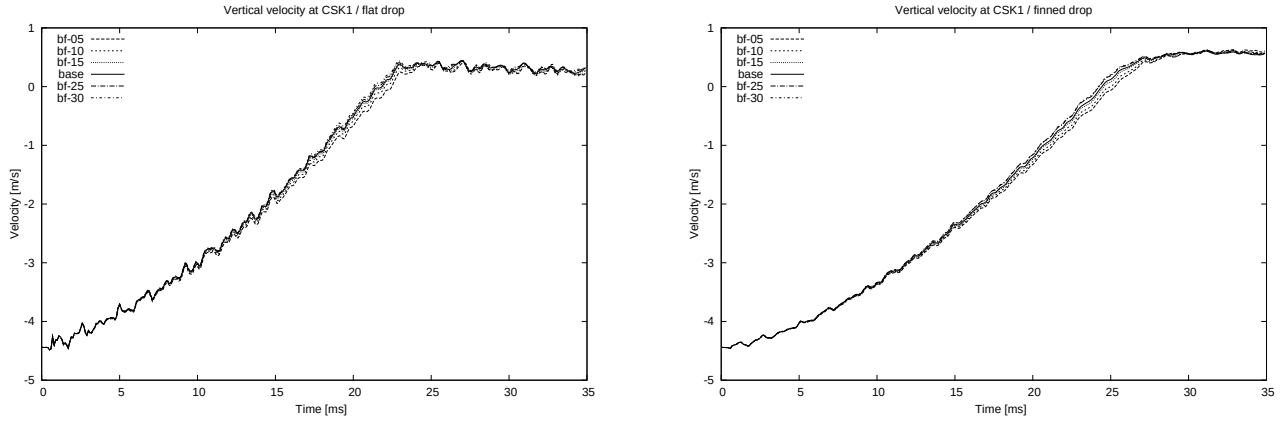

(a) *(b)*

Figure 3.23: *Computed vertical velocity at the CSK1 for different coefficients of friction: flat (a) and finned target (b).*

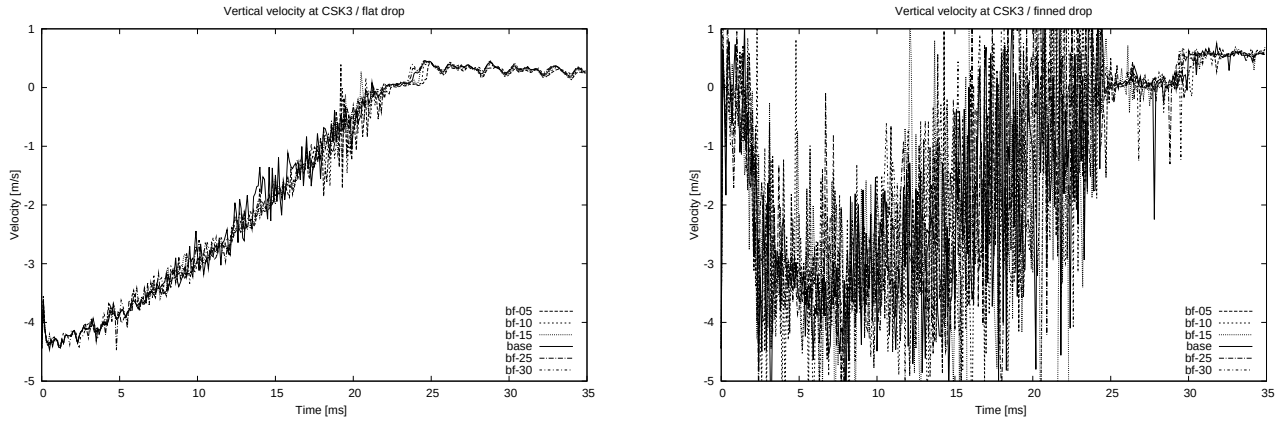

(a) *(b)*

Figure 3.24: *Computed vertical velocity at the CSK3 for different coefficients of friction: flat (a) and finned target (b).*

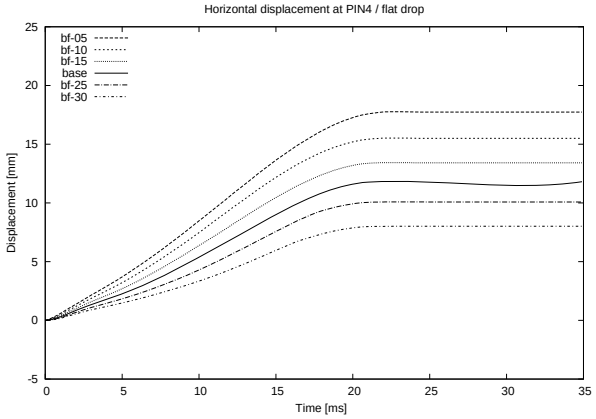

Figure 3.25: *Computed horizontal displacement at the PIN4 for different coefficients of friction for the flat target.*

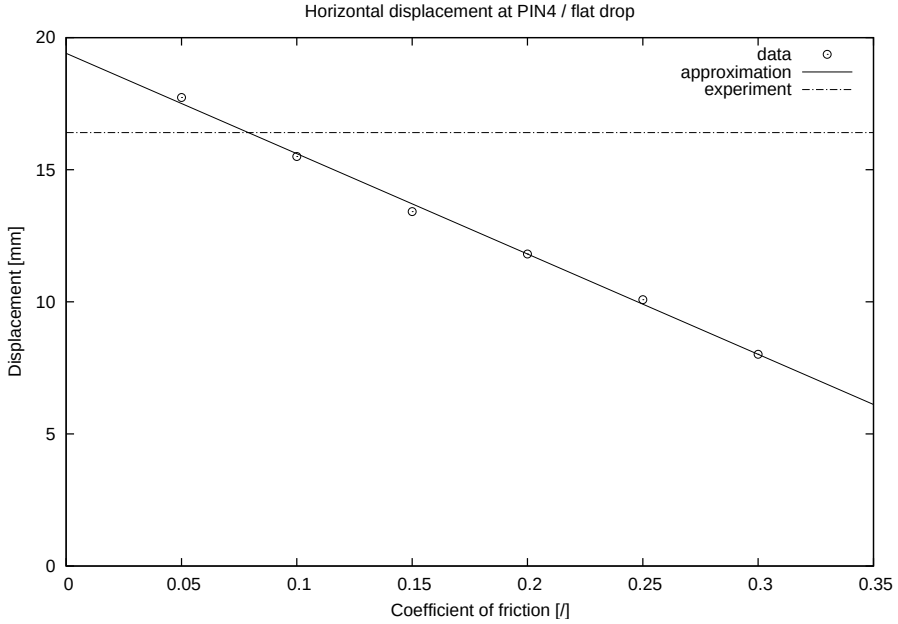

Figure 3.26: *Linear approximation of the horizontal displacement of PIN4 point as function of the coefficient of friction - flat drop case.*

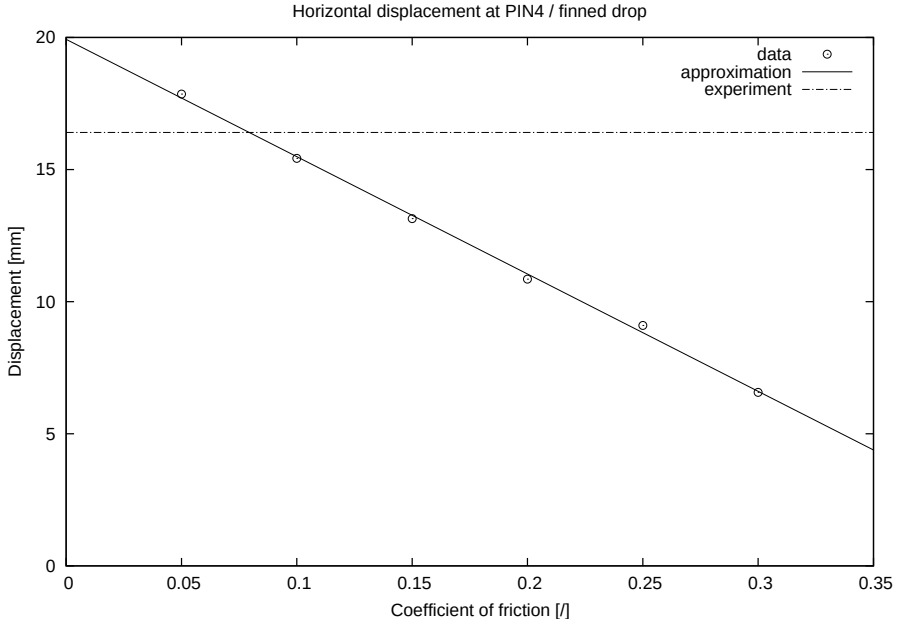

Figure 3.27: *Linear approximation of the horizontal displacement of PIN4 point as function of the coefficient of friction - finned drop case.*

3.5 Influence of the different tensile curves

Three different material data formulations of the cask and bar were compared. Base Model and Model *ctm* are done by resampling measured data which were sampled too densely for the ABAQUS material data regularization routines (see [1], Appendix D).

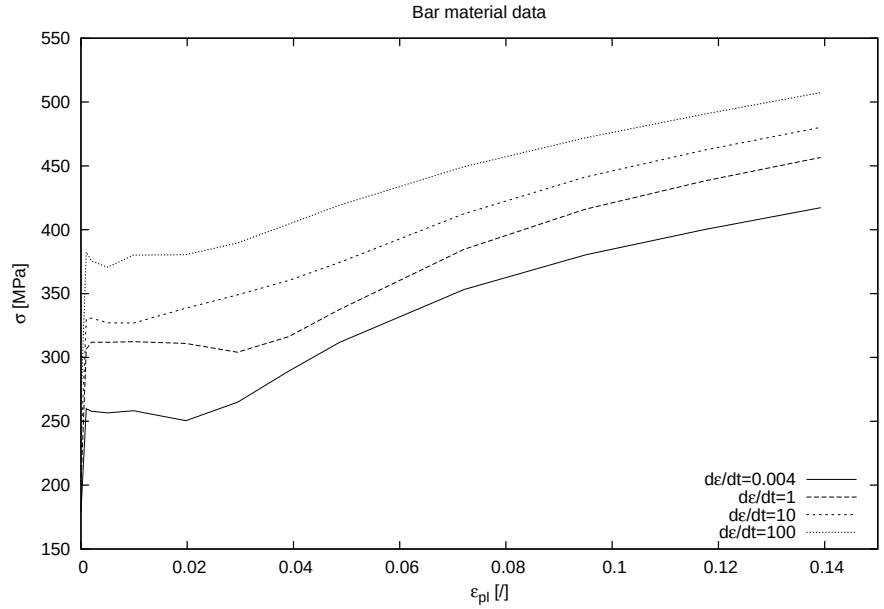

(a)

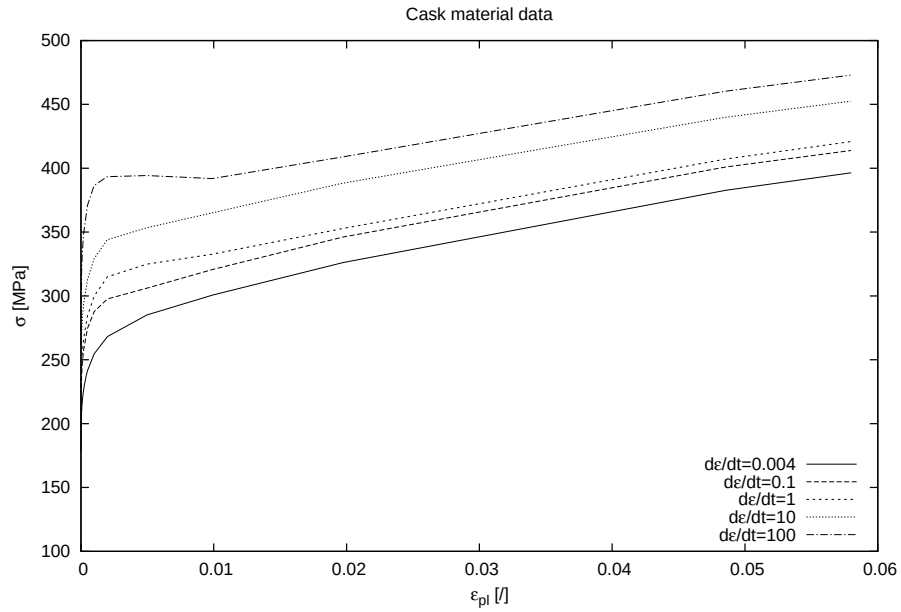

(b)

Figure 3.28: *Measured stress-strain curves for different strain rates: cask material (a) and bar material (b).*

Material data from the tensile test are presented in Appendix B and in Fig. 3.28. Fig. 3.29 and 3.30 depict magnified region $0\% \leq \varepsilon \leq 0.014\%$ for the material data used with Base Model and Model *ctm* respectively. This was done due to the ABAQUS regularization of the material data. All other data points ($\varepsilon > 0.014\%$) follow measurements exactly.

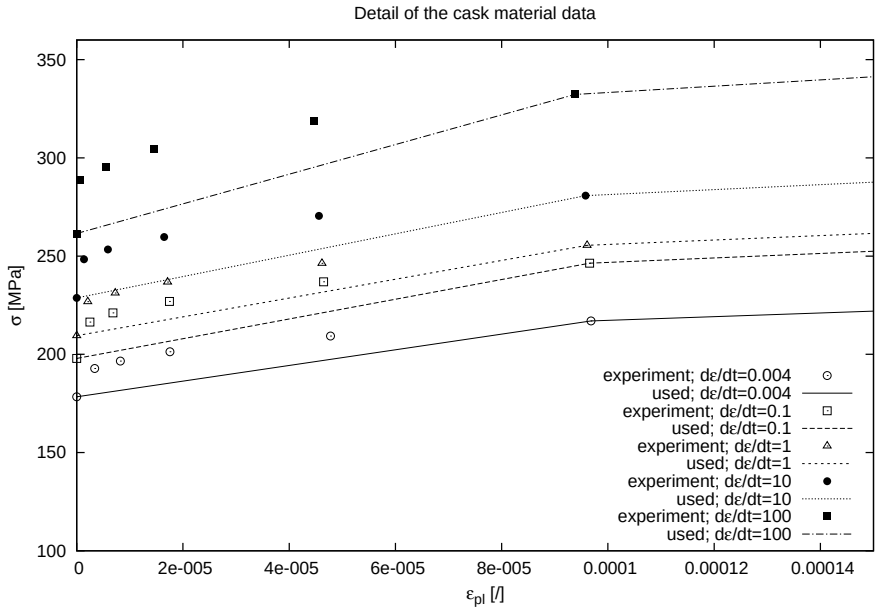

Figure 3.29: *Magnified region of the cask material data used in Base Model.*

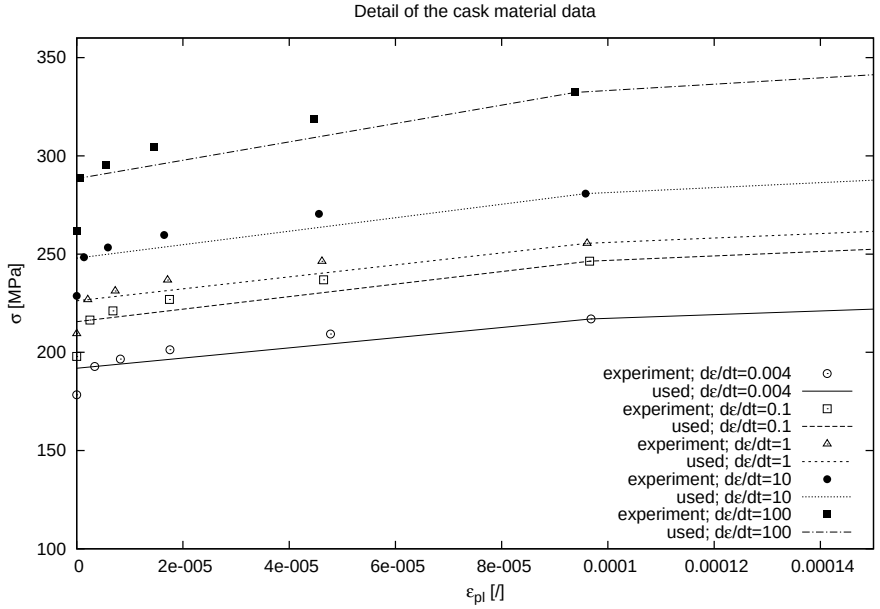

Figure 3.30: *Magnified region of the cask material data used in Model ctm.*

Johnson-Cook material model has been fitted to the tensile test data. The fit is presented in figure 3.31.

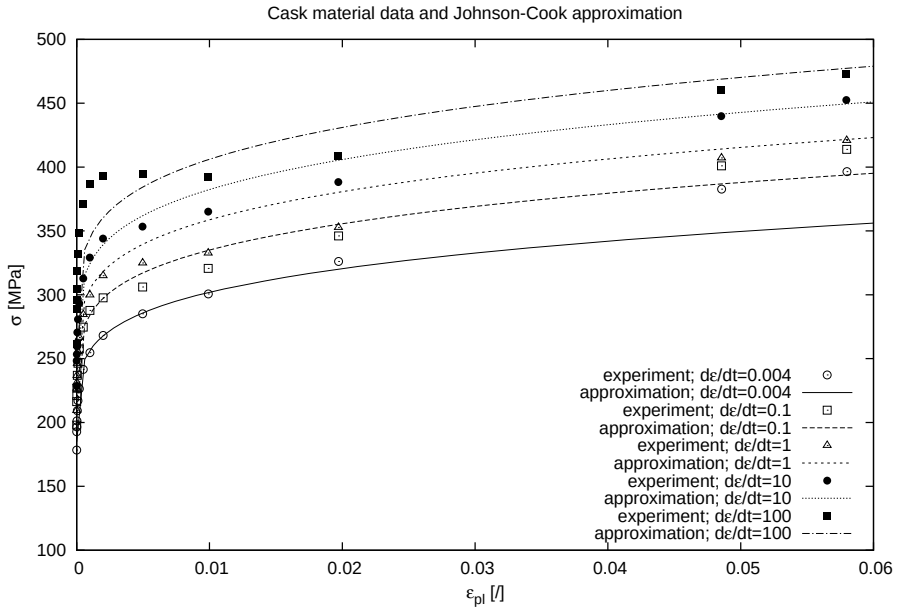

Figure 3.31: *Cask material data approximated by the Johnson-Cook model.*

The artificial, total, kinetic and strain energies are shown in Fig. 3.32, 3.33, 3.34 and 3.35 respectively for the three material models. A comparison of the reaction forces in the vertical directions is shown in Fig. 3.36 and the maximal principal strains at the D1 measurement point in Fig. 3.37. Vertical displacements at the points CSK1 and CSK3 are compared in Fig. 3.38 and 3.39 respectively. Vertical velocities at the points CSK1 and CSK3 are compared in Fig. 3.41 and 3.41. Horizontal displacements at the point PIN4 are compared in Fig. 3.42.

Base and *ctm* models give almost identical results. It is clear from Fig. 3.31 that Johnson-Cook material model itself differs significantly from experimental data. The model responses with the Johnson-Cook model clearly differ from two other models.

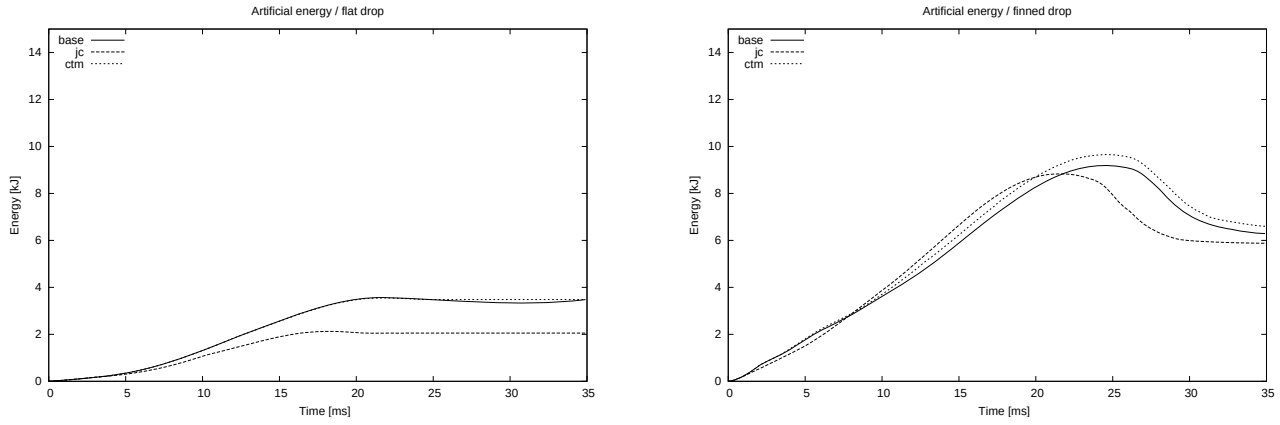

(a) *(b)*

Figure 3.32: *Computed artificial energy for different material models: flat (a) and finned target (b).*

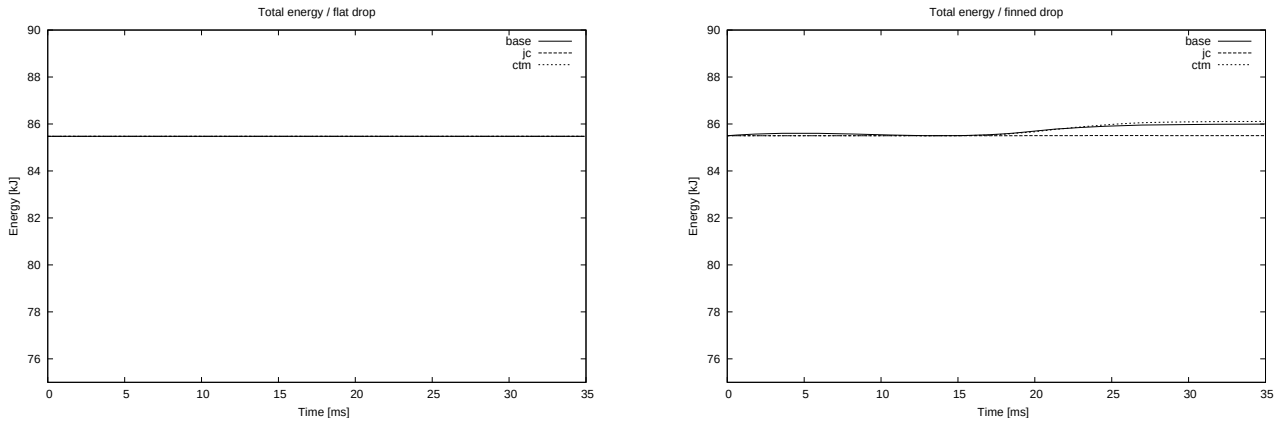

(a) *(b)*

Figure 3.33: *Computed total energy for different material models: flat (a) and finned target (b).*

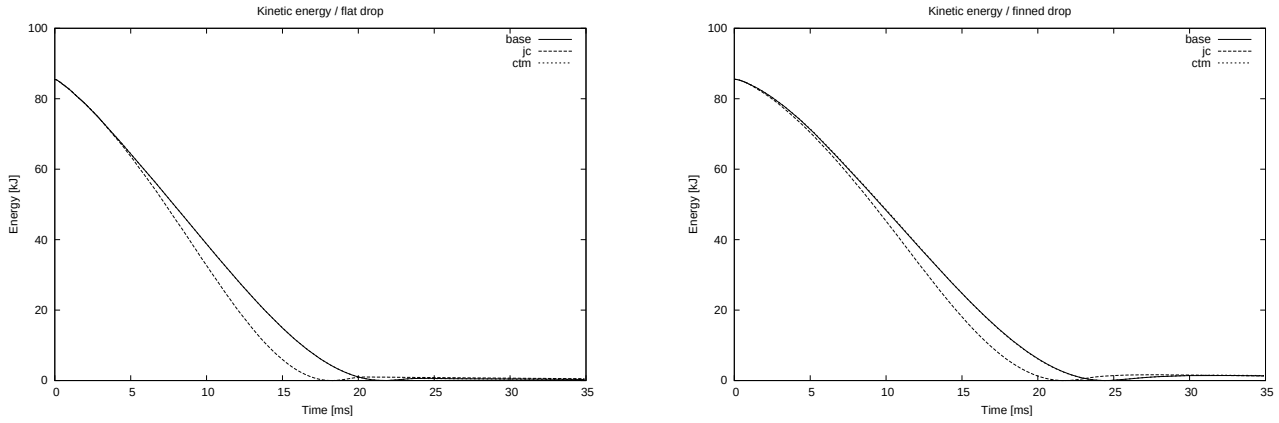

(a) *(b)*

Figure 3.34: *Computed kinetic energy for different material models: flat (a) and finned target (b).*

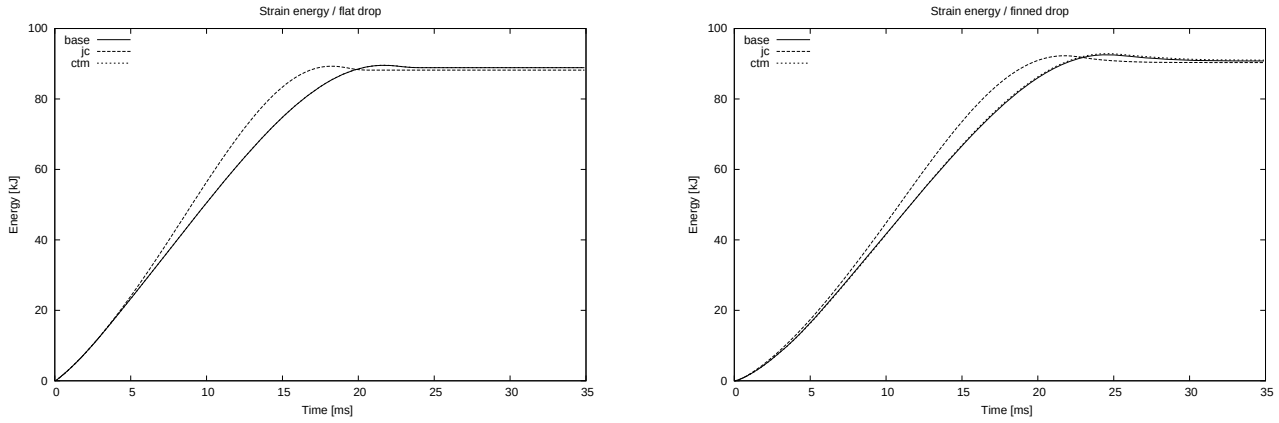

(a) *(b)*

Figure 3.35: *Computed strain energy for different material models: flat (a) and finned target (b).*

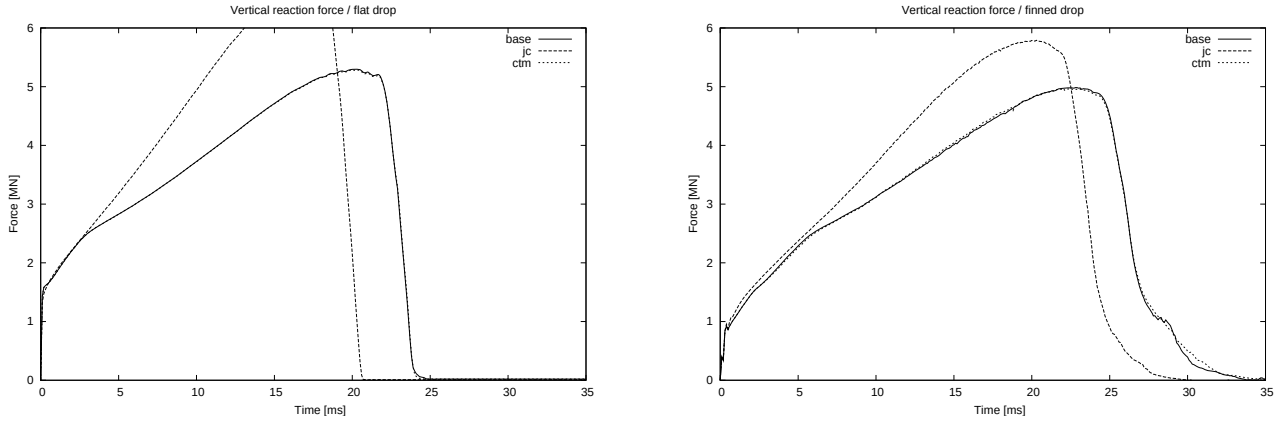

(a) *(b)*

Figure 3.36: *Computed vertical reaction forces for different material models: flat (a) and finned target (b).*

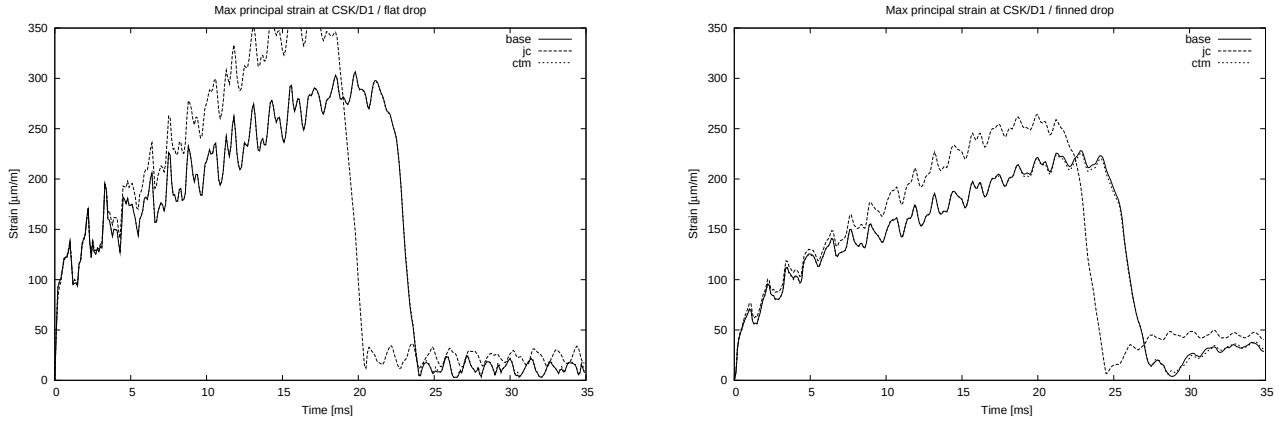

(a) *(b)*

Figure 3.37: *Computed maximal principal strains at the D1 for different material models: flat (a) and finned target (b).*

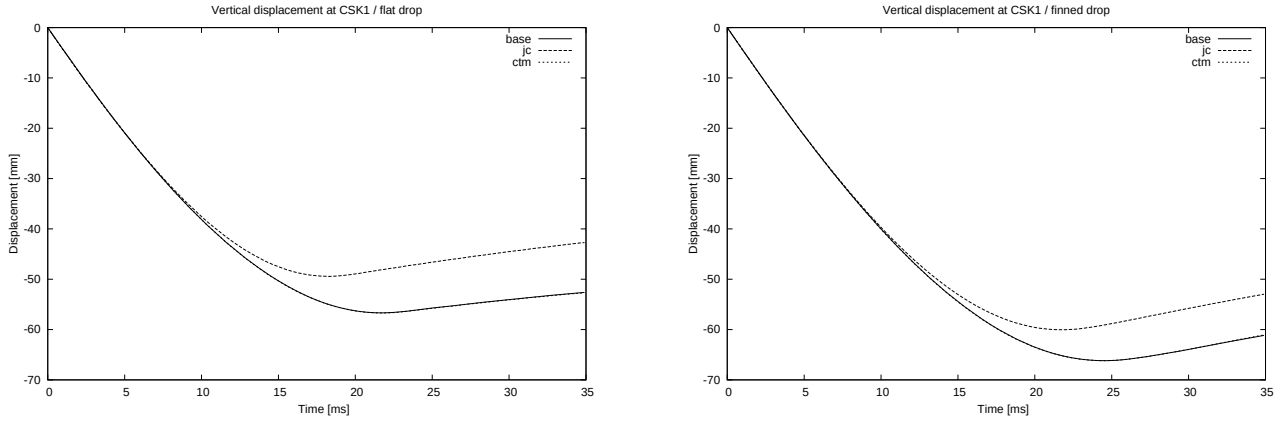

(a) *(b)*

Figure 3.38: *Computed vertical displacements at the CSK1 for different material models: flat (a) and finned target (b).*

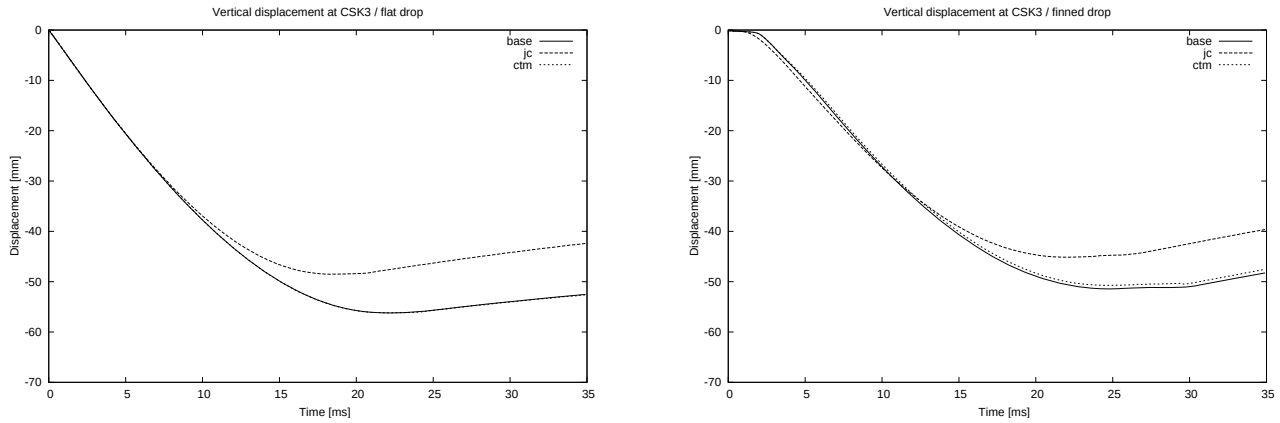

(a) *(b)*

Figure 3.39: *Computed vertical displacements at the CSK3 for different material models: flat (a) and finned target (b).*

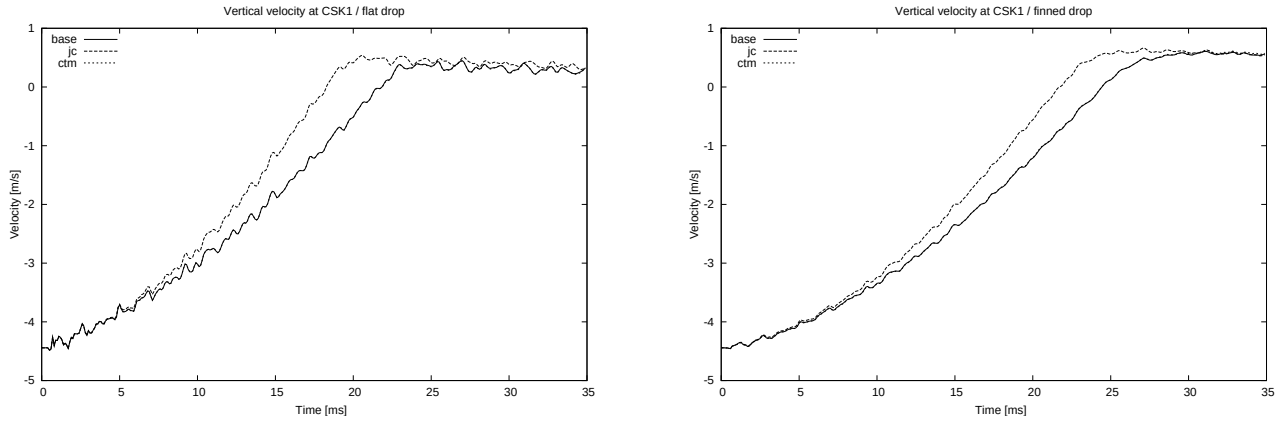

(a) *(b)*

Figure 3.40: *Computed vertical velocity at the CSK1 for different material models: flat (a) and finned target (b).*

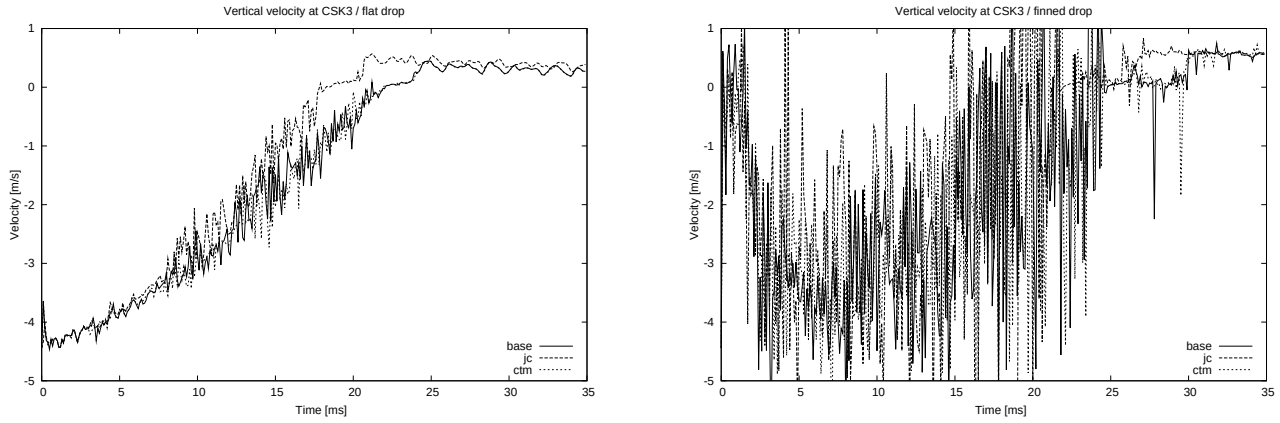

(a) *(b)*

Figure 3.41: *Computed vertical velocity at the CSK3 for different material models: flat (a) and finned target (b).*

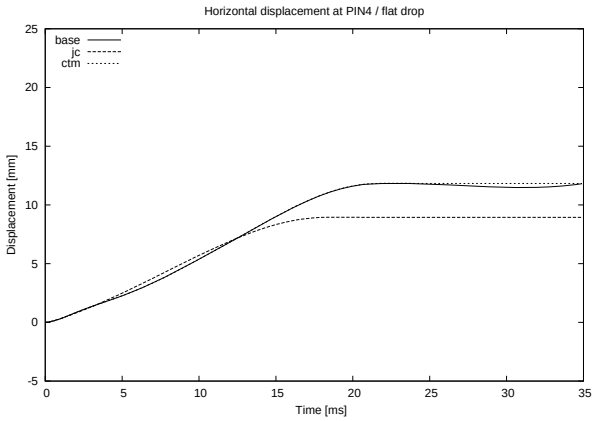

Figure 3.42: *Computed horizontal displacement at the PIN4 for different material models for the flat target.*

3.6 Influence of mass scaling factors

Mass scaling is used in order to speed-up the analysis. The scaling factor should be chosen in a way so that the system response is not significantly affected. Different integration time steps Δt, equivalent scaling factor and computational times are compiled in Tab. 3.4. The smaller integration time steps for the flat drop case is due to complex meshing of the cask part 6d.

Table 3.4: *Models and associated mass scaling parameters.*

Model name	Drop type	Time step (min) Δt [ns]	Equivalent scaling factor	CPU time [HH:MM:SS]
base	flat	11.4	1	08:13:52
	fins	19.6	1	03:59:24
f02	flat	22.8	2	04:31:03
	fins	39.2	2	02:37:43
f04	flat	45.6	4	02:01:49
	fins	78.4	4	01:10:48
f08	flat	91.2	8	01:00:34
	fins	156.8	8	00:37:58
f16	flat	182.4	16	00:35:09
	fins	313.6	16	00:19:53

Plots of the artificial, total, kinetic and strain are presented in Fig. 3.43, 3.44, 3.45 and 3.46 respectively for five scale factors. A comparison of the reaction forces in the vertical directions is shown in Fig. 3.47 and the maximal principal strains at the D1 measurement point in Fig. 3.48. Vertical displacements at the points CSK1 and CSK3 are compared in Fig. 3.49 and 3.50 respectively. Vertical velocities at the points CSK1 and CSK3 are depicted in Fig. 3.52 and 3.52. Horizontal displacements at the point PIN4 are shown in Fig. 3.53.

The smallest elements are found in the bar and in the parts 6, which are then the elements scaled when using

factors 2 and 4 as seen in Fig. 3.45. Much more elements in different parts are affected when larger scaling factors are applied.

It is clear from the figures that mass scaling should be used carefully due to its influence on the responses. Mass scaling factor should not exceed value of 8. Mass scaling should be avoided or it should not exceed factor 4 if the information about reaction force or strains at the point D1 are required. It may be used in the case when only approximative responses are needed.

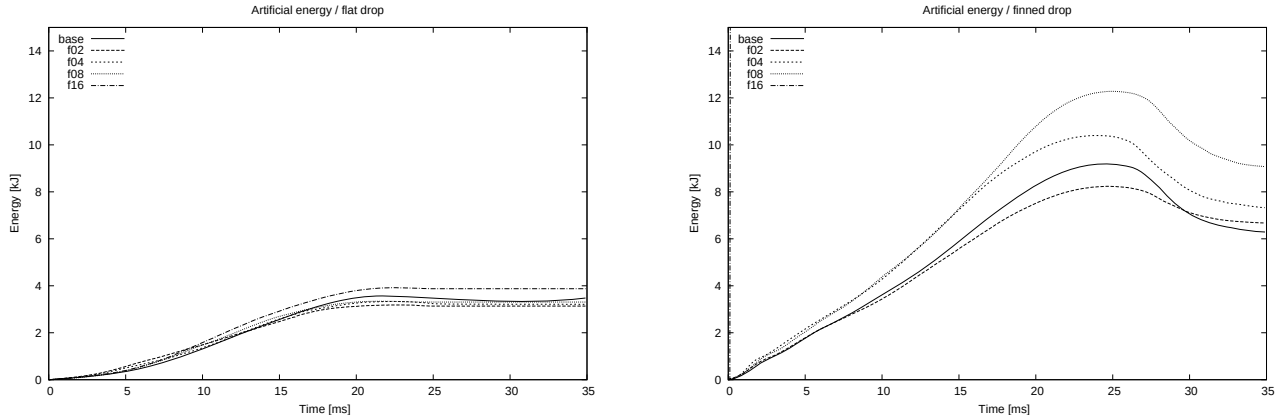

Figure 3.43: *Computed artificial energy for different mass scaling factors: flat (a) and finned target (b).*

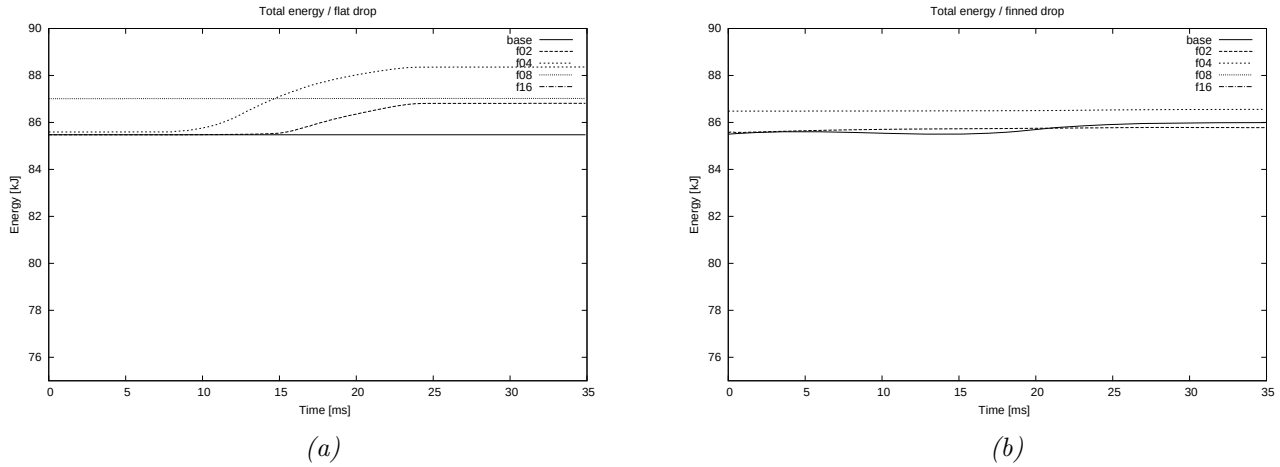

Figure 3.44: *Computed total energy for different mass scaling factors: flat (a) and finned target (b).*

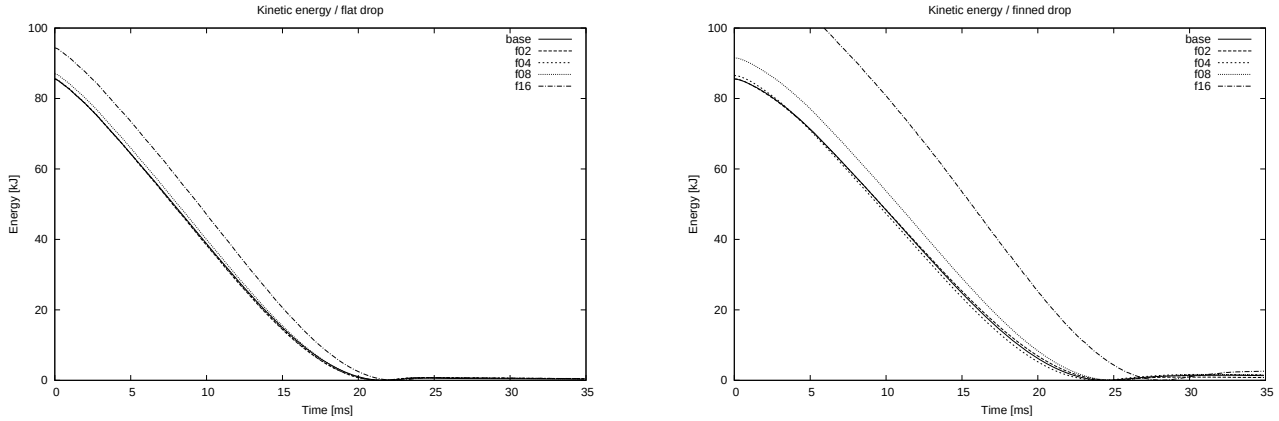

(a) *(b)*

Figure 3.45: *Computed kinetic energy for different mass scaling factors: flat (a) and finned target (b).*

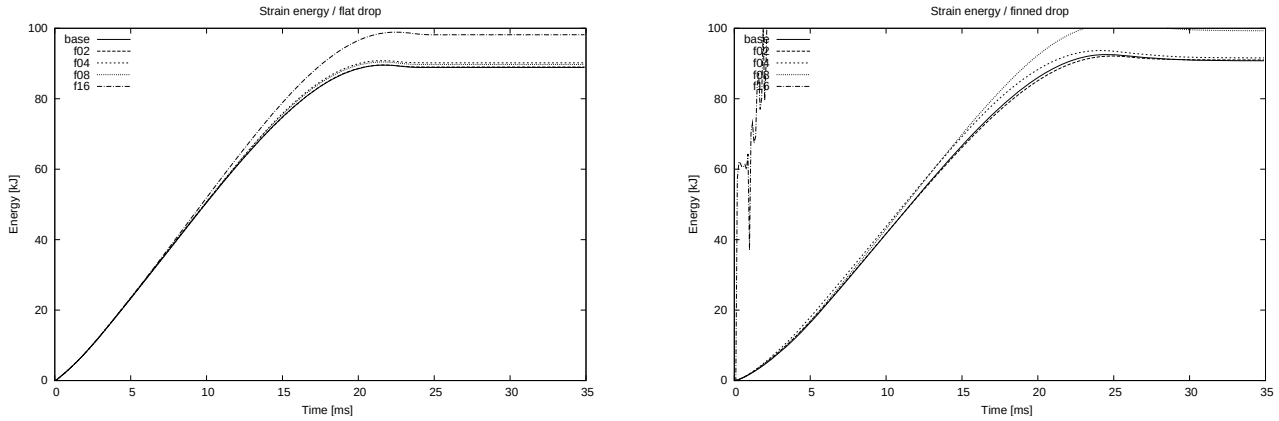

(a) *(b)*

Figure 3.46: *Computed strain energy for different mass scaling factors: flat (a) and finned target (b).*

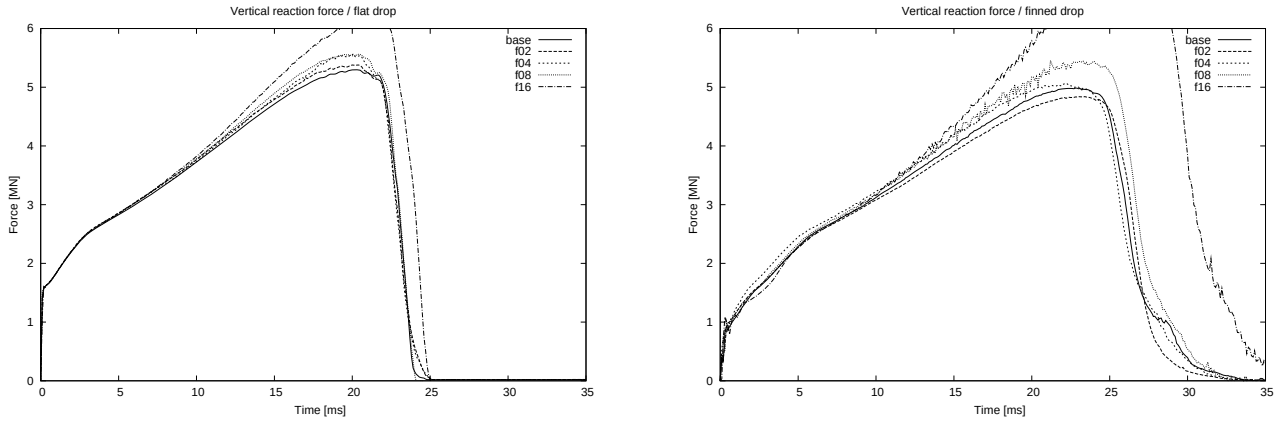

(a) *(b)*

Figure 3.47: *Computed vertical reaction forces for different mass scaling factors: flat (a) and finned target (b).*

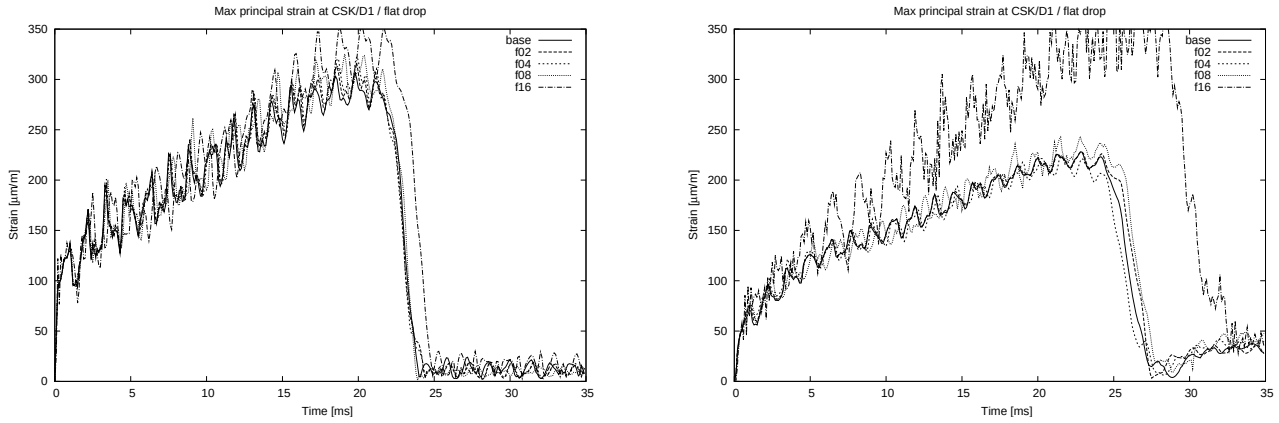

(a) *(b)*

Figure 3.48: *Computed maximal principal strains at the D1 for different mass scaling factors: flat (a) and finned target (b).*

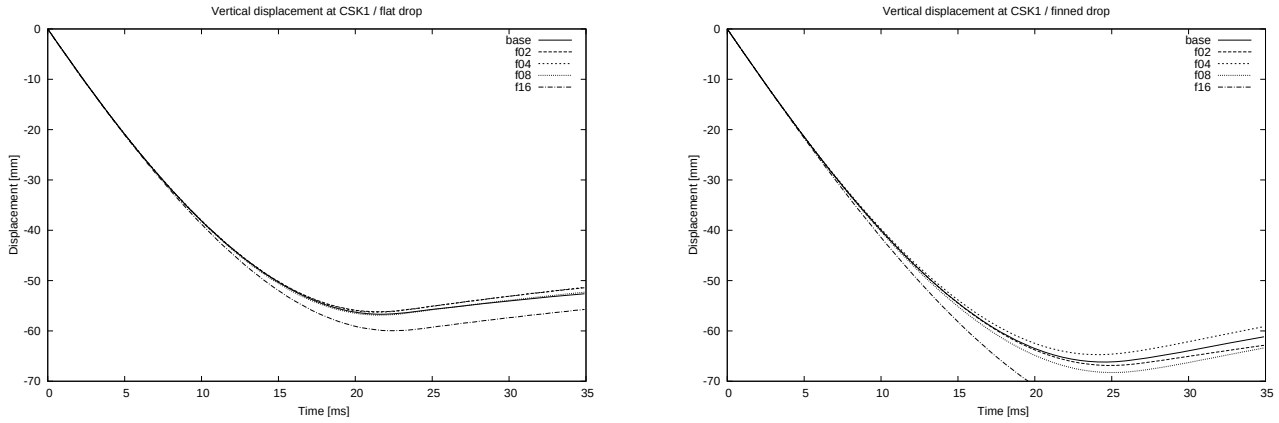

(a) *(b)*

Figure 3.49: *Computed vertical displacements at the CSK1 for different mass scaling factors: flat (a) and finned target (b).*

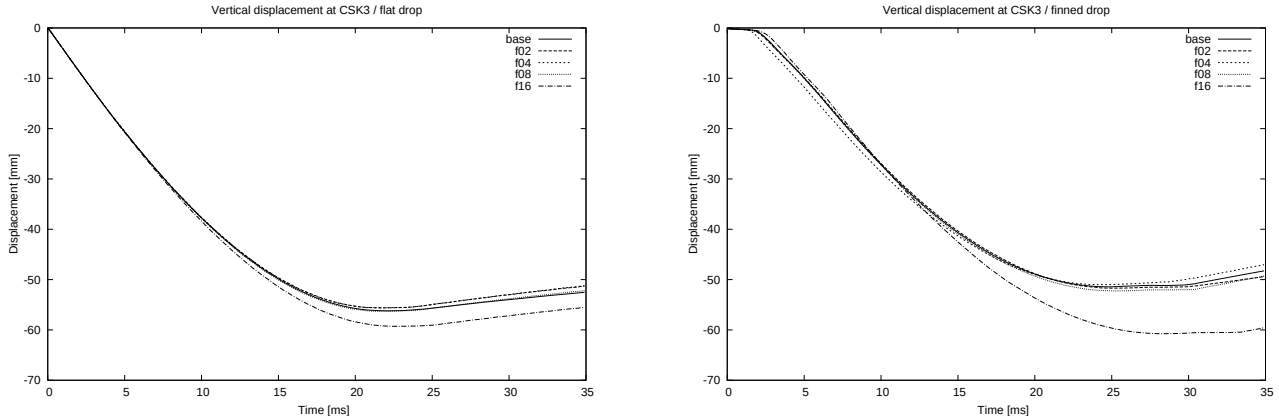

(a) *(b)*

Figure 3.50: *Computed vertical displacements at the CSK3 for different mass scaling factors: flat (a) and finned target (b).*

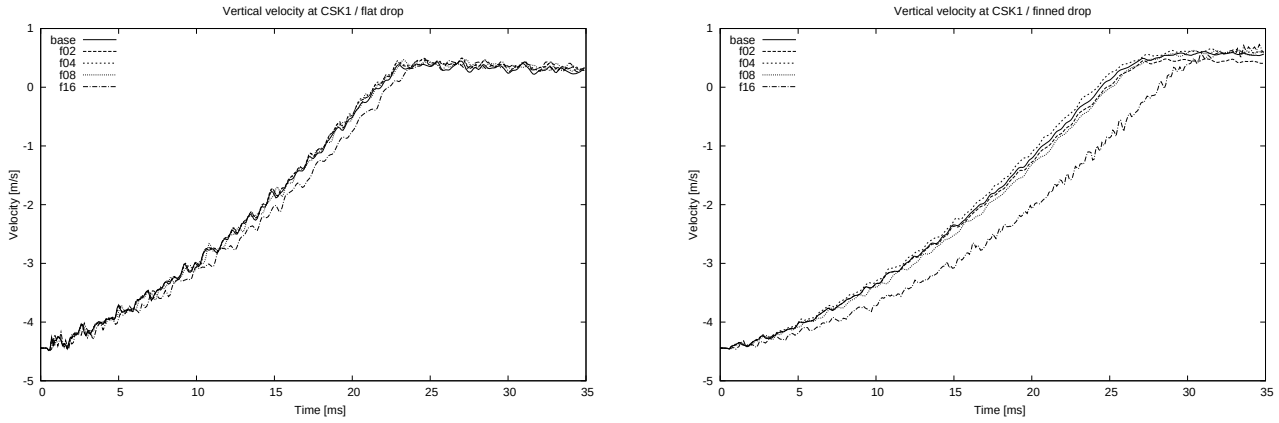

(a) *(b)*

Figure 3.51: *Computed vertical velocity at the CSK1 for different mass scaling factors: flat (a) and finned target (b).*

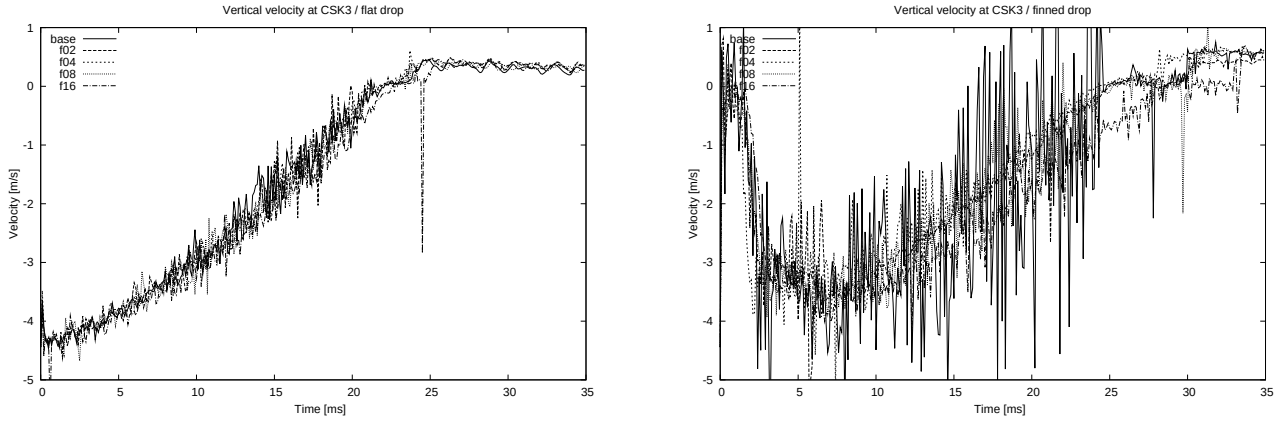

(a) *(b)*

Figure 3.52: *Computed vertical velocity at the CSK3 for different mass scaling factors: flat (a) and finned target (b).*

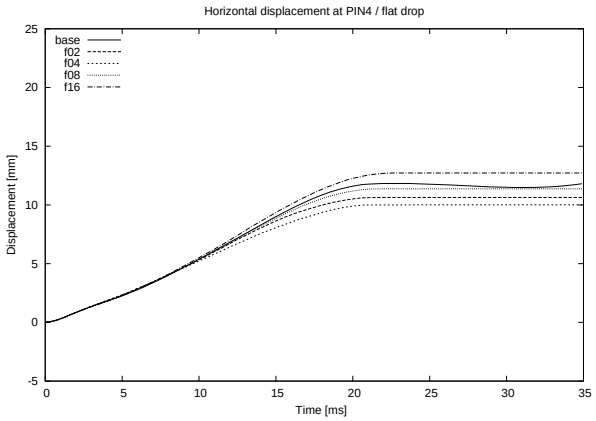

Figure 3.53: *Computed horizontal displacement at the PIN4 for different mass scaling factors for the flat target.*

3.7 Influence of mesh density

Several different mesh densities are considered, Tab. 3.5. Element sizes were varied predominantly in the vicinity of the impact area, Fig. 3.54 and 3.55. The element sizes in Tab. 3.5 are the "prescribed" values for the mesher in the impact region; actual element sizes may vary by a small amount. Different meshes are named and coded. The code of the mesh coincide with the element size of the cask 6a and bar part. The sizes of models in terms of the number of elements, nodes and degrees of freedom are shown in Tab. 3.6. The computational times of the analyses are indicated in Tab. 3.7.

Different model meshes are depicted in the Fig. 3.54 and 3.55. The subsequent figures present graphs of the same quantities as in preceding analyses. Four different energies of the complete model are considered again and compared for the models: artificial, total, kinetic and strain are presented in Fig. 3.56, 3.57, 3.58 and 3.59 respectively. A comparison of the reaction forces in the vertical directions is shown in Fig. 3.60 and the maximal principal strains at the D1 measurement point in Fig. 3.61. Vertical displacements at the points CSK1 and CSK3 are compared in Fig. 3.62 and 3.63 respectively. Vertical velocities at the points CSK1 and CSK3 are compared in Fig. 3.65 and 3.65. Horizontal displacements at the point PIN4 are compared in Fig. 3.66.

There are small differences in energies, which are integral measures of the models' behaviour, and reaction forces and maximal principal strains at the point D1. Larger differences can be seen in the finned drop case (minimum value is within 10% off the maximum one) than in the flat one. The differences in vertical displacement for the flat drop at points CSK1 and CSK3 are relatively small though they reach almost 5 mm which is around 10% of the maximal value. Larger differences (almost 20%) can be observed for the vertical displacements for the finned drop case. The relative differences in vertical displacement and velocity at the point CSK1 are comparable. Oscillations seen in vertical velocities are due to friction formulation in contact between the cask and bar. Finer meshes exhibit less oscillations, which is expected. The considerable scatter of horizontal displacements at bar's point PIN4 is comparable to differences due to coefficient of friction variations.

It is clear that the mesh density influences kinematical results such as vertical displacements and velocities as well as forces and strains. But, the most significant influence can be seen when studying horizontal displacement

Table 3.5: *Parameters of the mesh, degrees of freedom and computational times.*

Parameter	Unit	Mesh density: name and code								
		the coarsest	coarser	base	intermediate	fine	finer	x fine	xx fine	the finest
		200	**150**	**100**	**075**	**050**	**035**	**030a**	**030b**	**020**
_cskElementSize_1	mm	50	50	50	50	50	50	50	50	50
_cskElementSize_2	mm	50	50	50	50	50	50	50	50	50
_cskElementSize_3	mm	50	50	50	50	50	50	50	50	50
_cskElementSize_4	mm	50	50	50	50	50	50	50	50	50
_cskElementSize_5	mm	20	20	20	20	15	15	15	15	15
_cskElementSize_6a	mm	**20**	**15**	**10**	**7.5**	**5**	**3.5**	**3**	**3**	**2**
_cskElementSize_6b	mm	20	15	15	15	10	10	10	5	5
_cskElementSize_6c	mm	20	15	15	15	10	10	10	5	5
_cskElementSize_6d	mm	20	20	20	20	15	15	15	15	15
_pinElementSize	mm	**20**	**15**	**10**	**7.5**	**5**	**3.5**	**3**	**3**	**2**
_lidElementSize	mm	50	50	50	50	50	50	50	50	50

Table 3.6: *Model size.*

Mesh density	Code	Drop type	Number of elements	Number of nodes	Number of degrees of freedom
the coarsest	200	flat	19 451	20 818	62 457
		fins	18 359	21 431	64 296
coarser	150	flat	19 612	21 052	63 159
		fins	18 538	21 735	65 208
base	100	flat	20 058	21 609	64 830
		fins	19 042	22 427	67 284
intermediate	075	flat	20 976	22 716	68 151
		fins	20 258	23 957	71 874
fine	050	flat	28 561	29 622	88 869
		fins	27 484	31 932	95 799
finer	035	flat	40 039	42 046	126 141
		fins	41 093	47 063	141 192
x fine	030a	flat	43 072	45 472	136 419
		fins	/	/	/
xx fine	030b	flat	44 134	46 886	140 661
		fins	/	/	/
the finest	020	flat	110 243	116 054	348 165
		fins	125 388	137 501	412 506

at points PIN3 and PIN4 on the bar. It is also clear from Fig. 3.67 that convergence of the horizontal displacement is not monotonous and that the coefficient of friction is overestimated in this case since all displacement values are underestimated. More variations are found at the point PIN4 than in the point PIN3 due to the fact that the point PIN4 lies on the bottom bar surface where the frictional contact plays an important role.

Table 3.7: *Model analysis's computational times.*

Mesh density	Code	Drop type	CPU time [DD-HH:MM]	CPUs
the coarsest	200	flat	00-06:21	2
		fins	00-04:30	2
coarser	150	flat	00-04:07	2
		fins	00-02:11	2
base	100	flat	00-04:44	2
		fins	00-02:23	2
intermediate	07.5	flat	00-04:27	2
		fins	00-04:08	2
fine	050	flat	00-12:45	2
		fins	00-14:03	2
finer	035	flat	01-11:00	2
		fins	01-18:08	2
x fine	030a	flat	01-17:48	2
		fins	/	2
xx fine	030b	flat	01-18:32	2
		fins	/	2
the finest	020	flat	12-13:47	2
		fins	14-07:37	2

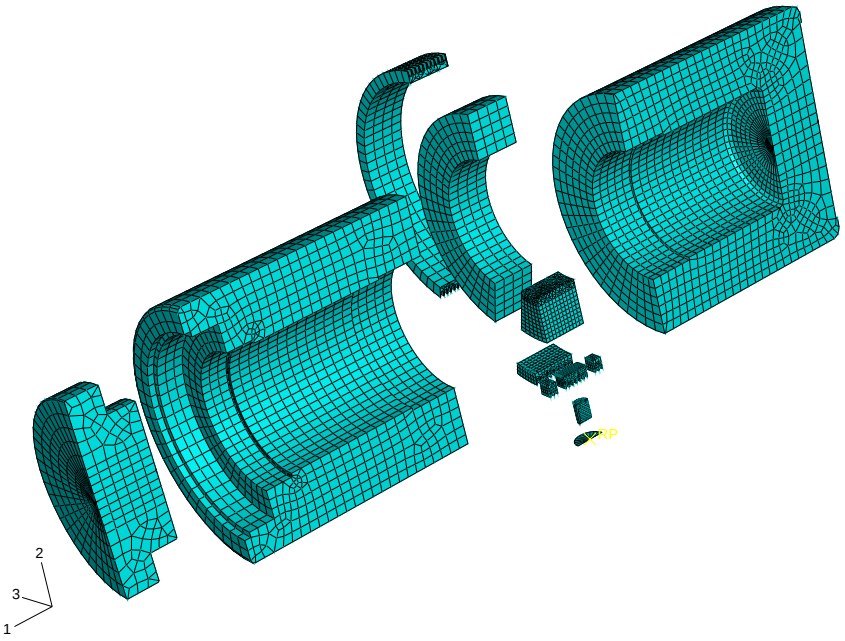

a

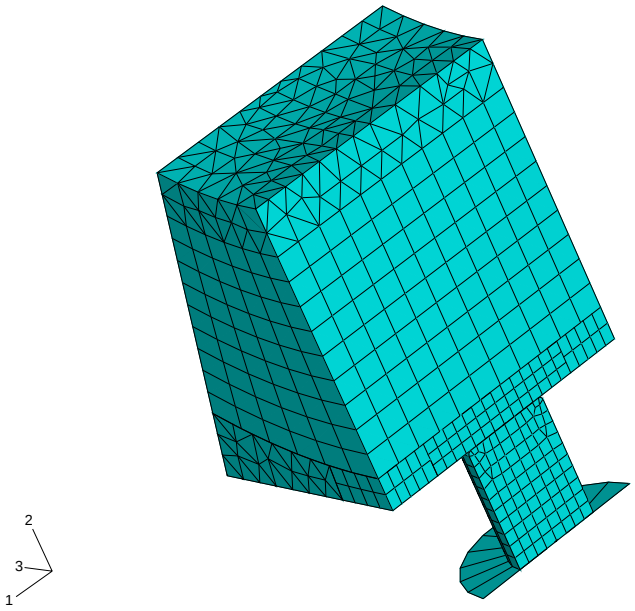

b

Figure 3.54: *Base model mesh: whole model (a) and detail (b).*

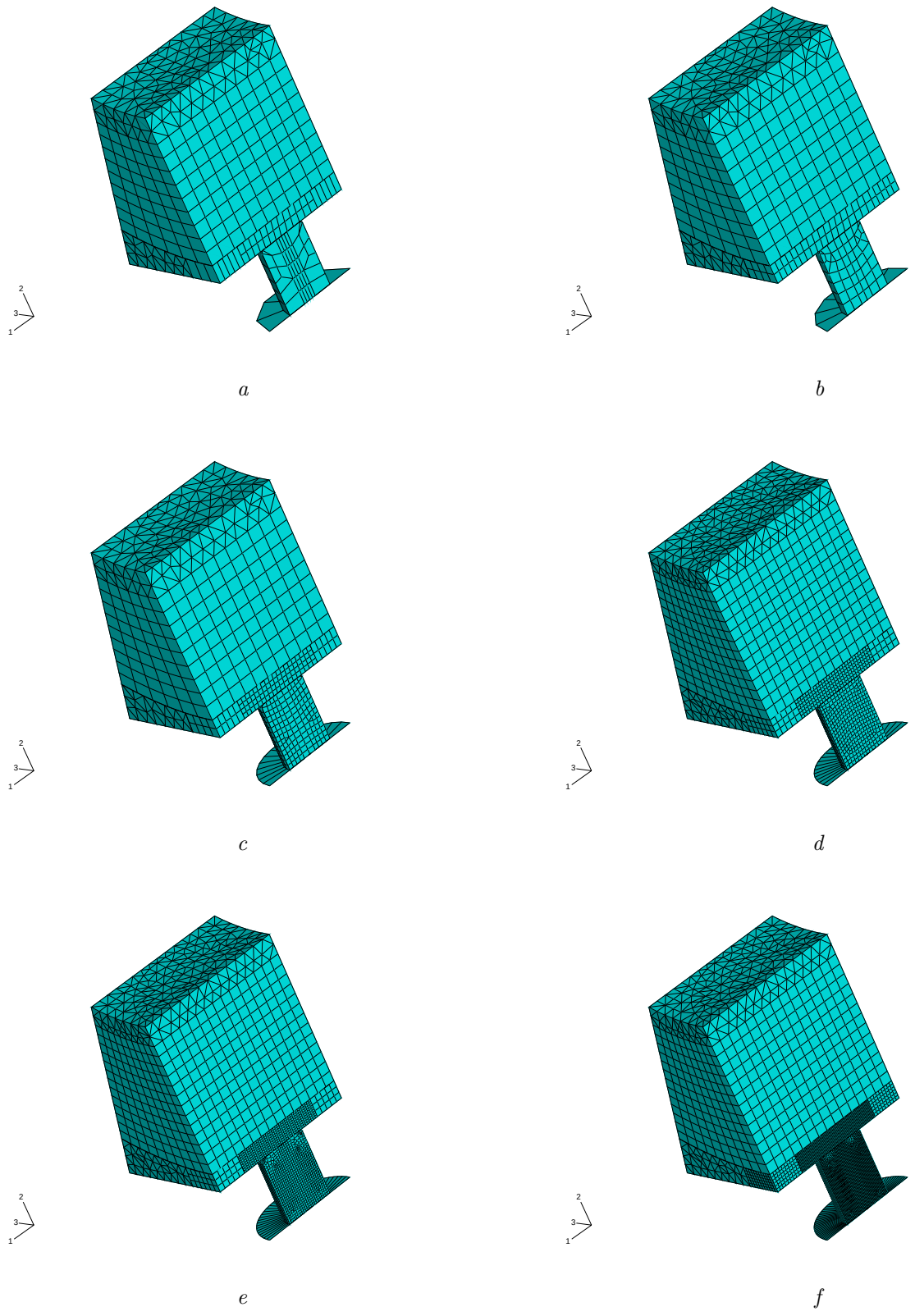

Figure 3.55: *Detail of the mesh: the coarsest (a), coarser (b), intermediate (c), fine (d), finer (e) and the finest (f) mesh.*

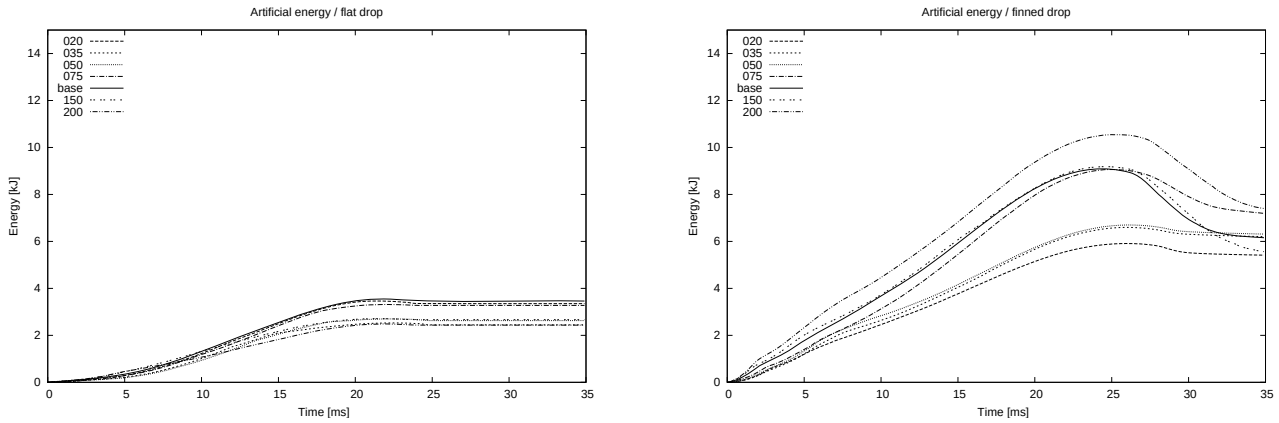

a *b*

Figure 3.56: *Computed artificial energy for different mesh densities: flat (a) and finned target (b).*

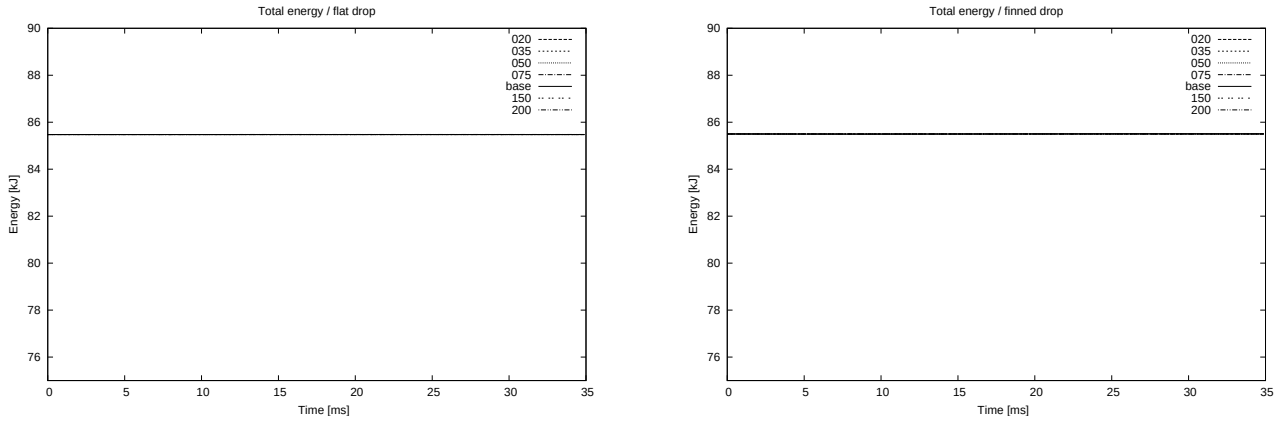

a *b*

Figure 3.57: *Computed total energy for different mesh densities: flat (a) and finned target (b).*

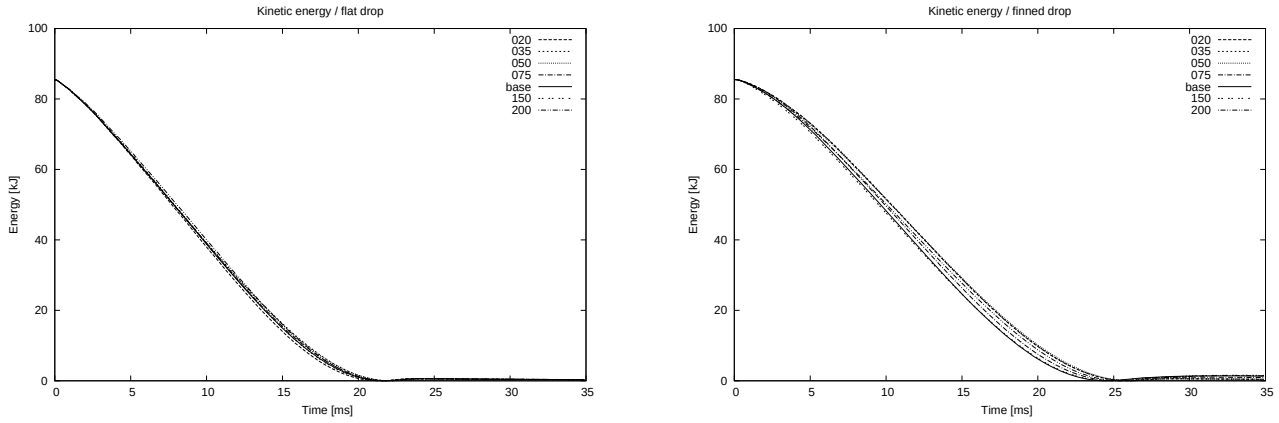

a *b*

Figure 3.58: *Computed kinetic energy for different mesh densities: flat (a) and finned target (b).*

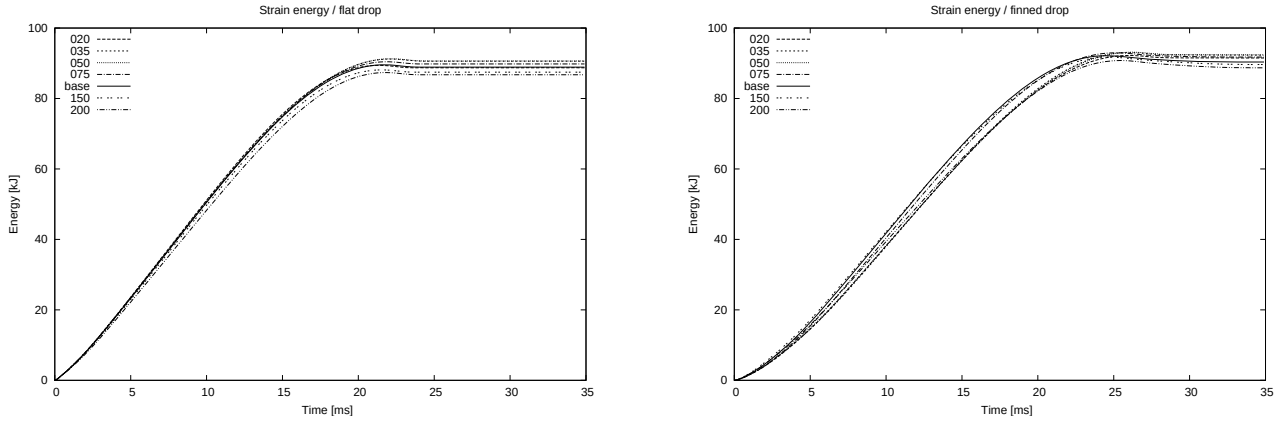

a *b*

Figure 3.59: *Computed strain energy for different mesh densities: flat (a) and finned target (b).*

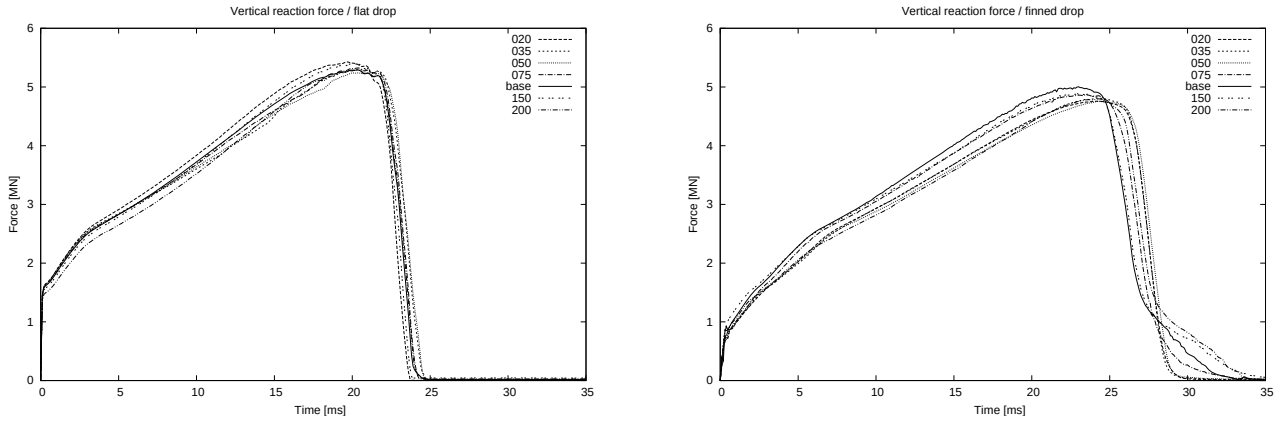

a *b*

Figure 3.60: *Computed vertical reaction forces for different mesh densities: flat (a) and finned target (b).*

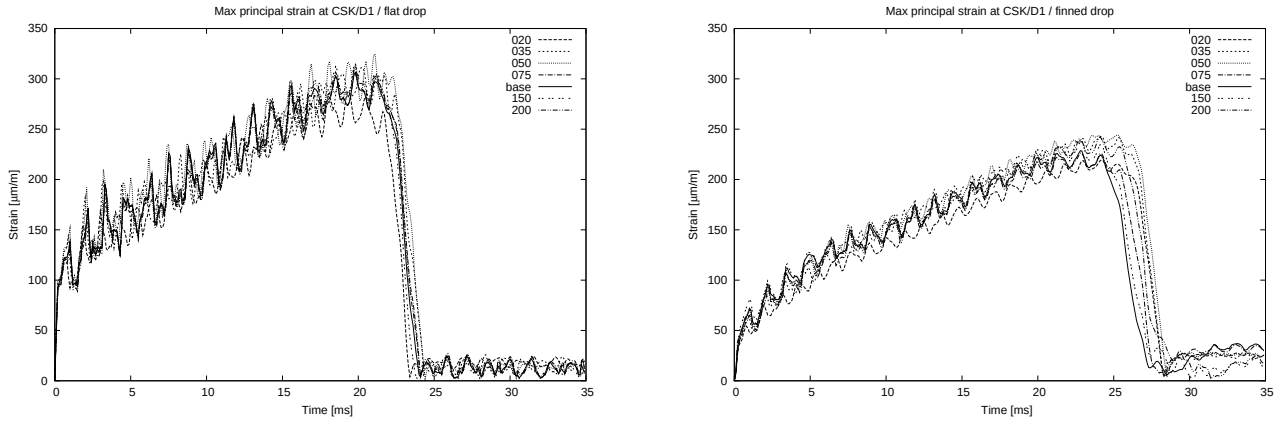

a *b*

Figure 3.61: *Computed maximal principal strains at the D1 for different mesh densities: flat (a) and finned target (b).*

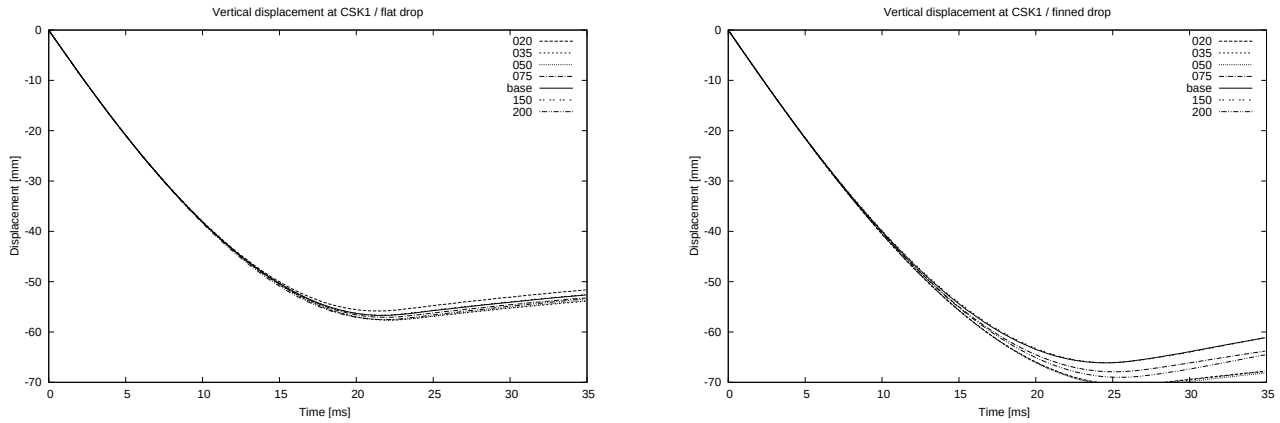

a *b*

Figure 3.62: *Computed vertical displacements at the CSK1 for different mesh densities: flat (a) and finned target (b).*

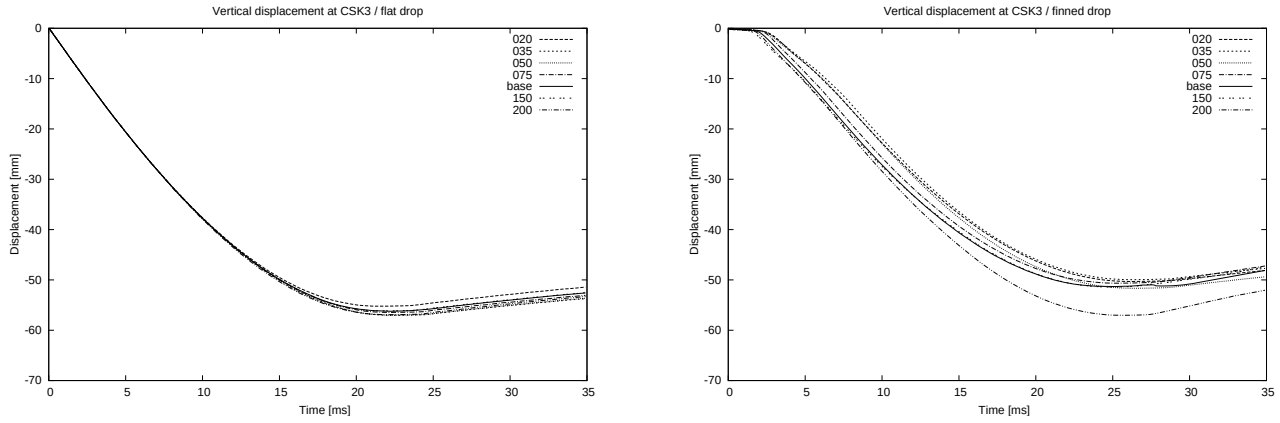

a *b*

Figure 3.63: *Computed vertical displacements at the CSK3 for different mesh densities: flat (a) and finned target (b).*

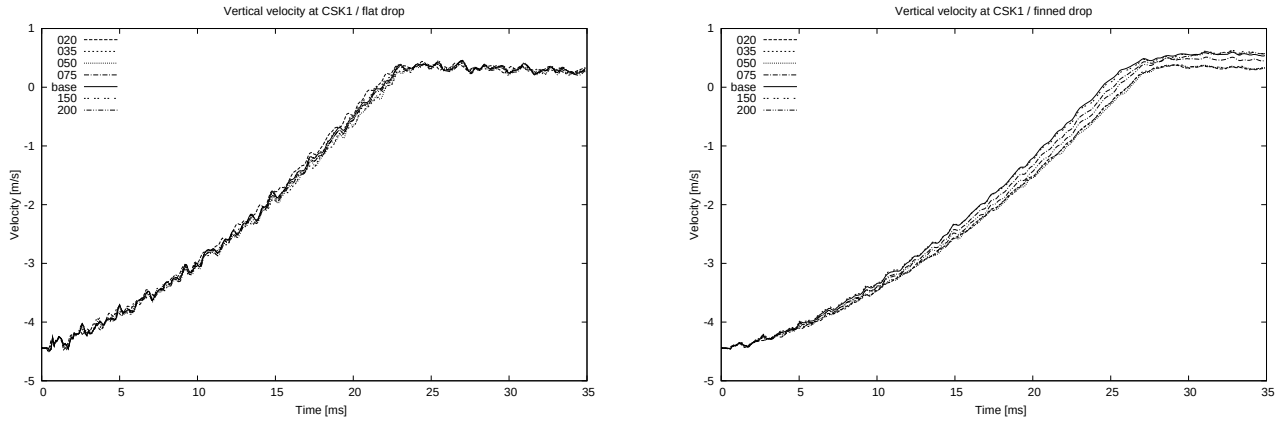

a *b*

Figure 3.64: *Computed vertical velocity at the CSK1 for different mesh densities: flat (a) and finned target (b).*

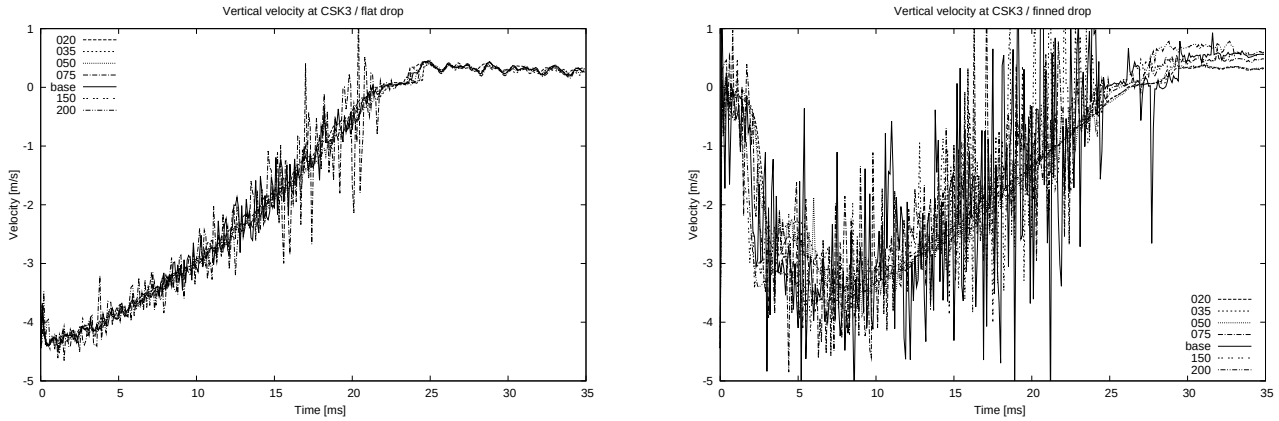

a *b*

Figure 3.65: *Computed vertical velocity at the CSK3 for different mesh densities: flat (a) and finned target (b).*

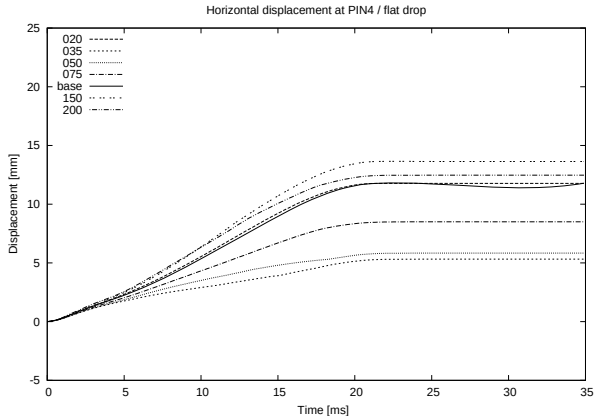

Figure 3.66: *Computed horizontal displacement at the PIN4 for different mesh densities for the flat target.*

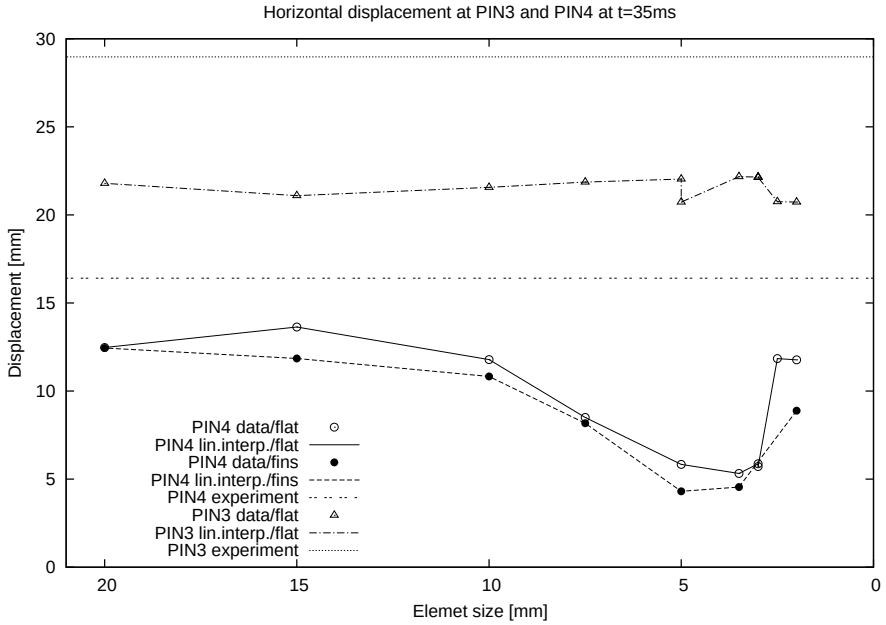

Figure 3.67: *Convergence of the horizontal displacement at PIN3 and PIN4 points on the bar with the mesh density.*

3.8 Influence of tie constraints

Parts of the cask are connected by the tie command. Tie constraints “tie” two separate surfaces with different meshes together so that there is no relative motion between them. The nodes on the slave surface are constrained to have the same value of displacement, temperature, pore pressure, or electrical potential as the point on the master surface to which they are tied. The surface with the finer mesh is selected to be the slave surface. This all interrupts continuity of interpolations over tie constraint borders. Hence, the tie constraints should be used in the places where gradients of quantities under consideration are arbitrary small.

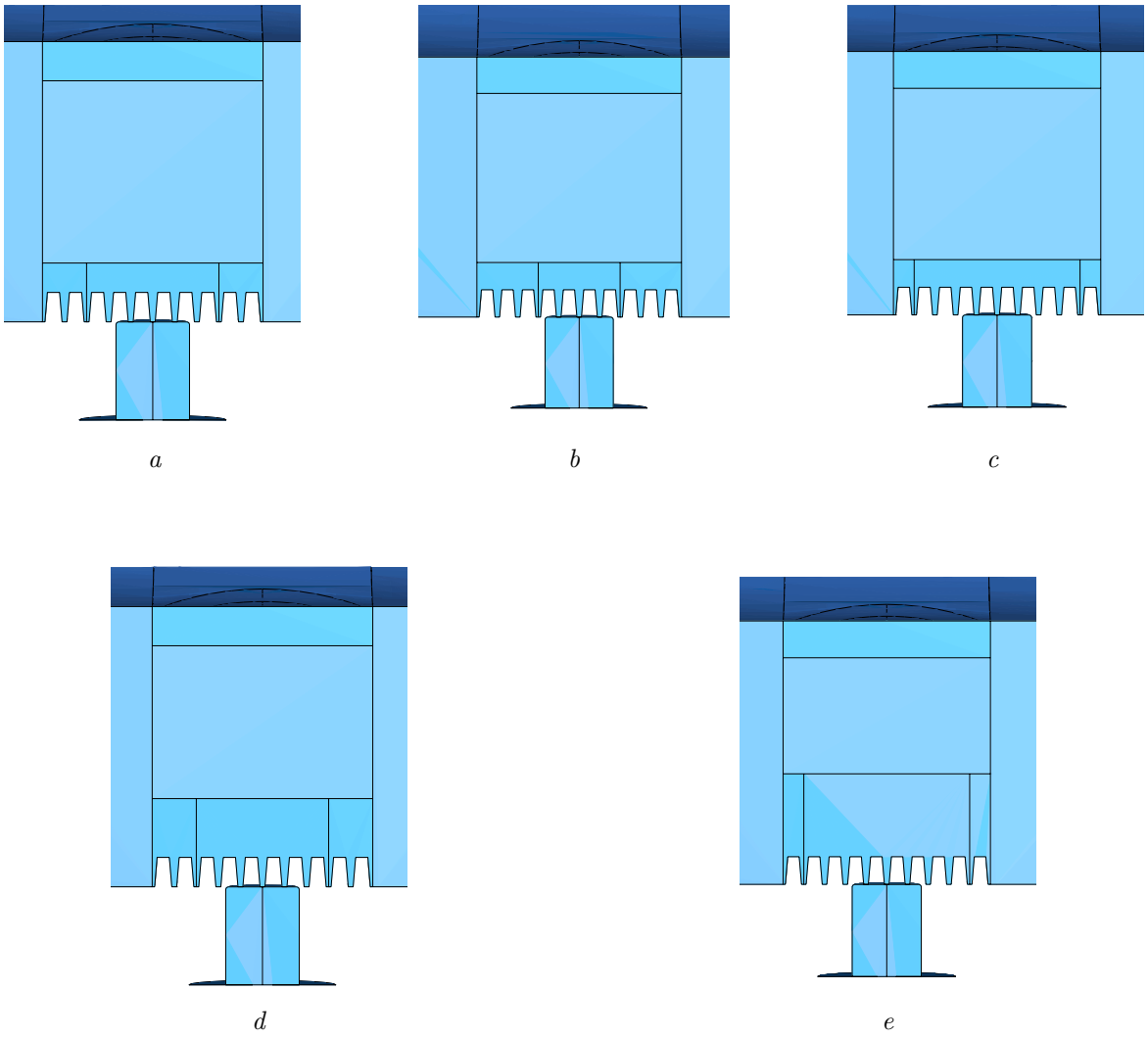

Figure 3.68: *Impact area detail of different models: Base Model (a), m1 model (b), p1 model (c), d1 model (d) and d2 model (e)*

Four new geometry sets or models are introduced to study the influence of the tie constraints near the impact area. Model *m1* decreases length of the 6a cask part by one fin on the both sides bringing tied surfaces very near to the impact cone (see Fig. 3.68*b*). On the contrary Model *p1* increases length of the 6a cask part for the same amount (see Fig. 3.68*c*). Model *d1* doubles the thickness of the full part of the 6a cask part in comparison to the Base model (see Fig. 3.68*d*) whereas model *d2* triples the thickness of the full part of the 6a cask part and also increases its length by one fin on the both sides in comparison to the Base model (see Fig. 3.68*e*).

The artificial, total, kinetic and strain energies are presented in Fig. 3.69, 3.70, 3.71 and 3.72 respectively. A comparison of the reaction forces in the vertical directions is shown in Fig. 3.73 and the maximal principal strains at the D1 measurement point in Fig. 3.74. Vertical displacements at the points CSK1 and CSK3 are compared in Fig. 3.75 and 3.76 respectively. Vertical velocities at the points CSK1 and CSK3 are compared in Fig. 3.78 and 3.78. Horizontal displacements at the point PIN4 are compared in Fig. 3.79.

There are no significant differences among different tie configurations models.

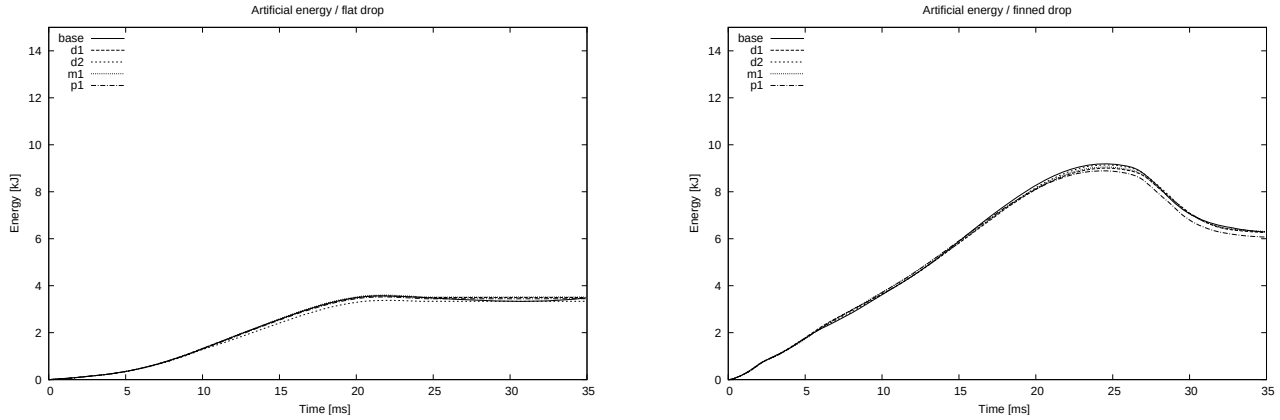

Figure 3.69: *Computed artificial energy for different tie model configurations: flat (a) and finned target (b).*

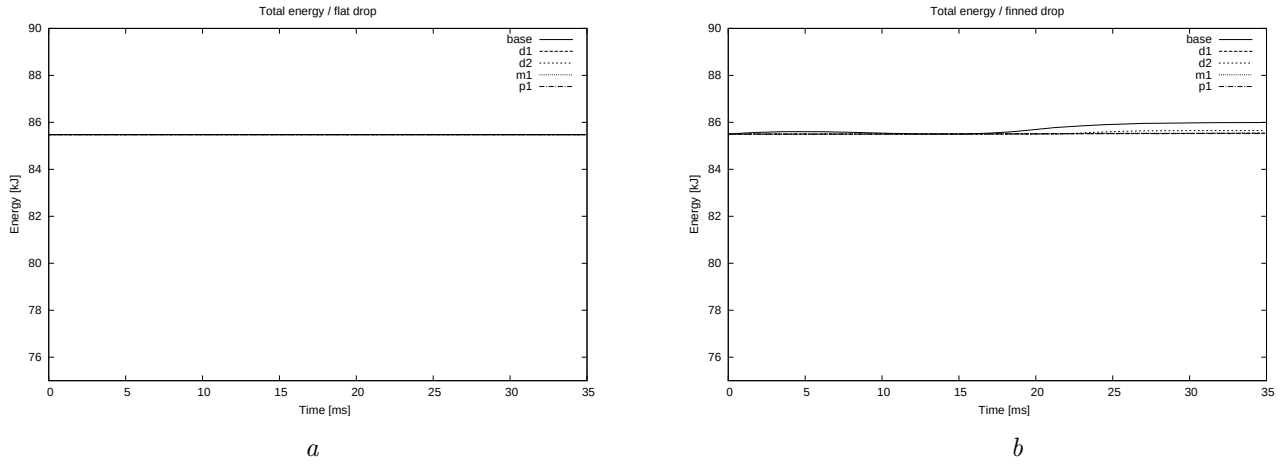

Figure 3.70: *Computed total energy for different tie model configurations: flat (a) and finned target (b).*

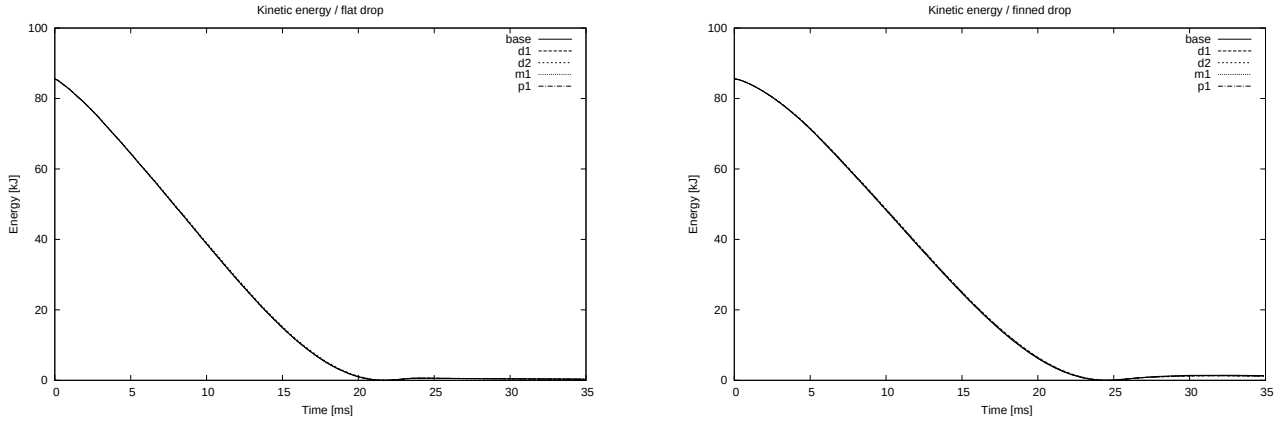

a *b*

Figure 3.71: *Computed kinetic energy for different tie model configurations: flat (a) and finned target (b).*

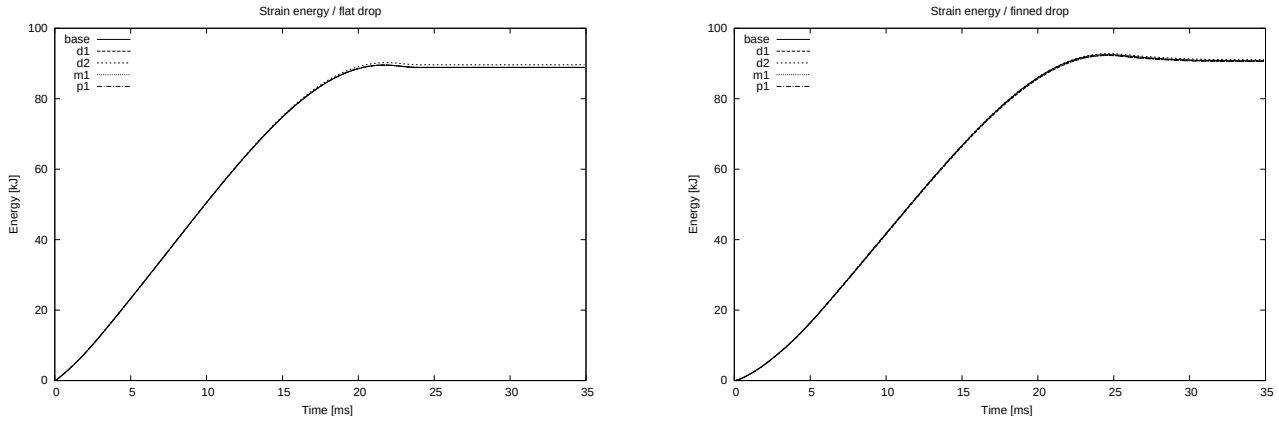

a *b*

Figure 3.72: *Computed strain energy for different tie model configurations: flat (a) and finned target (b).*

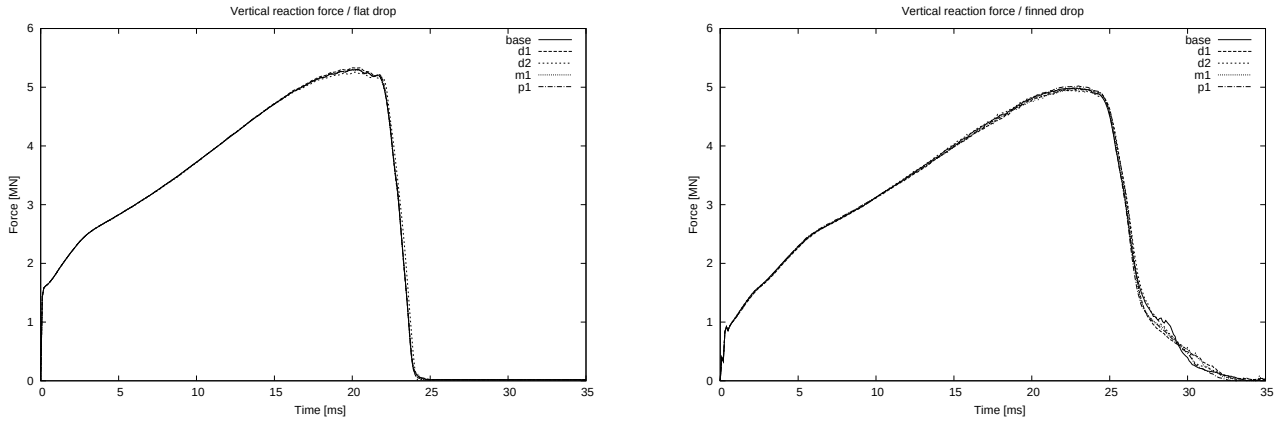

a *b*

Figure 3.73: *Computed vertical reaction forces for different tie model configurations: flat (a) and finned target (b).*

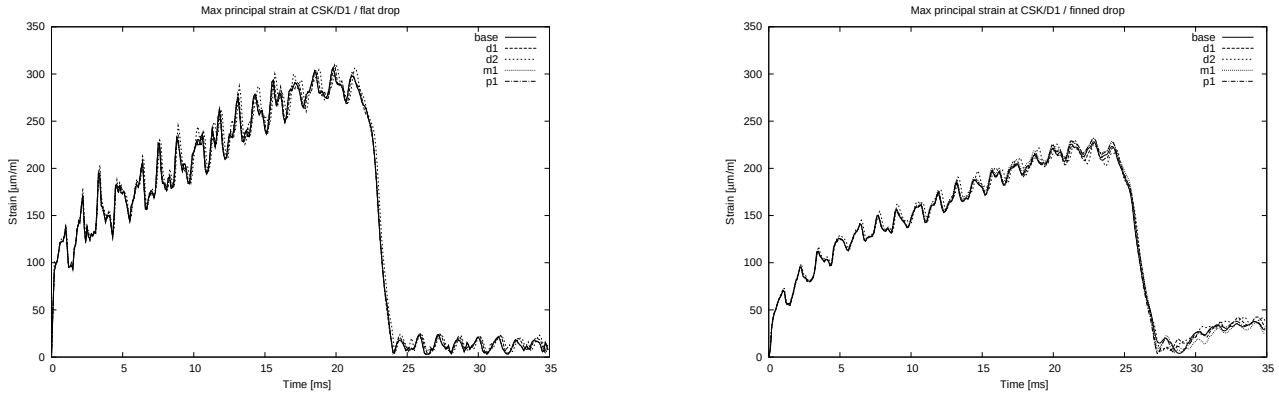

a *b*

Figure 3.74: *Computed maximal principal strains at the D1 for different tie model configurations: flat (a) and finned target (b).*

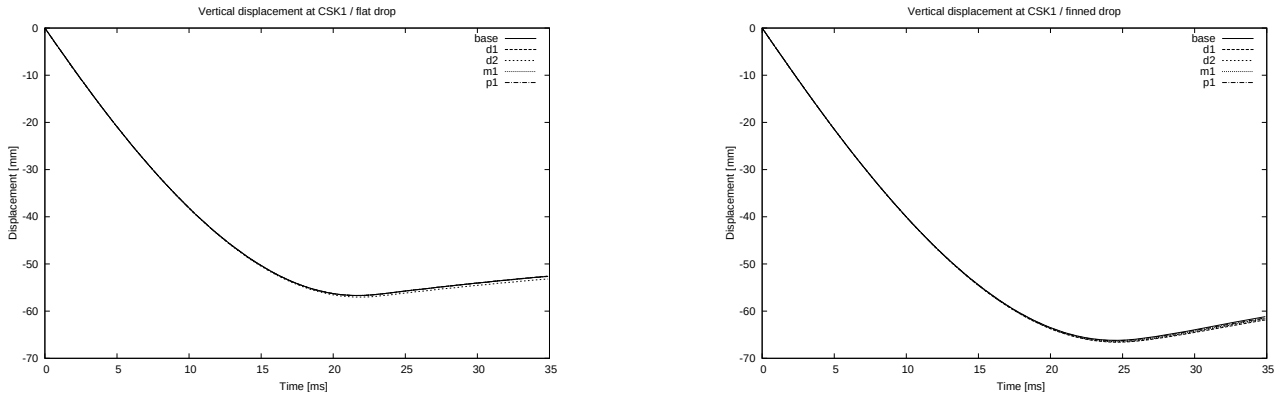

a *b*

Figure 3.75: *Computed vertical displacements at the CSK1 for different tie model configurations: flat (a) and finned target (b).*

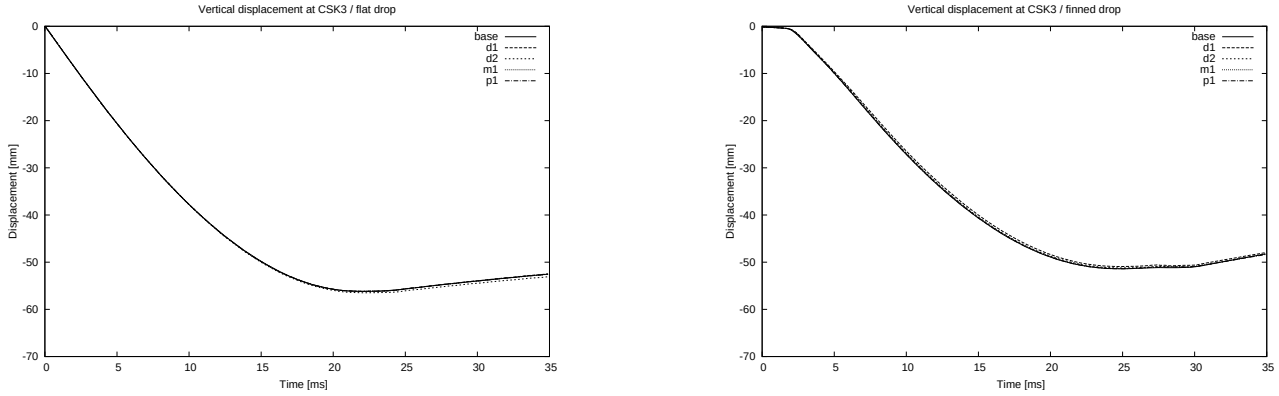

a *b*

Figure 3.76: *Computed vertical displacements at the CSK3 for different tie model configurations: flat (a) and finned target (b).*

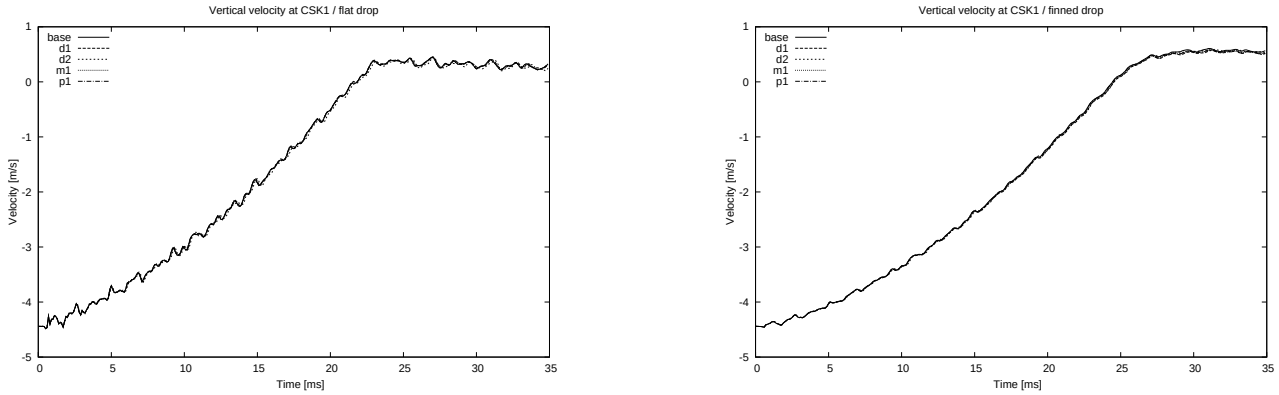

a *b*

Figure 3.77: *Computed vertical velocity at the CSK1 for different tie model configurations: flat (a) and finned target (b).*

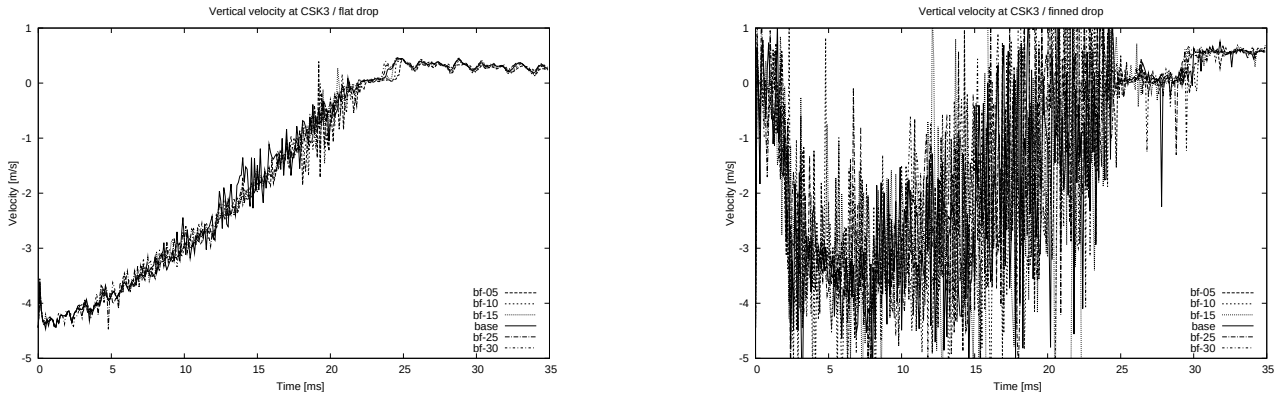

a *b*

Figure 3.78: *Computed vertical velocity at the CSK3 for different tie model configurations: flat (a) and finned target (b).*

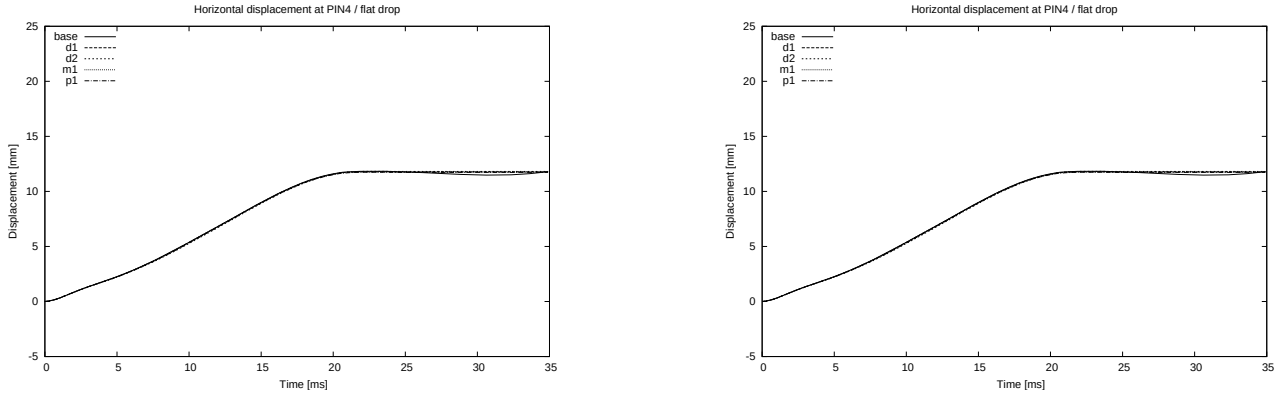

a *b*

Figure 3.79: *Computed horizontal displacement at the PIN4 for different tie model configurations: flat (a) and finned target (b).*

3.9 Influence of element type

The model is meshed with two different tetrahedral elements and compared to the Base Model (base). The linear tetrahedral elements (tet-lin) are used first and modified second-order tetrahedral elements (tet-mod) are used afterwards. The latter are an exception with ABAQUS/Explicit, which uses only linear elements. Hence, modified second-order tetrahedral elements can not be combined with any other elements.

The model meshed with the modified second-order tetrahedral elements for the finned target case has been computed only up to 26 ms out of 35 ms due to a hardware failure. The simulation was not repeated as the significant information was retrieved and due to long computational times. The model sizes and computational times are presented in Table 3.8. From the present analyses it is clear that tetrahedral elements requires significantly higher computational times and should be avoided if possible. If this is not possible it is impossible to say which tetrahedral elements are preferred. When combining different element types only linear tetrahedral elements apply due to ABAQUS/Explicit restrictions.

Table 3.8: *Model size and computational times; * estimated.*

Model	Drop type	Number of elements	Number of nodes	Number of degrees of freedom	CPU time [DD-HH:MM]
base	flat	20 058	21 609	64 830	00-08:14
	fins	19 042	22 427	67 284	00-03:59
tet-lin	flat	103 886	22 670	68 013	02-22:18
	fins	105 673	23 320	69 963	02-13:59
tet-mod	flat	103 886	263 073	789 222	27-20:49
	fins	105 673	268 558	805 677	21-21:56*

The artificial, total, kinetic and strain energies are presented in Fig. 3.80, 3.81, 3.82 and 3.83 respectively. A comparison of the reaction forces in the vertical directions is shown in Fig. 3.84 and the maximal principal strains at the D1 measurement point in Fig. 3.85. Vertical displacements at the points CSK1 and CSK3 are compared in Fig. 3.86 and 3.87 respectively. Vertical velocities at the points CSK1 and CSK3 are compared in Fig. 3.89 and 3.89. Horizontal displacements at the point PIN4 are compared in Fig. 3.90.

The results for the tet-lin are different from the results for the same element type in the report [1], Model **g**. The different partitioning of the models around the impact area is plausible cause for the difference in the model responses. The differences between responses are slightly larger than observed with different mesh densities or with different coefficients of friction used, but smaller than differences observed with the Johnson-Cook material model. The mesh consists of some small elements when the tetrahedral elements are used. This results in long computational times, Table 3.8, which is the major drawback.

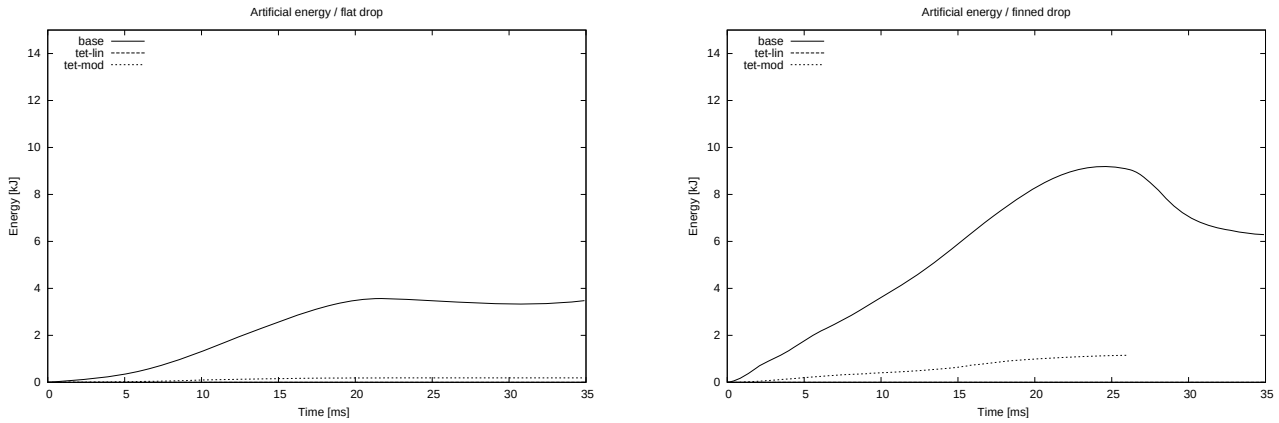

Figure 3.80: *Computed artificial energy for different element configurations: flat (a) and finned target (b).*

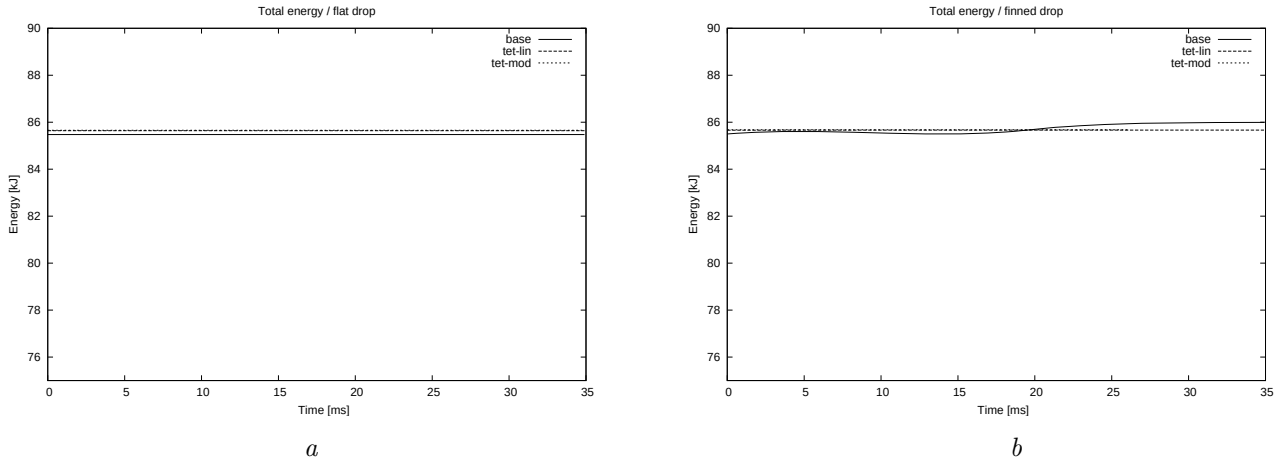

Figure 3.81: *Computed total energy for different element configurations: flat (a) and finned target (b).*

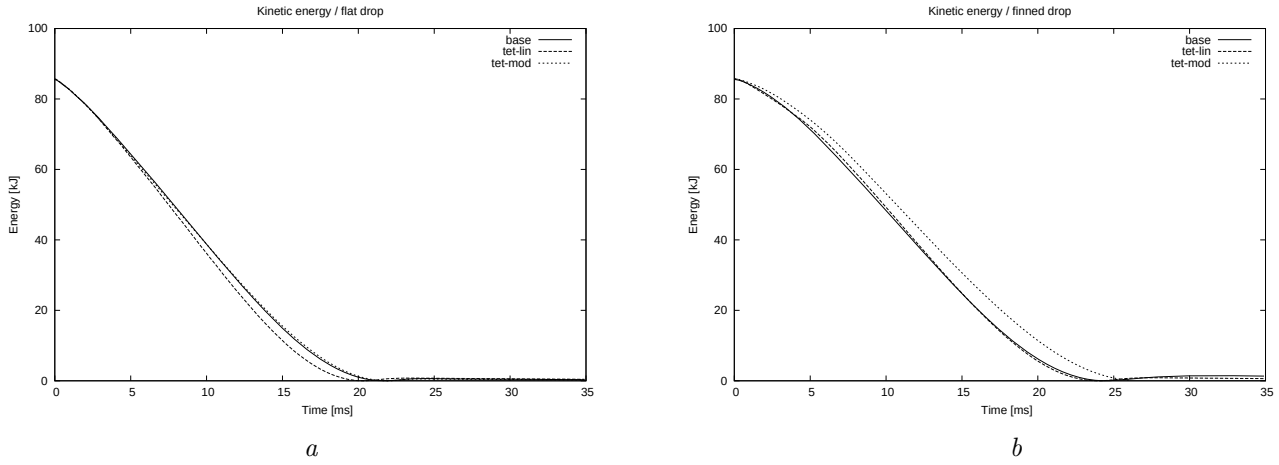

Figure 3.82: *Computed kinetic energy for different element configurations: flat (a) and finned target (b).*

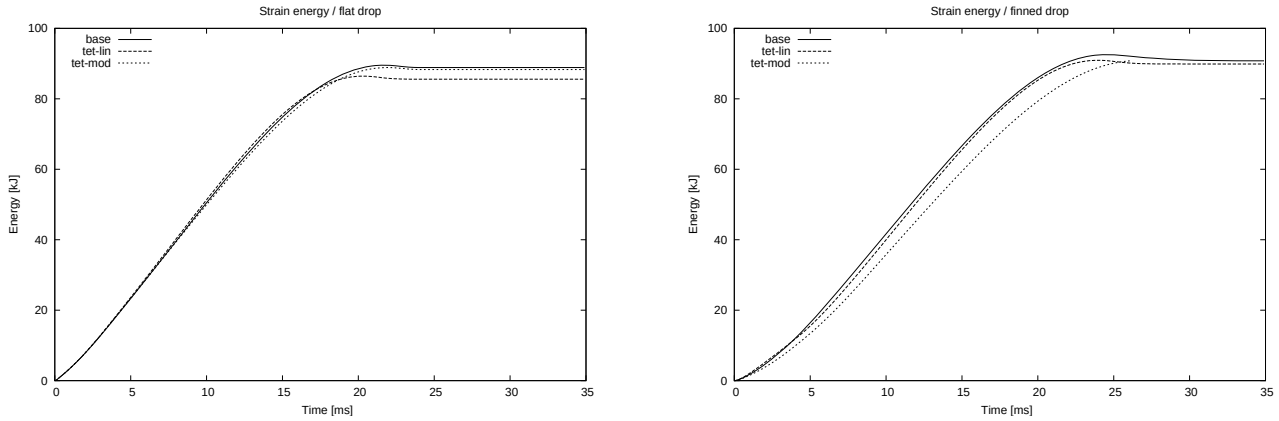

a *b*

Figure 3.83: *Computed strain energy for different element configurations: flat (a) and finned target (b).*

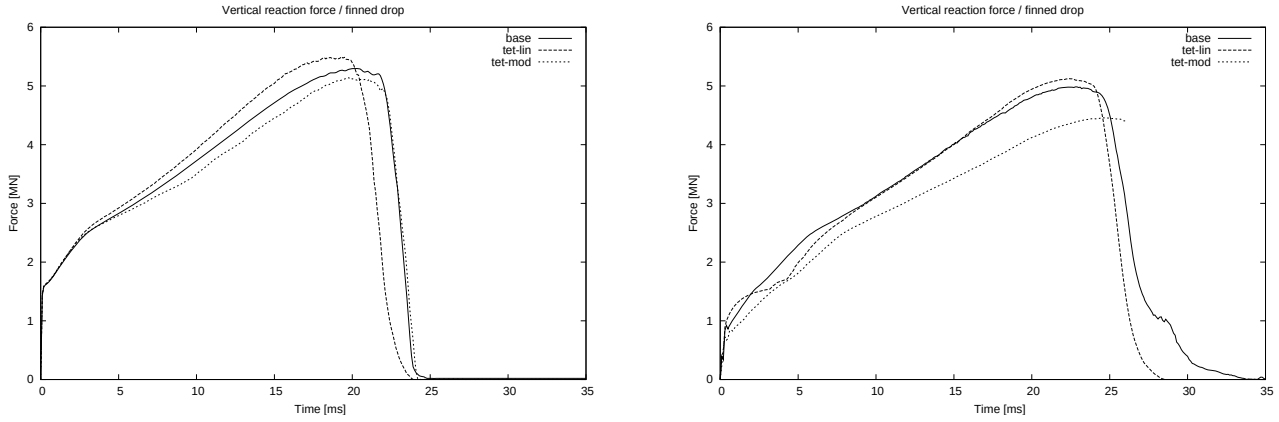

a *b*

Figure 3.84: *Computed vertical reaction forces for different element configurations: flat (a) and finned target (b).*

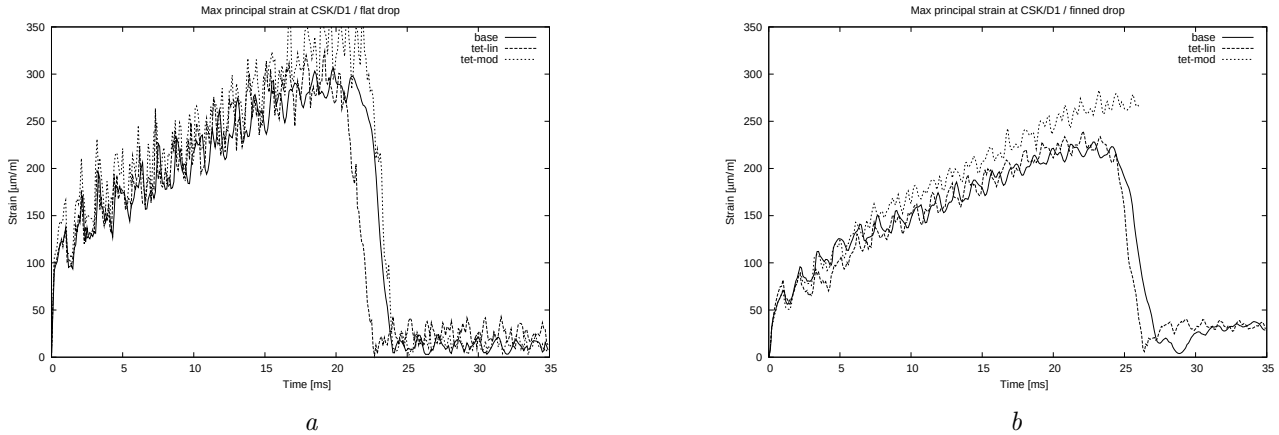

a *b*

Figure 3.85: *Computed maximal principal strains at the D1 for different element configurations: flat (a) and finned target (b).*

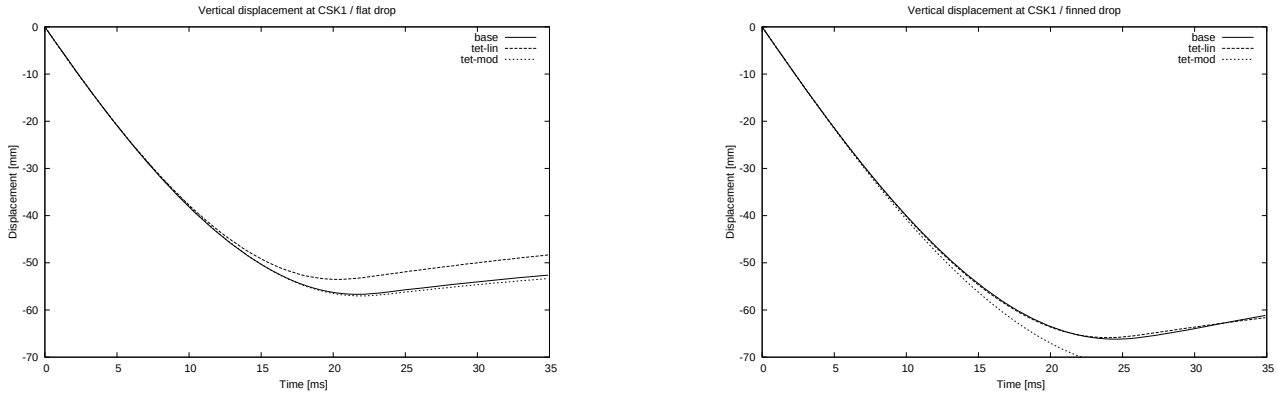

a *b*

Figure 3.86: *Computed vertical displacements at the CSK1 for different element configurations: flat (a) and finned target (b).*

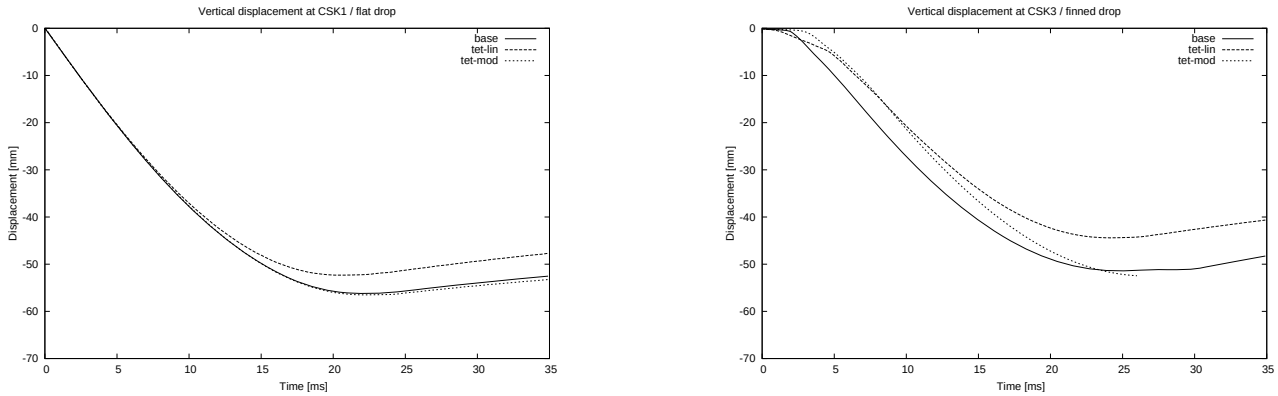

a *b*

Figure 3.87: *Computed vertical displacements at the CSK3 for different element configurations: flat (a) and finned target (b).*

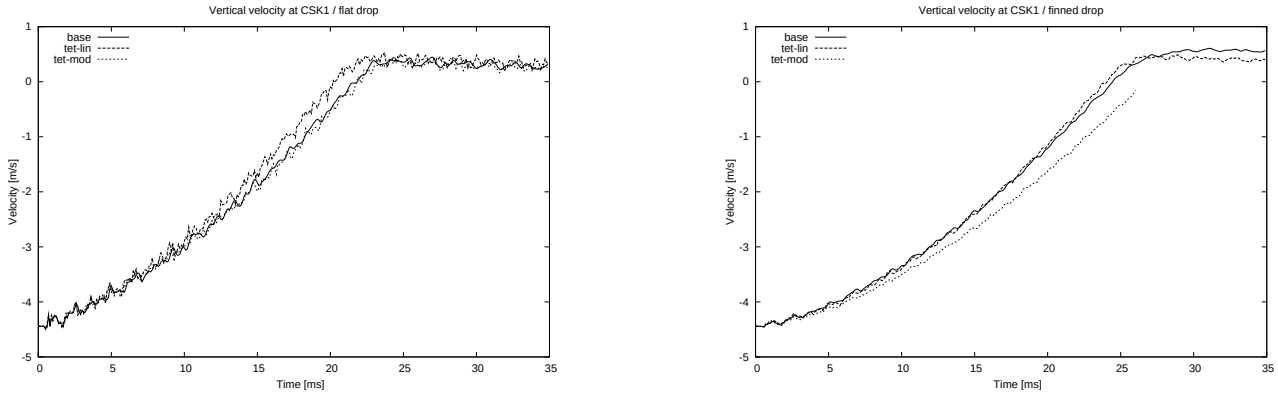

a *b*

Figure 3.88: *Computed vertical velocity at the CSK1 for different element configurations: flat (a) and finned target (b).*

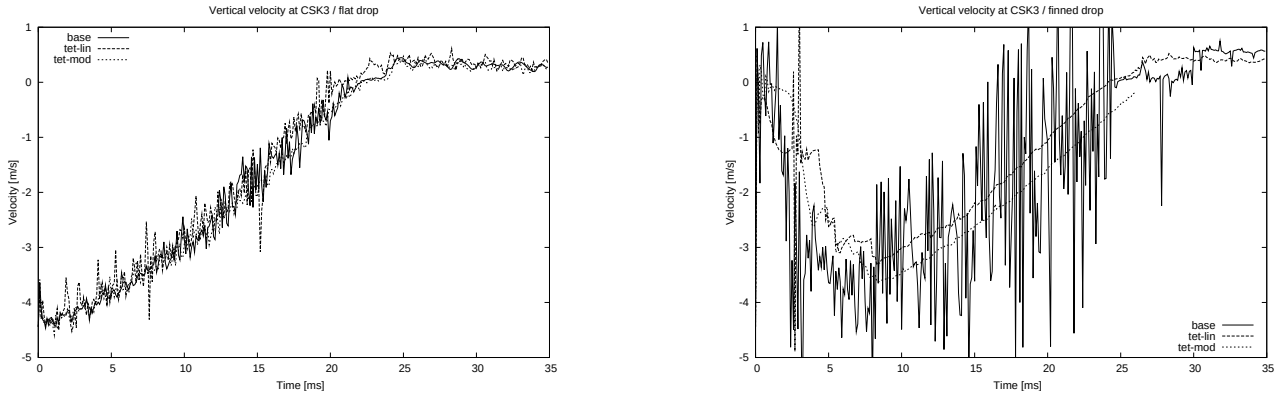

a *b*

Figure 3.89: *Computed vertical velocity at the CSK3 for different element configurations: flat (a) and finned target (b).*

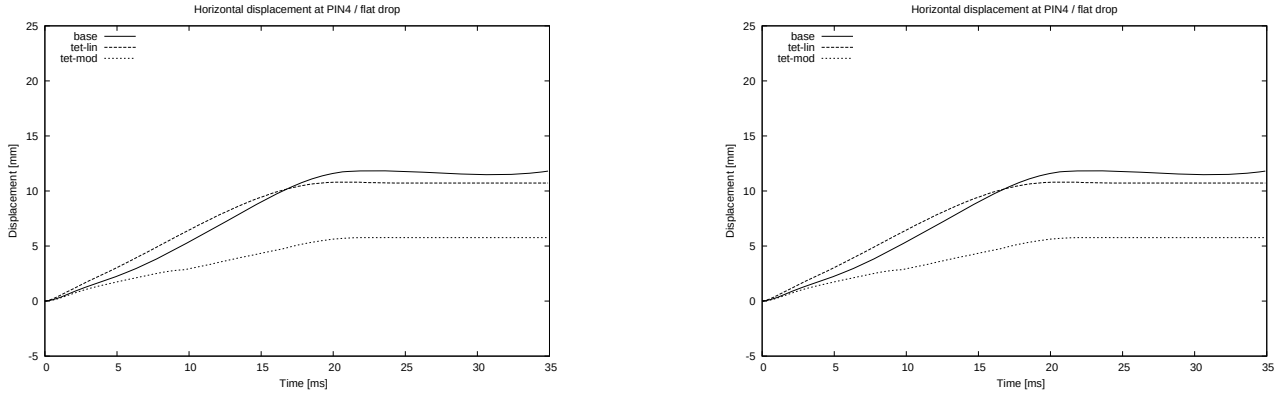

a *b*

Figure 3.90: *Computed horizontal displacement at the PIN4 for different element configurations: flat (a) and finned target (b).*

3.10 Conclusions

The analyses of the model behaviour presented in this chapter yield following conclusions:

- The Base Model was defined from the parameter study of the Model **a**. The differences between Base Model and Model **a** are significant and larger than differences due to the variation of basic model parameters.
- The supporting boundary conditions (SBC) without contact problem formulation between the bar and the ground are phenomenologically different to the SBC with the implemented contact. Differences of the results are modest ($\approx \pm 5\%$), particularly for vertical reaction force and horizontal displacement at the bar's bottom surface.
- Variation of the coefficient of friction in all of the contact areas scatters the model responses to up to $\pm 5\%$ around mid-value for technically acceptable range of coefficients of friction. The horizontal displacement of the bar's bottom surface is an exception and it was shown that it scales linearly with the coefficient of friction.
- The results were not sensitive to how the material data in tabular form was fitted to the experimental data in the small strain range. The Johnson-Cook model is not adequate for the material under consideration because it overestimates the vertical reaction force in the bar and strains in the cask.
- Mass scaling should be used with caution and the mass scaling factor should not exceed value of 8.
- No monotonous convergence of the bar's displacements was found when increasing the mesh density of the model. More variations are found at the point PIN4 in comparison with the point PIN3 due to the fact that the point PIN4 lies on the bottom bar surface where the frictional contact plays an important role.
- Tie constraints of the Base model are not affecting the results. Hence, the model set-up is appropriate.
- The analysis of the model meshed with the tetrahedral elements demand long computational times and should be avoided.

Chapter 4

Comparison between the experiment and simulation

4.1 Introduction

A comparison between the Base Model and the experimental results as well as a comparison between the Best Model and the experiment are presented in this chapter. The comparison between the Base Model and the experiment is of more information nature and not the final since the bar in experiment was 120 mm high and not 100 mm as stated in the originally supplied documentation. It is expected that this has some influence on results. Final analysis with the Best Model address the issue.

It was shown in previous chapter that the Base Model is a good candidate for the comparison. It seems that the mesh of Base Model is adequate but that the coefficient of friction is overestimated. There are two differences between the Base and Best Model:

- the length of the bar of the Best Model is 120mm whereas it is 100mm for the Base Model and
- the coefficient of the friction between the bar and the ground is decreased to $\mu = 0.08$ for the Best model whereas it was $\mu = 0.2$ for the Base Model.

Several quantities are compared qualitatively as well as quantitatively:

- vertical reaction force (rf2),
- equivalent (Mises) strain at D1 (ev), ε_v, eq. (4.1),
- equivalent (Mises) stress at D1 (sv), σ_v, eq. (4.2),
- displacement at CSK1 (u2),
- velocity at CSK1 (v2) and

- displacement at PIN0 (pu2).

The vertical force (rf2) is directly measured in the experiment. Equivalent strains and stresses are computed out of measured strain components at D1, equations 4.1 and 4.2. Displacements and velocities at CSK1 are not measured directly but are numerically integrated from the measured acceleration. Displacement at PIN0 is extracted from the speed-camera movie.

The equivalent strain is defined as [12]:

$$\varepsilon_v = \frac{1}{(1+\nu)\sqrt{2}}\sqrt{(\varepsilon_1-\varepsilon_2)^2+(\varepsilon_2-\varepsilon_3)^2+(\varepsilon_3-\varepsilon_1)^2} \tag{4.1}$$

The equivalent stress is defined as [12]:

$$\sigma_v = \frac{1}{\sqrt{2}}\sqrt{(\sigma_1-\sigma_2)^2+(\sigma_2-\sigma_3)^2+(\sigma_3-\sigma_1)^2} \tag{4.2}$$

4.2 Comparison between the Base Model and experimental results

Values of the extrema of the measured and simulated quantities and their positions, differences and relative differences can be found in Tab. 4.1.

Table 4.1: *Extrema (peak values) and their positions, differences and relative differences for the analyzed quantities.*

Extremum of the	Unit	Drop type	Experiment		Simulation		Difference		Relative difference
			Value	Time [ms]	Value	Time [ms]	Value	Time [ms]	[%]
Reaction force (rf2)	[MN]	flat	4.769	19.2	5.299	20.4	0.530	1.2	11.1
		fins	4.447	23.5	4.985	22.8	0.538	-0.7	12.1
Equivalent strain (ev)	[%]	flat	0.0386	19.0	0.0403	19.8	0.0017	0.8	4.4
		fins	0.0311	23.2	0.0298	22.8	-0.0087	-0.4	-4.1
Equivalent stress (sv)	[MPa]	flat	63.2	19.0	64.8	19.8	1.6	0.8	2.5
		fins	51.0	23.2	47.9	22.8	-3.1	-0.4	-6.1
Vertical velocity (v2)	[m/s]	flat	0.079	25.7	0.445	27.0	0.366	1.3	463
		fins	1.599	30.0	0.606	31.1	-0.993	1.1	-62
Vertical (u2) displacement	[mm]	flat	-58.9	24.0	-56.7	21.8	2.2	-2.2	3.7
		fins	-54.6	22.1	-66.2	24.4	-11.6	2.3	-21.2
Vertical (pu2) displacement	[mm]	flat	-54.3	21.2	-56.1	22.0	-1.8	0.8	-3.3
		fins	-47.8	21.3	-51.3	24.7	-3.5	3.4	-7.3
Horizontal (u1) displacement	[mm]	flat	16.4	/	11.8	/	-4.6	/	-28.0
		fins	/	/	/	/	/	/	/

Figure 4.1 shows the comparison of the vertical reaction forces. The maximal values of the simulated forces are overestimated by 11% for flat target drop and 12% for the finned one. Decreasing the coefficient of friction will increase the simulated force and the difference between experiment and simulation.

There is good agreement between the experiment and the simulation in equivalent strains and Mises stress, Fig. 4.2 and 4.3 respectively. The differences of the maximal values are less then 10% expect for the equivalent strains of the finned drop case.

Experimental vertical velocities and displacement on the cask (CSK1) weren't measured directly. They are obtained by numerical integration of the measured acceleration. The signals of the experimental and simulation's vertical displacement, Fig. 4.5, are qualitatively in good agreement. But in the finned case the difference in minima is just over 20%. The conclusions are similar when comparing signals of the vertical velocities, Fig. 4.4. Relative difference does not present reliable measure of error in this case due to almost zero value of the velocities' maxima.

The values of the vertical displacement on the bar (PIN0), Fig. 4.6, were extracted from the fast camera movie. The agreement between the experimental and the simulated signals is very good and final values varies less than 10%.

It can be seen in Tab. 4.1 that the horizontal displacement of the bar (PIN4) is underestimated. this is primarily due to overestimated model value for the coefficient of friction.

The time lag of the extrema in the finned drop case is generally smaller in the simulation than in the test.

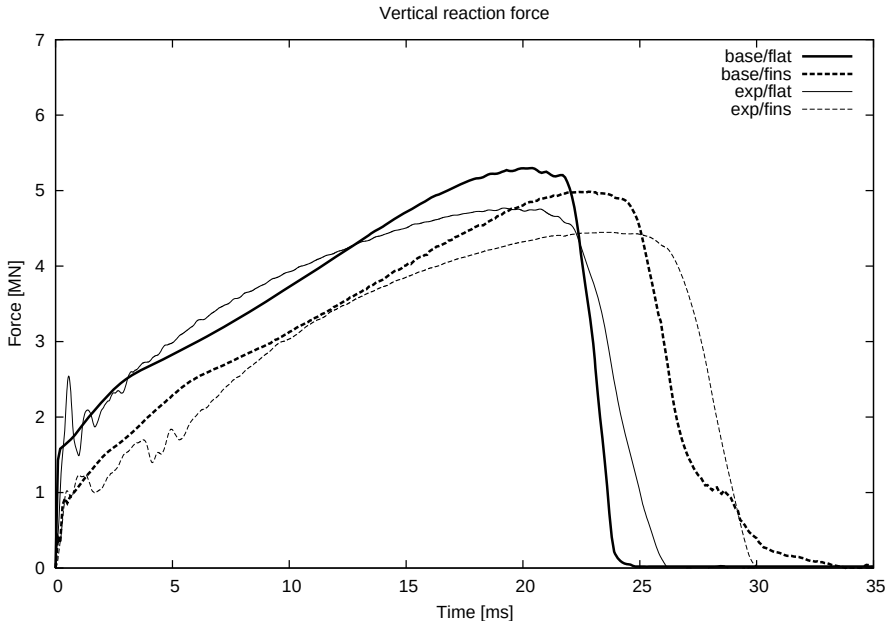

Figure 4.1: *Comparison of the vertical reaction force between the experiment and the base model.*

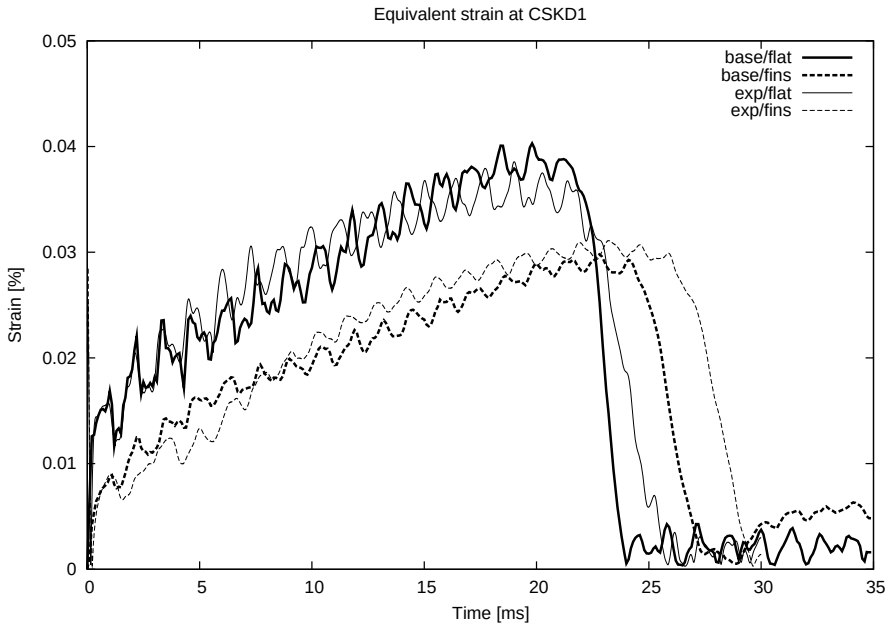

Figure 4.2: *Comparison of the equivalent strain at D1 between the experiment and the base model.*

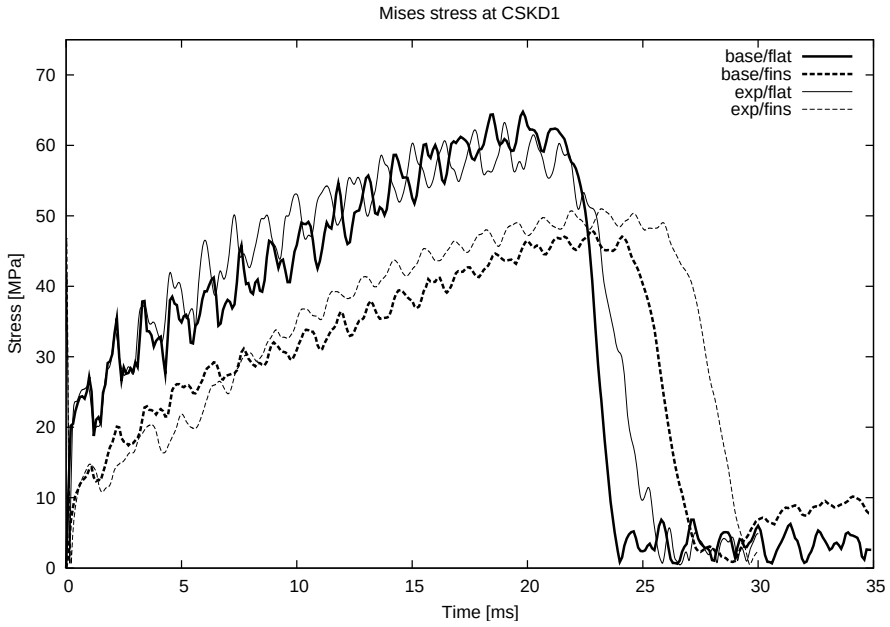

Figure 4.3: *Comparison of the equivalent stress at D1 between the experiment and the base model.*

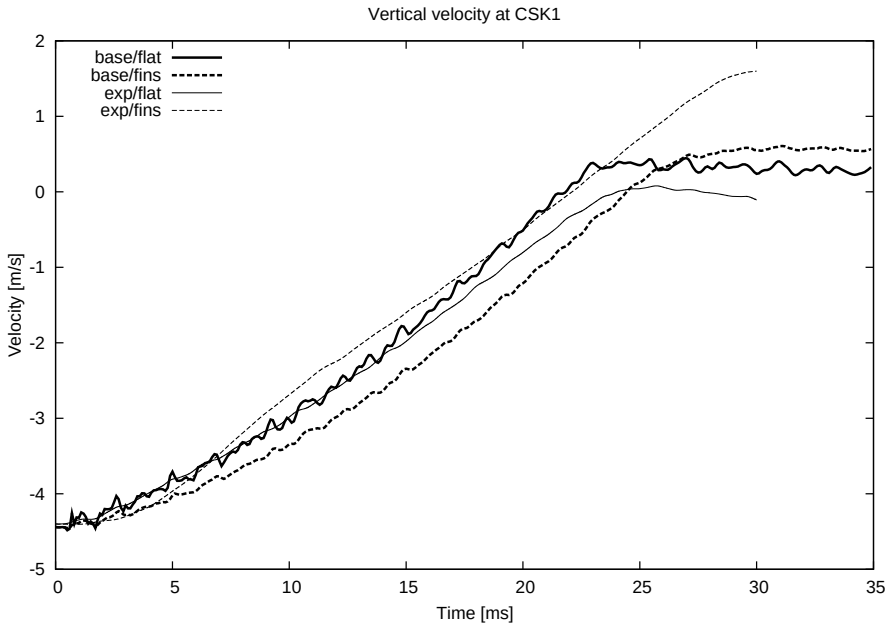

Figure 4.4: *Comparison of the vertical velocity at CSK1 between the experiment and the base model.*

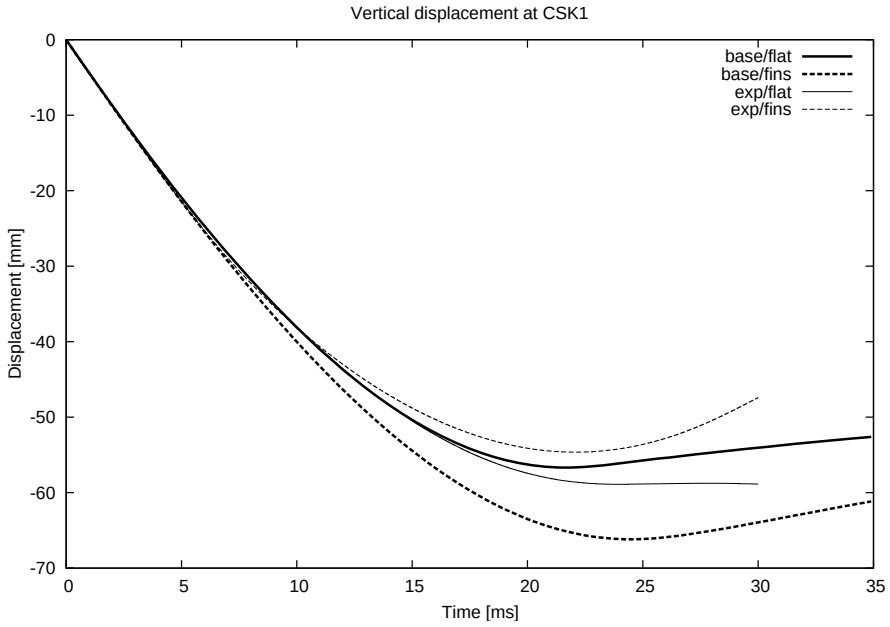

Figure 4.5: *Comparison of the vertical displacement at CSK1 between the experiment and the base model.*

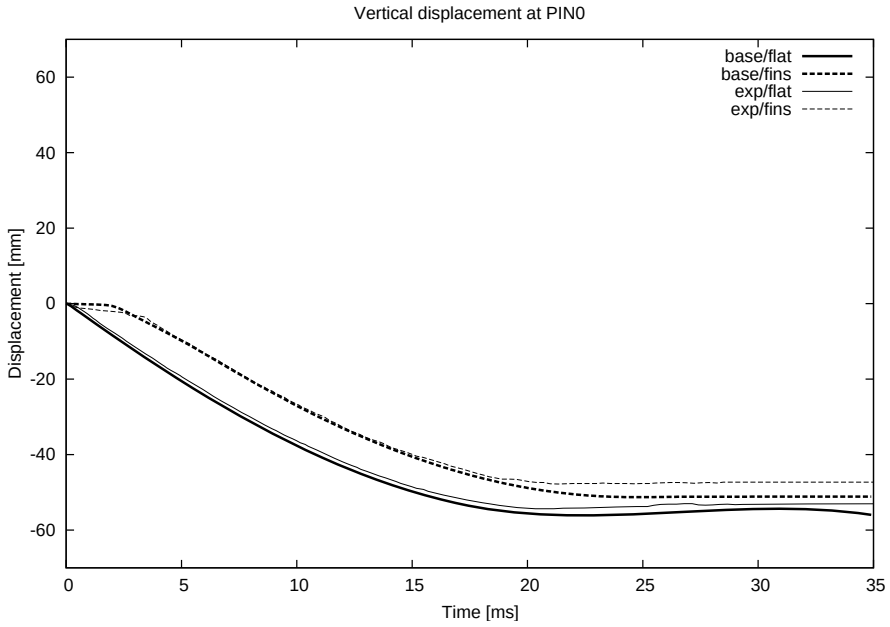

Figure 4.6: *Comparison of the vertical displacement at PIN0 between the experiment and the base model.*

4.3 Comparison between the Best Model and experimental results

The total mass of the cask model is 8667 kg, which is in good agreement with the real cask's half mass of 8655 kg. The estimated difference is -0.1%.

Values of the extrema of the measured and simulated quantities and their positions, differences and relative differences are shown in Tab. 4.2.

Figure 4.7 shows the comparison of the vertical reaction forces. The maximal values of the simulated forces are underestimated by 6% for flat target drop and 5% for the finned one.

There is good agreement between the experiment and the simulation in equivalent strains and Mises stress, Fig. 4.8 and 4.9 respectively. The differences of the maximal values are less then 10% for the flat drop case. For the finned drop case the difference is below 20%.

Experimental vertical velocities and displacement on the cask (CSK1) weren't measured directly. They are obtained by numerical integration of the measured acceleration. The signals of the experimental and simulation's vertical displacement, Fig. 4.11, are qualitatively in good agreement. But in the finned case the difference in minima is just over 20%. The conclusions are similar when comparing signals of the vertical velocities, Fig. 4.10. Relative difference does not present reliable measure of error in this case due to almost zero value of the velocities' maxima.

The values of the vertical displacement on the bar (PIN0), Fig. 4.12, were extracted from the fast camera movie. The agreement between the experimental and the simulated signals is relatively good and final values varies around or less than 20%.

Table 4.2: *Extrema (peak values) and their positions, differences and relative differences for the analyzed quantities.*

Extremum of the	Unit	Drop type	Experiment		Simulation		Difference		Relative difference
			Value	Time [ms]	Value	Time [ms]	Value	Time [ms]	[%]
Reaction force (rf2)	[MN]	flat	4.769	19.2	4.479	21.8	-0.290	2.6	-6.1
		fins	4.447	23.5	4.204	24.4	-0.243	0.9	-5.5
Equivalent strain (ev)	[%]	flat	0.0386	19.0	0.0361	22.7	-0.0025	3.7	-6.5
		fins	0.0311	23.2	0.0259	24.2	-0.0052	1.0	-16.7
Equivalent stress (sv)	[MPa]	flat	63.2	19.0	58.0	22.7	-5.2	3.7	-8.2
		fins	51.0	23.2	41.6	24.2	-9.4	1.0	-18.4
Vertical velocity (v2)	[m/s]	flat	0.079	25.7	0.382	27.0	0.303	1.3	383
		fins	1.599	30.0	0.520	32.9	-1.079	2.9	-67.5
Vertical (u2) displacement	[mm]	flat	-58.9	24.0	-62.7	24.4	-3.8	0.4	6.5
		fins	-54.6	22.1	-71.6	27.0	-17.0	4.9	31.1
Vertical (pu2) displacement	[mm]	flat	-54.3	21.2	-62.2	24.6	-7.9	3.4	14.5
		fins	-47.8	21.3	-57.4	27.4	-9.6	6.1	20.1
Horizontal (u1) displacement	[mm]	flat	16.4	/	12.8	/	-3.6	/	-22.0
		fins	/	/	/	/	/	/	/

It can be seen in Tab. 4.2 that the horizontal displacement of the bar (PIN4) is underestimated. This is primarily due to complex physics in the contact between the bar and the force transducer.

The time lag of the extrema in the finned drop case is generally smaller when comparing simulation results with the experimental ones.

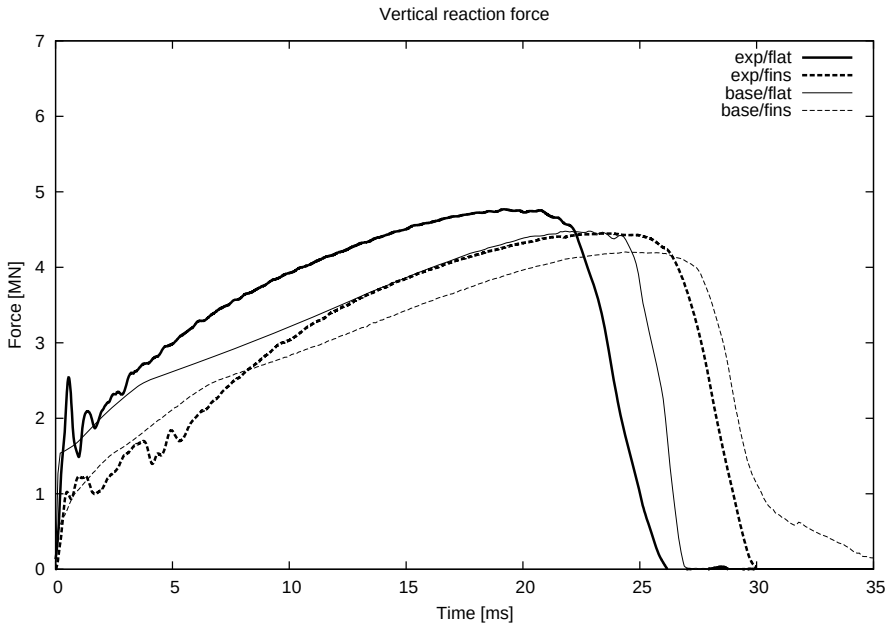

Figure 4.7: *Comparison of the vertical reaction force between the experiment and the base model.*

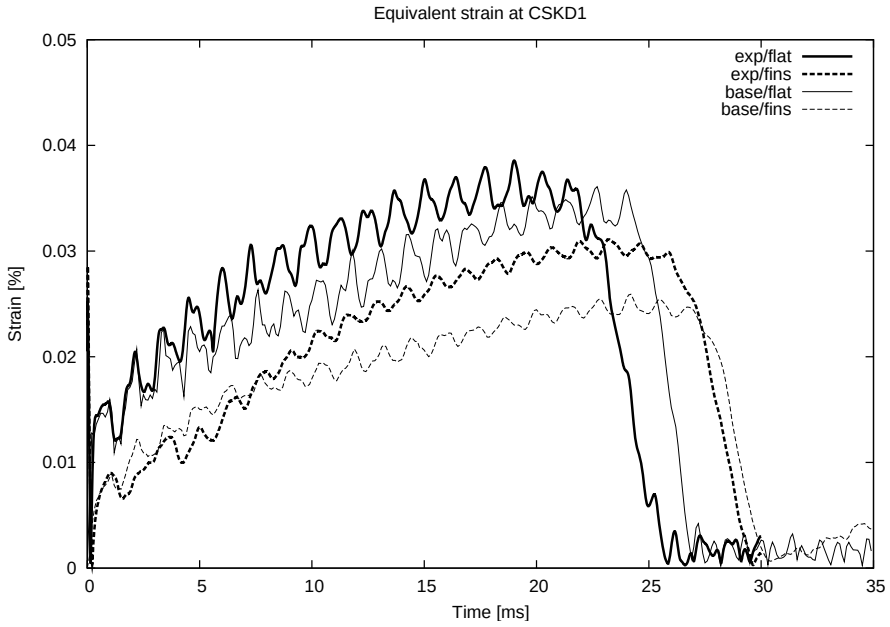

Figure 4.8: *Comparison of the equivalent strain at D1 between the experiment and the base model.*

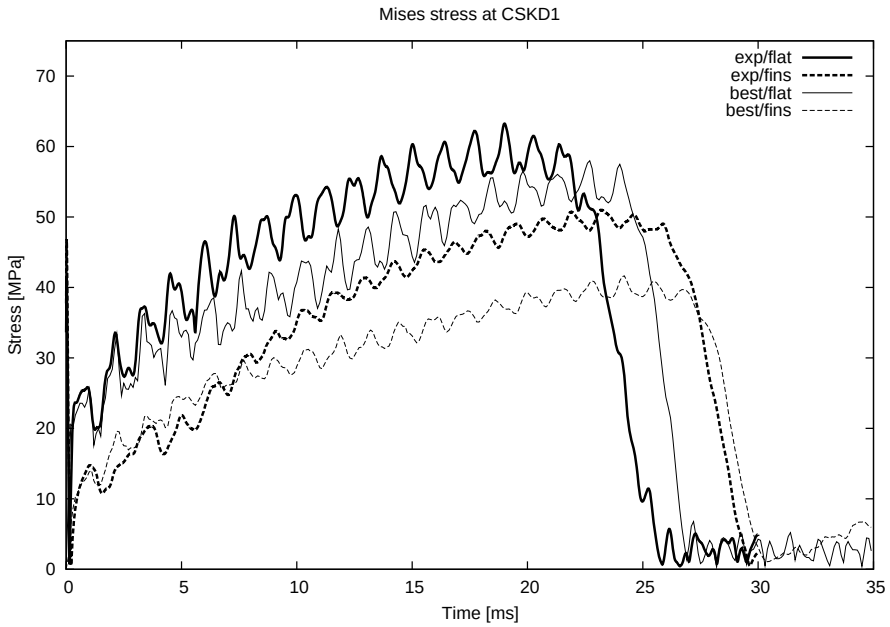

Figure 4.9: *Comparison of the equivalent stress at D1 between the experiment and the base model.*

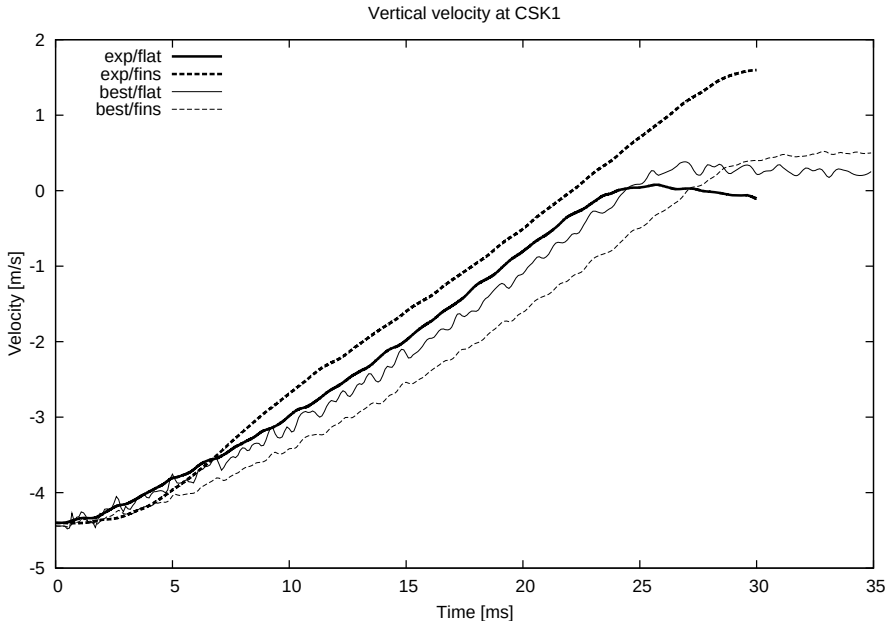

Figure 4.10: *Comparison of the vertical velocity at CSK1 between the experiment and the base model.*

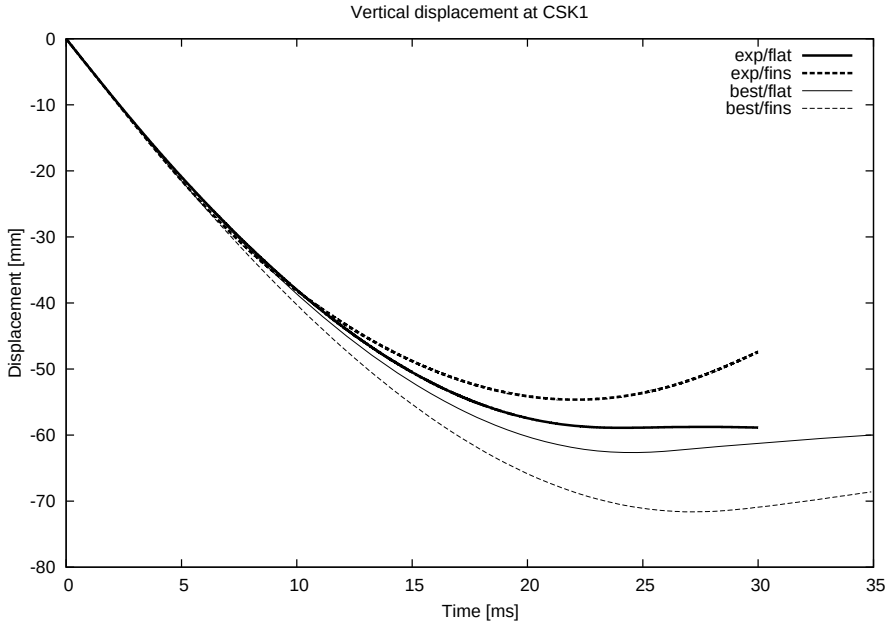

Figure 4.11: *Comparison of the vertical displacement at CSK1 between the experiment and the base model.*

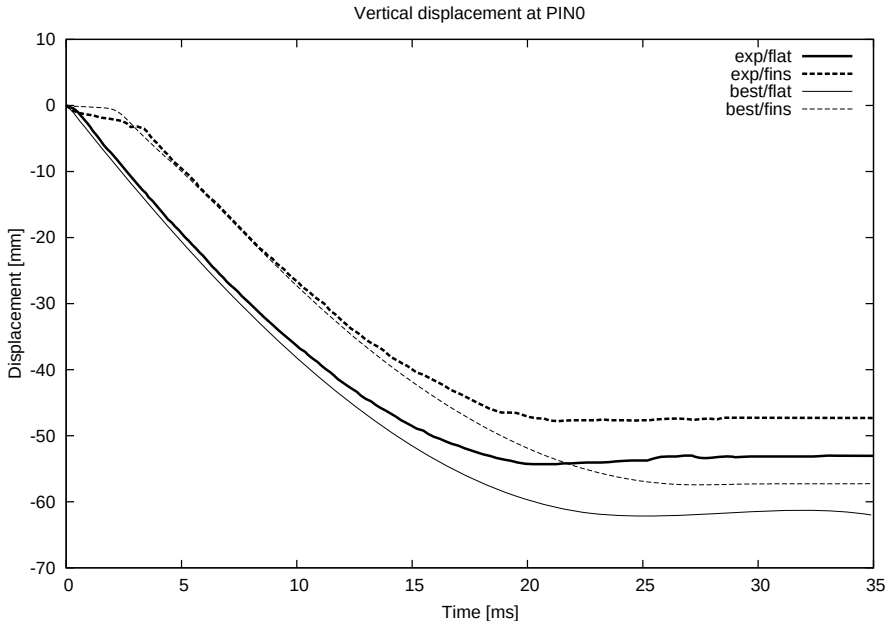

Figure 4.12: *Comparison of the vertical displacement at PIN0 between the experiment and the base model.*

4.4 Conclusions

The predictions from the Best Model and Base Model are both in relative good agreement with the experimental data for the main parameters as seen in Figure 4.13.

The Best Model, which has bar length of 120mm and $\mu = 0.08$ underestimates the reaction force and equivalent strain whereas the Base Model gives about 20% higher values than the Best Model. Both models underestimate the time lag for times, where extrema of certain quantities occur, between the finned and flat tests. Similar trends can be seen for the displacements.

There are two aspects that we believe could be relatively important and which we have not addressed.

1. Only tensile material curves were used. It is well known that the ductile cast iron has more hardening in compression than tension. The cask will be loaded in both tension and compression.
2. The fins failed in the experiment [1] but no failure nor damage models were implemented. It can be noted that the discrepancy between the Best Model and experiment is somewhat larger for the finned drop test, which can be seen as an indication of the relative importance of failure for the measured quantities.

There are more detailed conclusions for each model.

Base model

- The reaction forces are overestimated.
- The equivalent strains and Mises stresses are very well modelled.

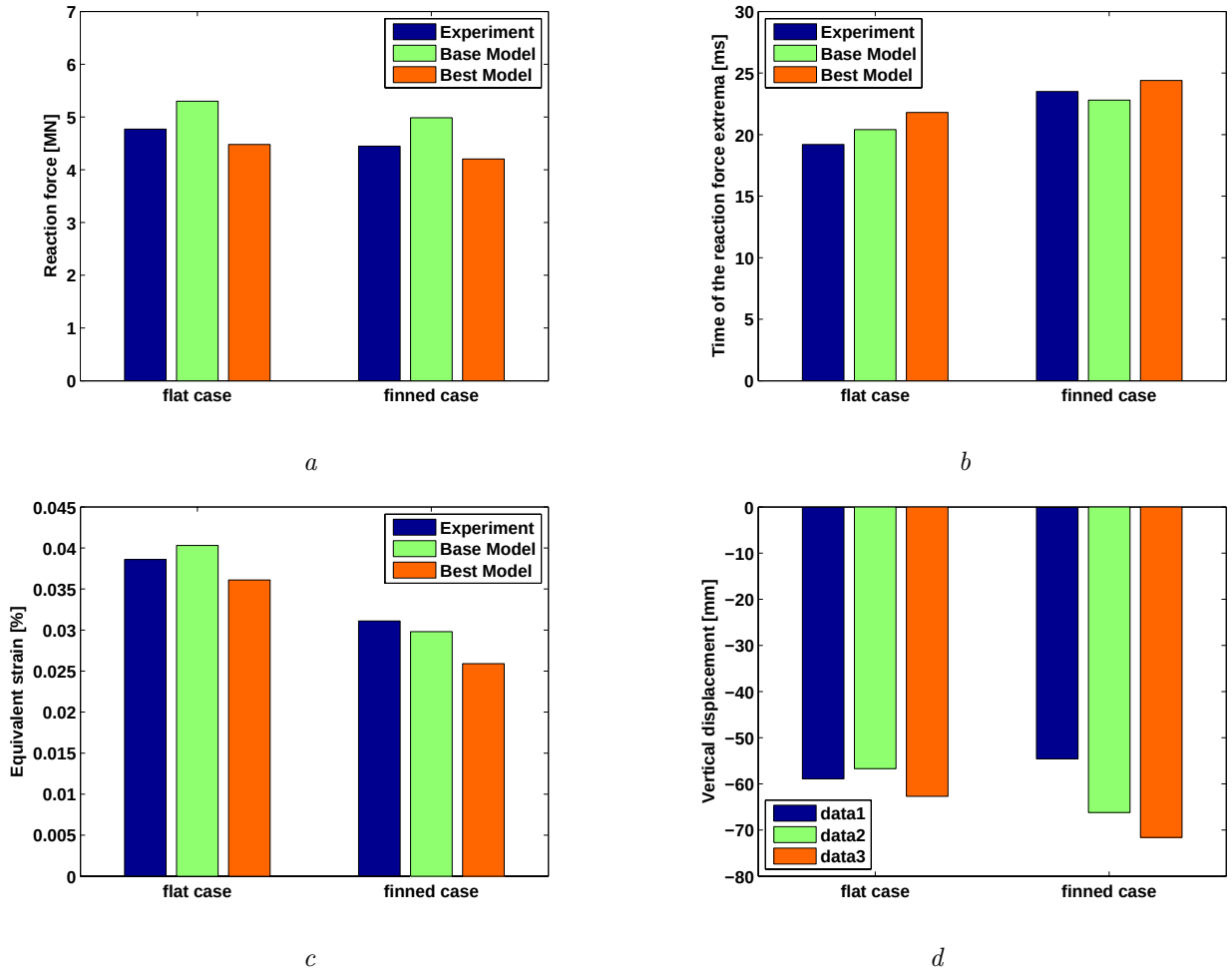

Figure 4.13: *Comparison between experiment and models, Base and Best: reaction forces (a), time of the reaction force extrema (b), equivalent strains (c) and vertical displacements (d).*

- Vertical velocities and displacement show similar behaviour. Some differences can occur due to integration of the measured cask's accelerations.
- The time gap between the flat and finned drop is slightly underestimated for the simulation.

Best model

- The reaction forces are underestimated.
- The equivalent strains and Mises stresses are well modelled.
- Vertical velocities and displacement show similar behaviour. Some differences can occur due to integration of the measured cask's accelerations.
- The time gap between the flat and finned drop is slightly underestimated for the simulation.

Chapter 5

Summary conclusions

This chapter summarize conclusions of the whole work on the numerical simulation of the one meter drop test on a bar for the CASTOR cask presented in two reports. The initial and sensitivity analyses are presented in [1] whereas the advanced and final analyses of the work are presented in this report.

The work is concerned with the numerical analysis of two one meter drop tests of a single ductile cast iron cask on a steel bar. The cask comes from the CASTOR family with machined cooling fins in a region where impact occurs. In the first test, the impact is on the cask's cooling fins whereas in the second test the impact is in an area where the fins have been locally machined away. The numerical analysis is based on explicit dynamic analysis using the commercial finite element code ABAQUS extended with Python scripts to allow a parametric description of the problem.

5.1 Model verification

The overall behavior of the model is qualitatively very similar to what was observed during the experiments. A longer impact duration, when the cask is dropped on the fins in comparison to the flat target, is observed in both the analysis and the test. The reaction force at the bar's bottom surface, equivalent strain and stress at the point D1, vertical displacement and velocities at the point CSK1 and horizontal displacement at the point PIN4 of the model are qualitatively and quantitatively similar to the experimental data. There are more detailed conclusions of the Best Model, such as:

- The reaction forces are underestimated.
- The equivalent strains and Mises stresses are modelled well.
- Vertical velocities and displacement show similar behaviour. Some differences can occur due to integration of the measured cask's accelerations.
- The time gap between the flat and finned drop is slightly underestimated for the simulation.

Only tensile material data was used for the cask and material failure was not modelled. It is possible that the simulation results might be quite affected if tension/compression material curves and material failure/damage were considered.

5.2 Parameter sensitivity analysis

The sensitivity analysis was performed to study the influence of different parameters which either cannot be or were not defined directly from the experimental data, such as the friction coefficient, or which are linked to the FE numerical procedures, like the bulk viscosity. Summary of detailed conclusions ordered by relative significance of the impact on the model responses are as follows:

- The model with the finer mesh generally yields somewhat better results than the model with the coarser one, but needs a lot of time to calculate the response. But, no monotonous convergence of the bar's displacement responses were found when increasing the mesh density of the model. *The model is not very mesh sensitive.*
- *The tetrahedral elements should be avoided* due to the long computational times.
- *The Johnson-Cook model is not adequate for the material under consideration* because it overestimates the vertical reaction force in the bar and the strains in the cask.
- The supporting boundary conditions (SBC) without contact problem formulation between the bar and the ground are phenomenologically different for the SBC with the implemented contact. Differences of the results are generally modest, but somewhat higher particularly for the vertical reaction force and horizontal displacement at the bar's bottom surface. The global deformation of the bar was more accurately modelled with the contact model.
- *Variation of the coefficient of friction for technically acceptable range in all of the contact areas scatters the model responses to by* $\pm 5\%$. The horizontal displacement of the bar's bottom surface is an exception and it was shown that it scales linearly with the coefficient of friction. The value of the coefficient of friction is estimated to be 0.08.
- *Mass scaling should be used with caution* and the mass scaling factor should not exceed value of 8.
- *The analysis did not clearly indicate the optimal hourglass control. However, the enhanced hourglass control seems to work relatively well for this analysis.* The Kelvin - pure stiffness hourglass formulation should be avoided. The integral viscoelastic hourglass formulation gives the lowest artificial energy in the case of the finned target drop. The Kelvin - pure viscous hourglass formulation gives the lowest artificial energy in the case of the flat target drop.
- The default values of the bulk parameters in ABAQUS/Explicit should be decreased in order to decrease the artificial energy.

Appendix A

Geometry parameters definition

Parameters are used in the drop test, analysis, geometry, mesh, loads, etc. definitions. The switches are parameters used for decision making inside the script. For example, whether a part should be modelled (switch is 1) or not (switch is 0).

The switches are presented in table A.1 and the parameters in table A.2. There is also reference to the file where switch/parameter can be found. The geometry parameters are also graphically described and the reference to the figure is given in the table. Parameters are printed in blue colour, geometry defining points in red colour and measuring points in green colour in following figures.

Table A.1: *List of the switches.*

Switch name	Def. value	Description	File
sw_csk	1	modelling the cask 0 = do not model the cask 1 = do model the cask	`01-parameters.py`
sw_pin	1	modelling of the bar 0 = do not model the bar 1 = do model the bar	`01-parameters.py`
sw_csk_rc	1	modelling of the cask's circumferential fins 0 = do not model the fins 1 = do model the fins	`01-parameters.py`
sw_csk_cc	0	modelling of the cask's circumferential channel 0 = do not model the channel 1 = do model the channel	`01-parameters.py`
sw_lid_bh	0	modelling of the lids's bolt holes 0 = do not model the holes 1 = do model the holes	`01-parameters.py`
sw_csk_mm	0	method of modelling of the cask's material 0 = tabular material data 1 = Johnson-Cook model	`01-parameters.py`

Table A.1: *(continued...)*

Switch name	Def. value	Description	File
sw_lid_mm	0	method of modelling of the lids's material 0 = tabular material data 1 = Johnson-Cook model	`01-parameters.py`
sw_pin_mm	0	method of modelling of the bar's material 0 = tabular material data 1 = Johnson-Cook model	`01-parameters.py`

Table A.2: *List of the parameters.*

Param. name	Value	Unit	Description	File	Figure
Tolerances and basic numeric parameters					
dropTol	10^{-6}	m	tolerance of the length	`01A-basic.py`	/
dropTolAngle	10^{-3}	rad	tolerance of the angle	`01A-basic.py`	/
pidiv180	0.017...	/	$\pi/180$	`01A-basic.py`	/
twopi	6.283...	/	2π	`01A-basic.py`	/
gravity	9.80665	m/s^2	gravity constant	`01A-basic.py`	/
eps	10^{-4}	m	small length	`01A-basic.py`	/
epsAng	10^{-2}	m	small angle	`01A-basic.py`	/
Drop test parameters					
dropJobName	'dropTest'	/	the name of the job	`01B-analysis.py`	/
dropJobType	0	/	the job type definition 0 = data check 1 = analysis	`01B-analysis.py`	/
dropJobSubmit	0	/	submit the job? 0 = no 1 = yes	`01B-analysis.py`	/
dropDuration	35	ms	duration of the drop job	`01B-analysis.py`	/
dropHeight	1.006-eps	m	the drop height	`01B-analysis.py`	/
dropFlat	0	/	the cask's drop target 0 = drop on the finned target 1 = drop on the flat target	`01B-analysis.py`	/
dropFreq	10	/	number of frames per millisecond	`01B-analysis.py`	/
dropDataFreq	1	/	number of history data per frame	`01B-analysis.py`	/
Analysis parameters					
anaMassScaling	0	/	do the mass scaling? 0 = no 1 = yes	`01B-analysis.py`	/

Table A.2: *(continued...)*

Param. name	Value	Unit	Description	File	
anaTimeStep	10^{-7}	s	minimal integration time step for mass scaling	`01B-analysis.py`	/
anaLinBulkVis	0.03	/	coefficient of the linear bulk viscosity	`01B-analysis.py`	/
anaQuadBulkVis	0.6	/	coefficient of the quadratic bulk viscosity	`01B-analysis.py`	/
anaFricCoef	0.2	/	coefficient of dry friction in contact between the cask and bar	`01B-analysis.py`	/
anaFricCoefGround	0.2	/	coefficient of dry friction in contact between the bar and ground	`01B-analysis.py`	/
anaContactMethod	0	/	contact method formulation 0 = penalty 1 = frictionless	`01B-analysis.py`	/
anaElemType	0	/	element type 0 = HEX where possible 1 = TET everywhere	`01B-analysis.py`	/
anaHourglassControl	0	/	type of the hourglass control 0 = enhanced 1 = relaxed stiffness 2 = stiffness 3 = viscous	`01B-analysis.py`	/
anaSupportBC	2	/	definition of the support boundary conditions 0 = encastred at srew 1 = encastred everywhere 2 = contact formulation	`01B-analysis.py`	/
Parameters of the MODEL					
rotationAngle	180	°	angle of the model's cross-section rotation	`01-parameters.py`	/
Parameters of the CASK					
_csk_Rmin	5	mm	minimal radius for fillets	`01C0-cask.py`	/
_csk_Lo	2645	mm	cask length	`01C0-cask.py`	A.1
_csk_Do	1230	mm	cask diameter	`01C0-cask.py`	A.1
_csk_Rt	20	mm	radius of the cask's fillet at the top	`01C0-cask.py`	A.1
_csk_Rb	45	mm	radius of the cask's fillet at the battom	`01C0-cask.py`	A.1
_csk_Hsa	700	mm	height of the cask's storage space A	`01C0-cask.py`	A.2
_csk_Hsb	976	mm	height of the cask's	`01C0-cask.py`	A.2

Table A.2: *(continued...)*

Param. name	Value	Unit	Description	File	
			storage space B		
_csk_Hsc	644	mm	height of the cask's storage space C	01C0-cask.py	A.2
_csk_Dsa	658	mm	inner diameter of the cask's storage space A	01C0-cask.py	A.1
_csk_Dsb	632	mm	inner diameter of the cask's storage space B	01C0-cask.py	A.1
_csk_Dsc	632	mm	inner diameter of the cask's storage space C	01C0-cask.py	A.1
_csk_Hla	32	mm	height of the cask's lid seat A	01C0-cask.py	A.2
_csk_Hlb	165	mm	height of the cask's lid seat B	01C0-cask.py	A.2
_csk_Hlc	305	mm	height of the cask's lid seat C	01C0-cask.py	A.2
_csk_Dla	990	mm	diameter of the cask's lid seat A	01C0-cask.py	A.1
_csk_Dlb	940	mm	diameter of the cask's lid seat B	01C0-cask.py	A.1
_csk_Dlc	665	mm	diameter of the cask's lid seat C	01C0-cask.py	A.1
_csk_Rla	2.5	mm	fillet radius of the cask's lid seat A	01C0-cask.py	A.1
_csk_Rlb	2.5	mm	fillet radius of the cask's lid seat B	01C0-cask.py	A.1
_csk_Rlc	6	mm	fillet radius of the cask's lid seat C	01C0-cask.py	A.1
_csk_Hv	10	mm	height of the cask's bottom void	01C0-cask.py	A.2
_csk_Dv	1040	mm	diameter of the cask's bottom void	01C0-cask.py	A.2
_csk_Hcc	16	mm	height of the cask's circumferential channel	01C0-cask.py	A.2
_csk_Dcc	652	mm	diameter of the cask's circumferential channel	01C0-cask.py	A.1
_csk_Pcc	16	mm	position of the cask's circumferential channel	01C0-cask.py	A.2
_csk_Rcc	2.5	mm	fillet radius of the cask's circumferential channel	01C0-cask.py	A.1
_csk_Lr	1319	mm	position of the center	01C0-cask.py	A.2

Table A.2: *(continued...)*

Param. name	Value	Unit	Description	File	
			of the cask's fins		
_csk_Nr	5	/	half number of the cask's fins	01C0-cask.py	A.3
_csk_Sr	22.5	mm	step of the cask's fins	01C0-cask.py	A.3
_csk_Or	5	mm	half thickness of the cask's fins	01C0-cask.py	A.3
_csk_Pr	2.5	mm	half thickness of the cask's fins at the top	01C0-cask.py	A.3
_csk_Rr	6.25	mm	fillet radius of the cask's fins at the bottom	01C0-cask.py	A.3
_csk_Dr	30	mm	depth of the cask's fins	01C0-cask.py	A.3
_csk_Lf	582	mm	distance from the cask's flat target to the cask's centerline	01C0-cask.py	A.2
_csk_La2	1200	mm	distance of the accelerometer from the cask's bottom	01C0-cask.py	A.2
_csk_Dsi	100	mm	inner diameter of the strain gauges measurement positions	01C0-cask.py	A.4
_csk_Dso	200	mm	outer diameter of the strain gauges measurement positions	01C0-cask.py	A.4
Parameters of the LID					
_lid_Rmin	1	mm	minimal radius for fillets	01C1-lid.py	/
_lid_H	300	mm	lid height	01C1-lid.py	A.5
_lid_Ht	164	mm	height of lid top	01C1-lid.py	A.5
_lid_D	937	mm	lid diameter	01C1-lid.py	A.5
_lid_Db	658	mm	diameter of lid bottom	01C1-lid.py	A.5
_lid_Nb	24	/	number of circumferential bolts	01C1-lid.py	/
_lid_Nbb	3	/	number of circumferential big bolts	01C1-lid.py	/
_lid_C1	5	mm	top chamfer	01C1-lid.py	A.5
_lid_C2	5	mm	mid chamfer	01C1-lid.py	A.5
_lid_C3	5	mm	bottom chamfer	01C1-lid.py	A.5
_lid_Dc	30	mm	central bolt hole diameter	01C1-lid.py	A.5
_lid_Hc	55	mm	central bolt hole depth	01C1-lid.py	A.5
_lid_Dbo	76	mm	bigger bolt hole outer diameter	01C1-lid.py	A.5
_lid_Dbi	45	mm	bigger bolt hole inner diameter	01C1-lid.py	A.5
_lid_Hb	52	mm	bigger bolt hole depth	01C1-lid.py	A.5
_lid_Dso	61	mm	smaller bolt hole outer diameter	01C1-lid.py	A.5
_lid_Dsi	39	mm	smaller bolt hole inner diameter	01C1-lid.py	A.5
_lid_Hs	95	mm	smaller bolt hole depth	01C1-lid.py	A.5
Parameters of the BAR					
_pin_Rmin	1	mm	minimal radius for fillets	01C3-pin.py	/

Table A.2: *(continued...)*

Param. name	Value	Unit	Description	File	
_pin_R	3	mm	fillet radius	`01C3-pin.py`	A.6
_pin_H	100	mm	bar height	`01C3-pin.py`	A.6
_pin_D	75	mm	bar diameter	`01C3-pin.py`	A.6
_pin_Db	20	mm	bolt diameter	`01C3-pin.py`	A.6
Parameters of the GROUND					
_grd_Dist	0.001	mm	distance between bar and ground	`01C4-ground.py`	/
Meshing parameters					
_csk_ElementSize_1	50	mm	approx. size of the elements of the cask's part 1	`01C-meshing.py`	/
_csk_ElementSize_2	50	mm	approx. size of the elements of the cask's part 2	`01C-meshing.py`	/
_csk_ElementSize_3	50	mm	approx. size of the elements of the cask's part 3	`01C-meshing.py`	/
_csk_ElementSize_4	50	mm	approx. size of the elements of the cask's part 4	`01C-meshing.py`	/
_csk_ElementSize_5	20	mm	approx. size of the elements of the cask's part 5	`01C-meshing.py`	/
_csk_ElementSize_6a	10	mm	approx. size of the elements of the cask's part 6a	`01C-meshing.py`	/
_csk_ElementSize_6b	15	mm	approx. size of the elements of the cask's part 6b	`01C-meshing.py`	/
_csk_ElementSize_6c	15	mm	approx. size of the elements of the cask's part 6c	`01C-meshing.py`	/
_csk_ElementSize_6d	20	mm	approx. size of the elements of the cask's part 6d	`01C-meshing.py`	/
_lid_ElementSize	50	mm	approx. size of the elements of the lid's part	`01C-meshing.py`	/
_pin_ElementSize	10	mm	approx. size of the elements of the bar's part	`01C-meshing.py`	/

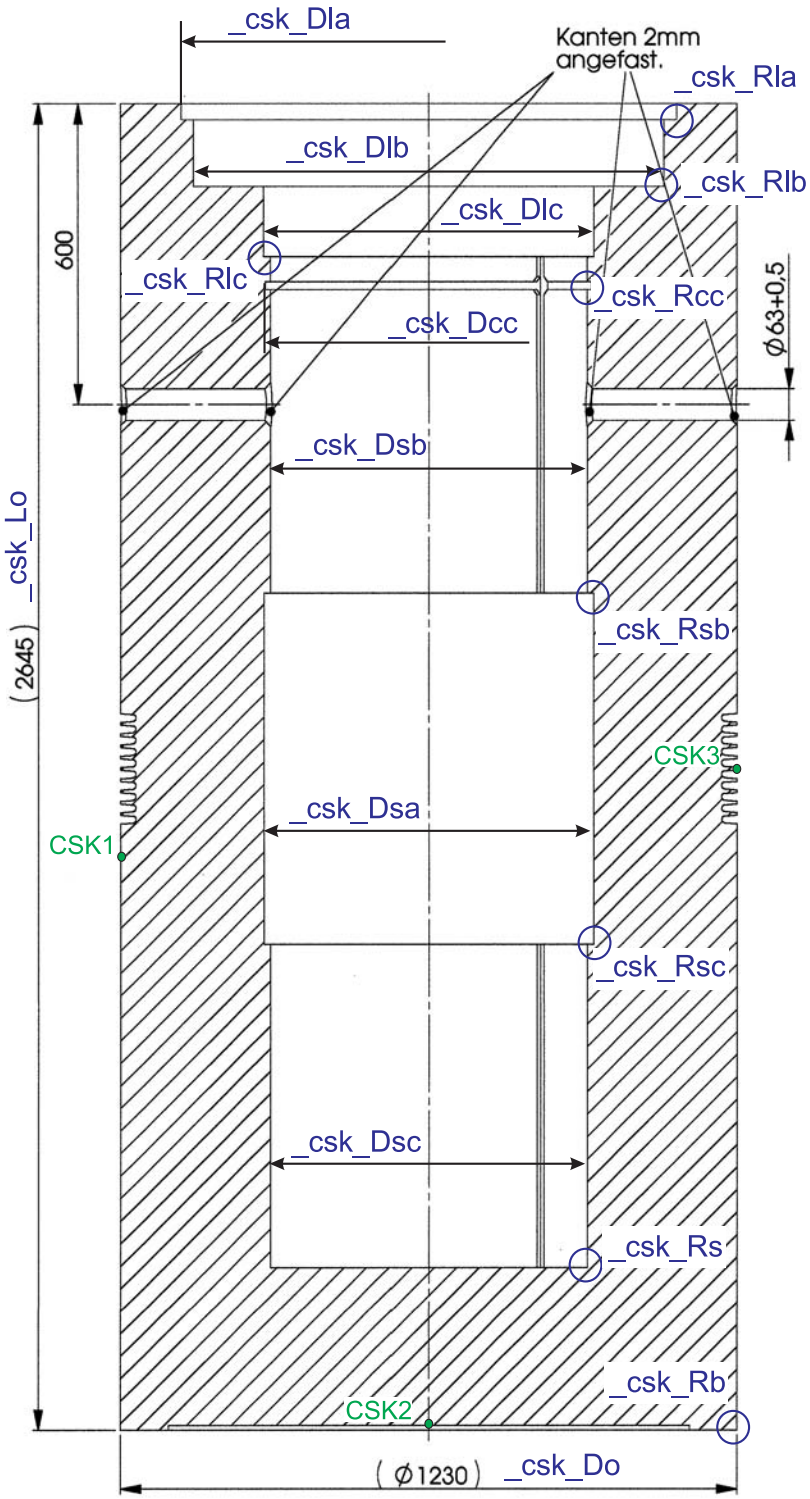

Figure A.1: *The geometry parameters of the cask (1); with measurement points.*

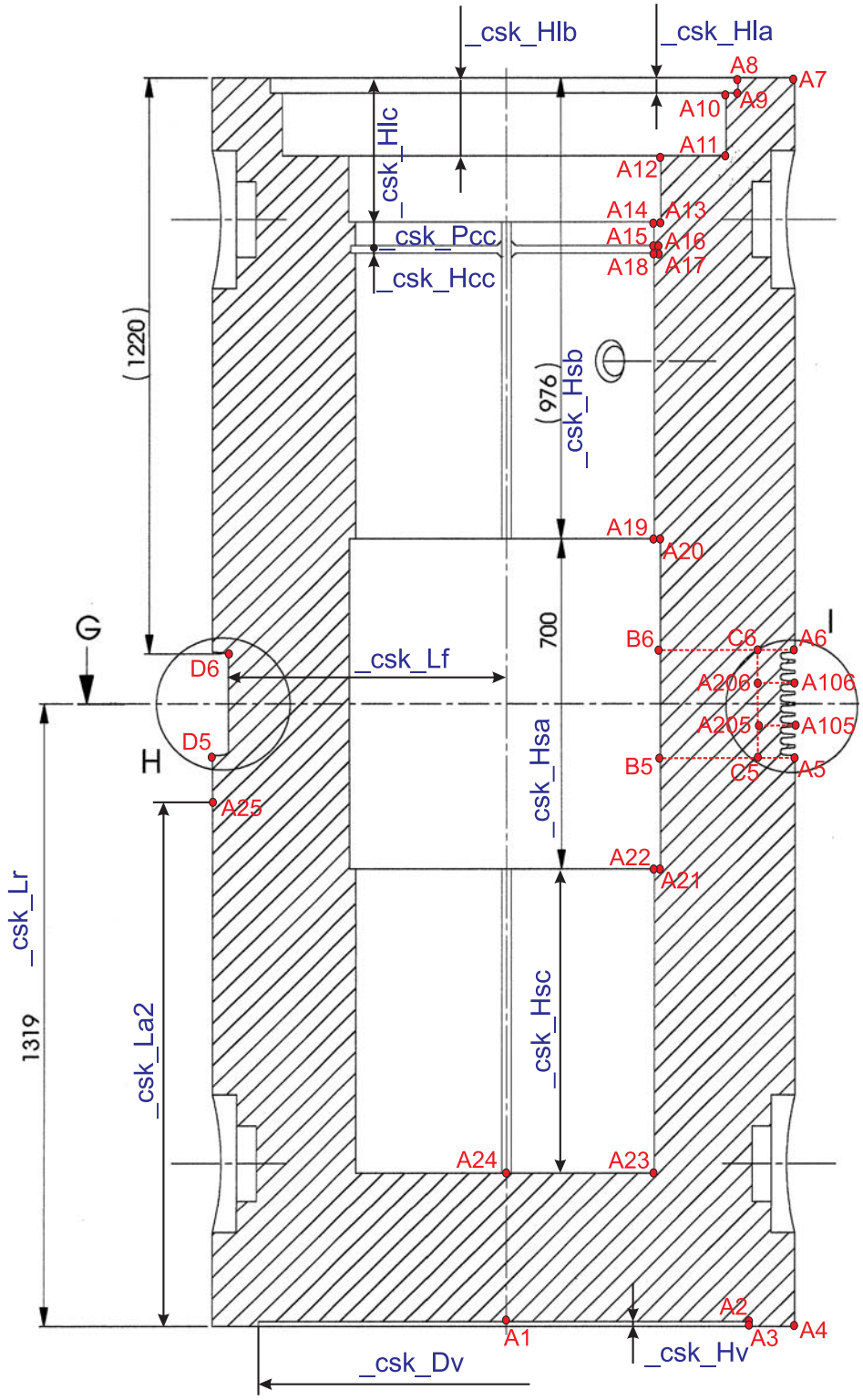

Figure A.2: *The geometry parameters of the cask (2); with geometry definition auxiliary points.*

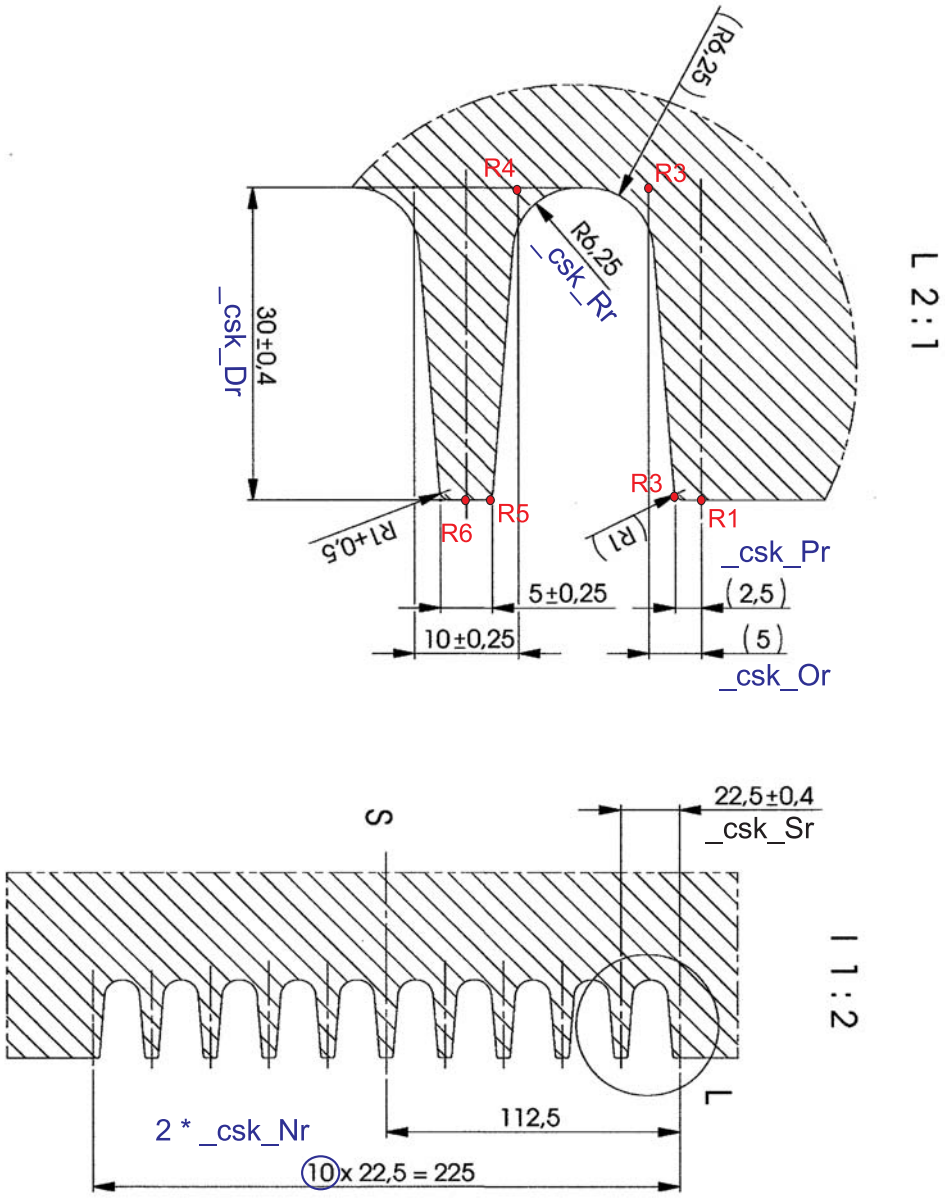

Figure A.3: *The geometry parameters of the cask (3); with geometry definition auxiliary points.*

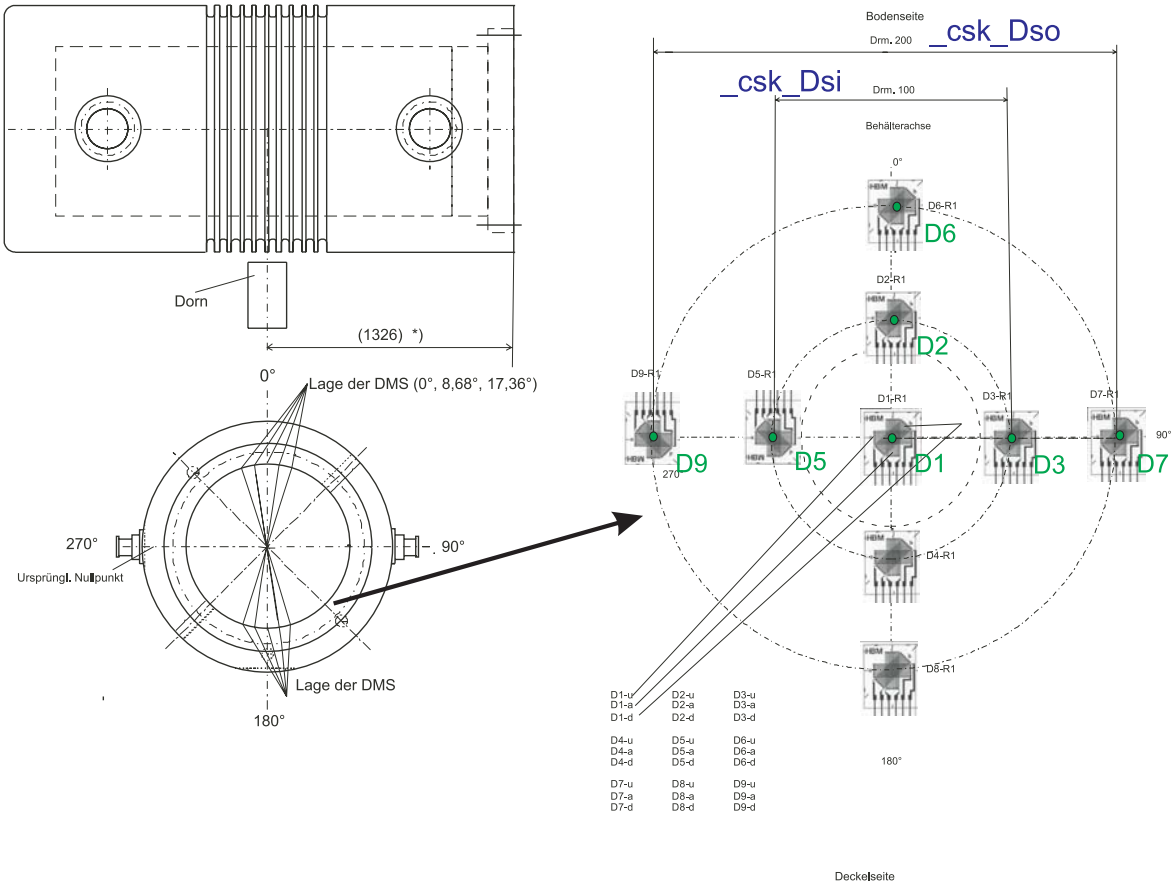

Figure A.4: *The geometry parameters of the cask (4); with strain measurement points.*

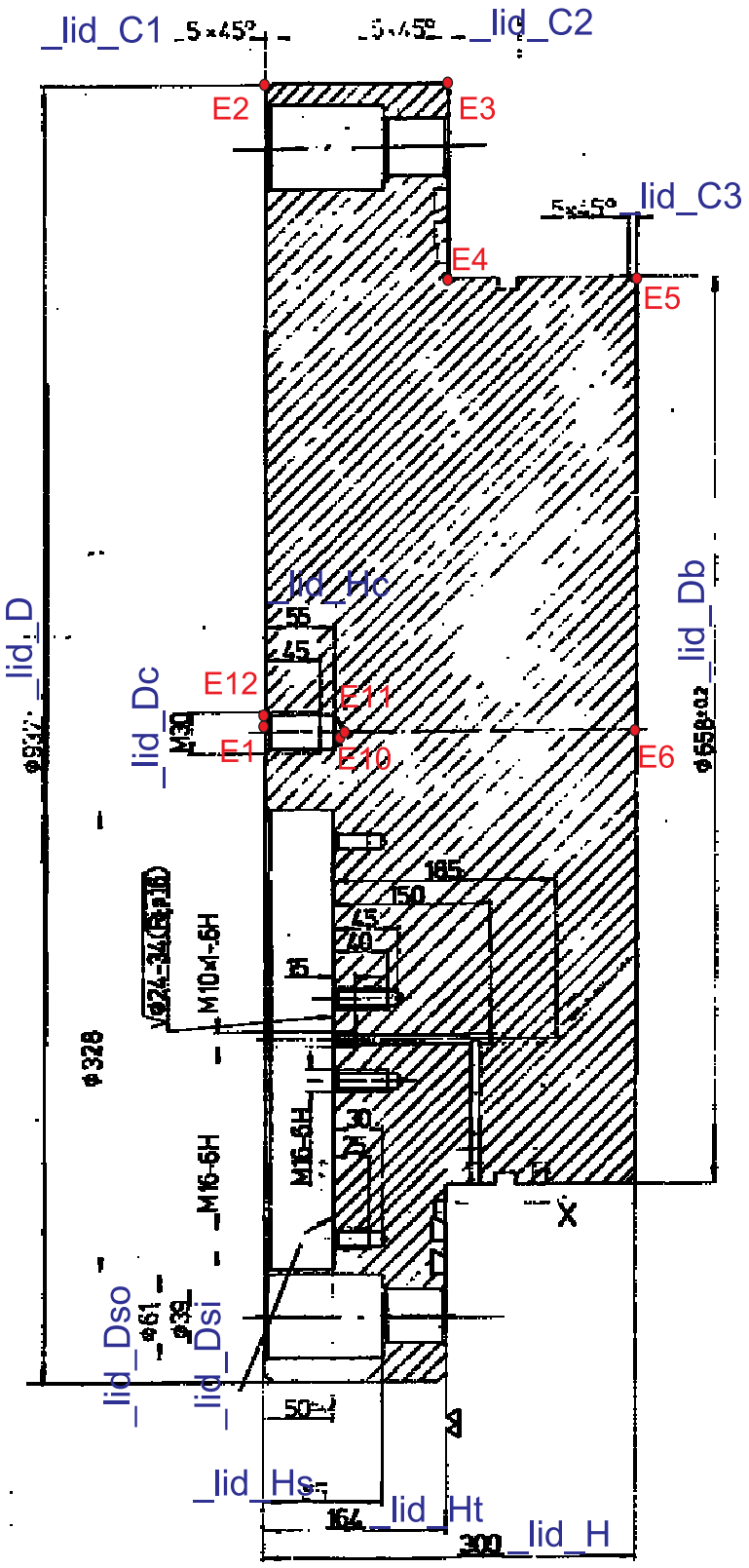

Figure A.5: *The geometry parameters of the lid.*

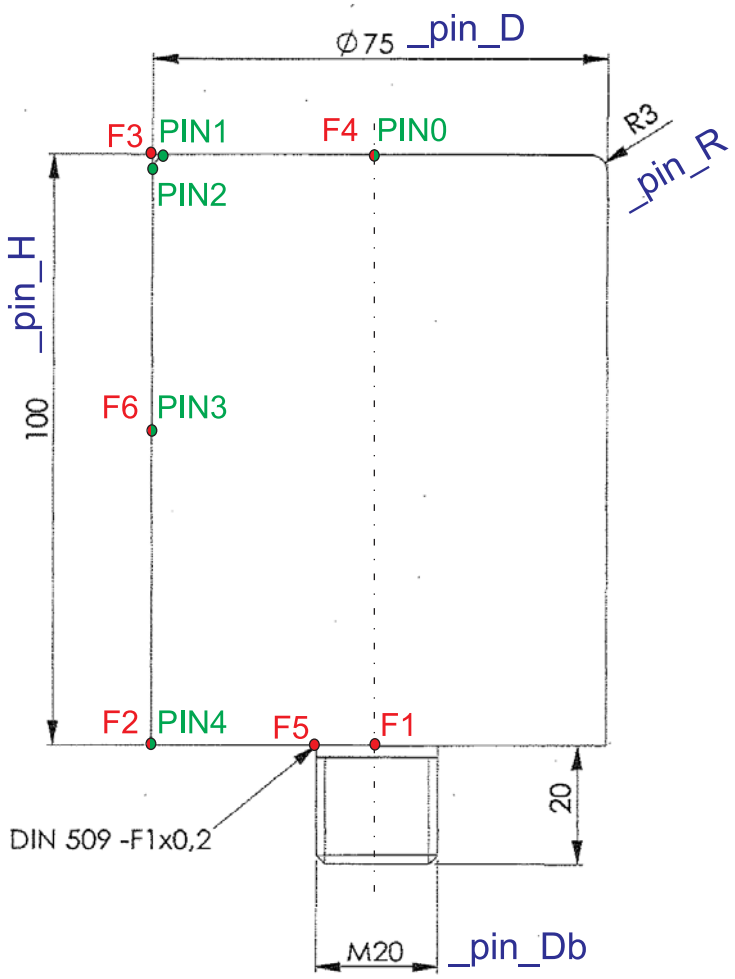

Figure A.6: *The geometry parameters of the bar.*

Appendix B

Material data

Most of the material data were provided by the GNS. The experiment – the drop test – was done at room temperature (RT). Hence, only the material data of the tensile test for the RT is considered. Material data are presented in tables B.1, B.3 and B.2.

Table B.1: *Basic material data.*

		Castor	Bar	Data source
Density	ρ [kg/m^3]	7065	7850	/
Young's modulus	E [GPa]	164	212	[9, 10]
Poisson's ratio	ν [/]	0.3	0.3	/

Table B.2: *Bar tensile test material data at the RT; source: [10].*

Test type		Static $\dot{\epsilon} = 0.004$ [1/s]		Dynamic $\dot{\epsilon} = 1$ [1/s]		Dynamic $\dot{\epsilon} = 10$ [1/s]		Dynamic $\dot{\epsilon} = 100$ [1/s]	
	technical plastic strain ϵ_p [%]	true strain total ϵ^t [%]	true stress σ [MPa]	true strain total ϵ^t [%]	true stress σ [MPa]	true strain total ϵ^t [%]	true stress σ [MPa]	true strain total ϵ^t [%]	true stress σ [MPa]
1	0.0	0.0844	179.2	0.0942	200.0	0.1081	229.5	0.1239	263.2
2	0.1	0.2221	259.9	0.2440	306.6	0.2549	329.9	0.2795	382.5
3	0.2	0.3208	257.9	0.3461	312.0	0.3548	330.8	0.3758	375.5
4	0.5	0.6184	256.6	0.6441	311.9	0.6512	327.1	0.6714	370.7
5	1.0	1.1142	258.3	1.1392	312.4	1.1459	326.9	1.1703	380.1
6	2.0	2.0936	250.5	2.1210	311.0	2.1334	338.6	2.1523	380.4
7	3.0	3.0735	265.0	3.0908	304.1	3.1107	349.0	3.1287	389.6
8	4.0	4.0480	289.3	4.0597	316.3	4.0788	360.2	4.0980	404.4
9	5.0	5.0122	311.8	5.0231	337.5	5.0388	374.3	5.0579	419.2
10	7.5	7.3759	353.2	7.3887	384.6	7.4000	412.5	7.4150	449.3
11	10.0	9.6789	380.3	9.6929	416.1	9.7026	441.3	9.7145	472.0
12	12.5	11.9271	400.1	11.9412	438.2	11.9501	462.3	11.9606	490.5
13	15.0	14.1247	417.3	14.1387	456.6	14.1470	480.1	14.1566	507.3

Table B.3: *Castor material tensile test data at the RT; source: [9].*

Test type		Static $\dot{\epsilon} = 0.004$ [1/s]		Dynamic $\dot{\epsilon} = 0.1$ [1/s]		Dynamic $\dot{\epsilon} = 1$ [1/s]		Dynamic $\dot{\epsilon} = 10$ [1/s]		Dynamic $\dot{\epsilon} = 100$ [1/s]	
	technical plastic strain ϵ_p [%]	true strain total ϵ^t [%]	true stress σ [MPa]	true strain total ϵ^t [%]	true stress σ [MPa]	true strain total ϵ^t [%]	true stress σ [MPa]	true strain total ϵ^t [%]	true stress σ [MPa]	true strain total ϵ^t [%]	true stress σ [MPa]
1	0.0000	0.1086	178.4	0.1205	197.9	0.1275	209.5	0.1392	228.7	0.1591	261.5
2	0.0005	0.1179	192.8	0.1322	216.4	0.1385	226.8	0.1516	248.4	0.1761	288.7
3	0.0010	0.1207	196.6	0.1355	221.1	0.1417	231.2	0.1551	253.4	0.1808	295.6
4	0.0020	0.1245	201.3	0.1401	226.9	0.1461	236.8	0.1600	259.7	0.1870	304.3
5	0.0050	0.1324	209.3	0.1491	236.9	0.1548	246.3	0.1695	270.5	0.1988	318.7
6	0.0100	0.1420	217.0	0.1599	246.4	0.1654	255.5	0.1808	280.8	0.2120	332.3
7	0.0200	0.1577	226.4	0.1766	257.6	0.1822	266.7	0.1982	293.2	0.2315	348.1
8	0.0500	0.1968	241.6	0.2169	274.7	0.2229	284.5	0.2400	312.8	0.2752	371.0
9	0.1000	0.2546	254.7	0.2746	287.8	0.2820	299.9	0.2997	329.2	0.3343	386.5
10	0.2000	0.3623	268.2	0.3801	297.6	0.3906	315.0	0.4081	344.0	0.4379	393.4
11	0.5000	0.6704	285.1	0.6830	306.1	0.6944	324.9	0.7114	353.4	0.7359	394.3
12	1.0000	1.1743	300.7	1.1862	320.7	1.1933	332.7	1.2126	365.1	1.2285	391.9
13	2.0000	2.1708	326.1	2.1825	346.1	2.1864	352.8	2.2070	388.3	2.2190	408.9
14	5.0000	5.0901	382.8	5.1001	401.0	5.1034	407.2	5.1214	439.9	5.1326	460.3
15	6.0000	6.0414	396.5	6.0508	413.9	6.0545	420.9	6.0715	452.5	6.0825	472.9

Appendix C

Script

List of the script files (for structure of files see [1]):

00-run.py The script is run by this file, which loads almost all files as seen in fig. C.1.

01-parameters.py The file defines some parameters and switches and loads the rest of the parameter defining files as seen in fig. C.1.

01A-basic.py The file defines basic numerical and tolerance parameters.

01B-analysis.py The file defines drop test and analysis parameters.

01C-geometry.py The file loads the files defining the cask's (`01C0-cask.py`) and bar's (`01C3-pin.py`) geometry parameters.

01C0-cask.py The file defines cask's geometry parameters.

01C1-lidk.py The file defines lid's geometry parameters.

01C3-pin.py The file defines bar's geometry parameters.

01C4-ground.py The file defines ground's geometry parameters.

01D-mesh.py The file defines parameter for meshing all of the parts.

01E-report.py The file reports the values of all parameters and switches.

02-material.py The file defines material properties.

03-geometry.py The file loads the rest of the geometry defining files as seen in fig. C.1.

03A-cask.py The file defines some auxiliary parameters and measurement points sets. It also loads all files for cask geometry definition as seen in fig. C.1.

03A1-cask(1).py The file defines the cask part 1 geometry and sets.

03A2-cask(2).py The file defines the cask part 2 geometry and sets.

03A3-cask(3).py The file defines the cask part 3 geometry and sets.

03A4-cask(4).py The file defines the cask part 4 geometry and sets.

03A5-cask(5).py The file defines the cask part 5 geometry and sets.

03A6-cask(6).py The file defines the geometry of cask parts 6a, 6b, 6c and 6d and their sets.

03B-lid.py The file defines some auxiliary parameters and geometry of the lid.

03D-pin.py The file defines some auxiliary parameters, geometry and measurement points sets of the bar.

03E-ground.py The file defines some auxiliary parameters and geometry of the ground.

04-mesh.py The file loads meshing definitions as seen in fig. C.1.

04A-cask.py The file meshes all cask parts.

04B-lid.py The file meshes lid part.

04D-pin.py The file meshes bar part.

04E-ground.py The file meshes ground part.

05-assembly.py The file creates assembly and instances of the parts. Instances are arranged or positioned into correct pre-impact position.

06-step.py The analysis step is defined as well as the eventual mass scaling. The field and time histories requests are also defined here.

07-initial-conditions.py The initial conditions are defined.

08-boundary-conditions.py The boundary conditions are defined.

09-loads.py The loads are defined.

10-contact.py The contact definition is configured.

11-connections.py The connections between the cask's instances are defined.

12-job.py The job is defined and submitted.

The file names at the right margin of this document contain whole code of the particular file, which can be downloaded by the double-click on the name.

C.1 Script files' tree structure

The structure of the script files follows closely the ABAQUS modelling philosophy and is presented in fig. C.1. The files' tree description is as follows:

```
00-run.py
    |
    |---  01-parameters.py
    |           |
    |           |---  01A-basic.py
    |           |
    |           |---  01B-analysis.py
    |           |
    |           |---  01C-geometry.py
    |           |           |
    |           |           |---  01C0-cask.py
    |           |           |
    |           |           |---  01C1-lid.py
    |           |           |
    |           |           |---  01C3-pin.py
    |           |           |
    |           |           |---  01C4-ground.py
    |           |
    |           |---  01D-mesh.py
    |           |
    |           |---  01E-report.py
    |
    |---  02-material.py
    |
    |---  03-geometry.py
    |           |
    |           |---  03A-cask.py
    |           |           |
    |           |           |---  03A1-cask(1).py
    |           |           |
    |           |           |---  03A2-cask(2).py
    |           |           |
    |           |           |---  03A3-cask(3).py
    |           |           |
    |           |           |---  03A4-cask(4).py
    |           |           |
    |           |           |---  03A5-cask(5).py
    |           |           |
    |           |           |---  03A6-cask(6).py
    |           |
    |           |---  03B-lid.py
    |           |
    |           |---  03D-pin.py
    |           |
    |           |---  03E-ground.py
    |
    |---  04-mesh.py
    |           |
    |           |---  04A-cask.py
    |           |
    |           |---  04B-lid.py
    |           |
    |           |---  04D-pin.py
    |           |
    |           |---  04E-ground.py
    |
    |---  05-assembly.py
    |
    |---  06-step.py
    |
    |---  07-initial-conditions.py
    |
    |---  08-boundary-conditions.py
    |
    |---  09-loads.py
    |
    |---  10-contact.py
    |
    |---  11-connections.py
    |
    |---  12-job.py
```

Figure C.1: *The script files tree structure.*

Bibliography

[1] N. Jakšić and K.-F. Nilsson, *Numerical simulation of the one meter drop test ona bar for the Castor cask*, European report EUR 22470 EN, ISSN 1018-5593, EC DG-JRC, Institute for Energy, Petten, 2007

[2] IAEA Safety Standards Series, *Advisory Material for the IAEA Regulations for the Safe Transport of Radioactive Material*, Safety Guide, No. TS-G-1.1 (ST-2), International Atomic Energy Agency, Vienna, June (2002)

[3] ABAQUS, *Getting Stated with ABAQUS*, v6.6

[4] ABAQUS, *ABAQUS/CAE User's Manual*, v6.6

[5] ABAQUS, *Analysis User's Manual*, v6.6

[6] E. Paffumi, *Report on dynamic structural integrity analysis of nuclear waste packages*, IE, DG-JRC, EC, Petten, November 2005 (internal document: NSU/EP/200511401)

[7] G.R. Johnson and W.H. Cook, (1983). A constitutive model and data for metals subjected to large strains, high strain rates and high temperatures. *Proc. 7th Int. Symp. Ballistics*, 541–547.

[8] G.R. Johnson and W.H. Cook, (1985). Fracture characteristics of three metals subjected to various strains, strain rates, temepratures and pressures. *Engineering Fracture Mechanics*, **21**(1), 31–48.

[9] GNS, *Technical report on Castor's material priperties*, Nr. E 2005/0085, 22.08.2005

[10] GNS, *Technical report on bar's material priperties*, Nr. E 2006/0080, 30.08.2006

[11] GNS, *Ergebnisbericht der Untersuchung der Wirksamkeit von Rippen beim Fall auf einen Dorn mit dem Behälter CASTOR® AVR*, Nr. GNB B 155/2006, 11.09.2006

[12] GNS, *Untersuchung der Wirksamkeit von Rippen beim Fall auf einen Dorn mit dem Behälter CASTOR® AVR - Merrergebnisse der Fallprüfungen*, Nr. GNB B 156/2006, 18.07.2006

European Commission

EUR 22470 EN /2 - DG JRC - Institute for Energy
NUMERICAL SIMULATION OF THE ONE METER DROP TEST ON A BAR FOR THE CASTOR CASK

Authors: Nikola Jakšić
Karl-Fredrik Nilsson

Luxembourg: Office for Official Publications of the European Communities
2007 - 108 pp. - 21 x 29.7 cm
EUR - Scientific and Technical Research Series; ISSN 1018-5593

Abstract

The report presents the numerical analysis of two one meter drop tests of a single ductile cast iron cask on a steel bar. This analysis is a follow-up to the analysis [1]. The cask comes from the CASTOR family with machined cooling fins in a region where impact occurs. In the first test, the impact is on the cask's cooling fins whereas in the second test the impact is in an area where the fins have been locally machined away. The numerical analysis is based on an explicit dynamic analysis using the commercial finite element code ABAQUS extended with Python scripts to allow a parametric description of the problem. The report describes two sets of analyses. First a comparison to the model used in [1] was carried out together with advanced parameter variation simulations (advanced sensitivity analyses) and then the responses of the basic model are compared with the experimental results provided by GNS. The overall behavior of the model is qualitatively very similar to what was observed during the experiments. The quantitative differences between experimental and numerical responses are generally within 10% and up to 20% with some exceptions. A longer impact duration, (between 3 ms to 5 ms) when the cask is dropped on the fins in comparison to the flat target, is observed in both the analysis and the test. The advanced sensitivity analysis was performed to study the influence of parameters either identified in [1] as influential or not yet tested there. Based on results the final set of parameters values are given and the final analysis is carried out. The overall behavior of the model is qualitatively very similar to what was observed during the experiments.

The mission of the Joint Research Centre is to provide customer-driven scientific and technical support for the conception, development, implementation and monitoring of EU policies. As a service of the European Commission, the JRC functions as a reference centre of science and technology for the Union. Close to the policy-making process, it serves the common interest of the Member States, while being independent of special interests, whether private or national.